NTNU

Norwegian University of
Science and Technology

Battery energy storage system connected to a three-phase 50 Hz-grid

Ida Pria Reite

Master of Energy and Environmental Engineering
Submission date: June 2017
Supervisor: Dimosthenis Peftitsis, IEL
Co-supervisor: Kamran Sharifabadi, Statoil

Norwegian University of Science and Technology
Department of Electric Power Engineering

Battery Energy Storage System connected to a Three-Phase 50-Hz Grid

I dedicate this work to my parents, Kristin and Kennedy, who offered unconditional love and support throughout my graduate studies. I also dedicate this work to my dearest grandmother, Mari Kristine (1926-2013), who unfortunately did not live to see me graduate. I will always appreciate the comfort and encouragement you gave me.

– Thank you so much.

Abstract

Battery energy storage systems (BESS) employing secondary battery technology may offer the greatest potential for large-scale integration of renewable energy sources (RES), and is considered a key element for enabling smart grids for future power systems. The two main components of a BESS are the power conversion system (PCS) and the battery management system (BMS). When selecting a PCS topology, the most important characteristics are the reliability and efficiency of the converter. The converter technologies commonly used for PCS' have been the conventional two- and three-level voltage source converters (VSCs), however the PCS topology chosen for the BESS in this thesis is the modular multilevel converter (MMC).

The MMC offers several advantages over the conventional VSCs, such as modularity and scalability, low total harmonic distortion (THD), excellent efficiency and reliability. The battery technology chosen for the BESS is based on the lithium-ion battery technology. Lithium-ion offers desirable characteristics such as high efficiency, good response time, reasonably high charge and discharge rates, small dimensions and/or low weight and little maintenance requirements. All of the abovementioned converter and battery characteristics imply that the full MMC-BESS scheme will become highly efficient and reliable with a high round trip efficiency, well-suited for large-scale BESS applications.

The system in which the MMC-BESS is investigated, comprises of an offshore wind farm, a two-level VSC-based HVDC transmission system and the AC grid on land. Based on the investigated cases, this thesis can be divided into two main parts: design of the MMC-BESS, and modeling and simulation of the MMC-BESS. The design-part is mainly focusing on a more realistic approach of the MMC-BESS configuration by performing various calculations regarding both battery and converter requirements. The initial MMC-BESS configuration was the conventional, half-bridge MMC with centralized batteries connected to the common DC-link. This approach may offer the simplest solution to implement, however it negatively affects the reliability and efficiency of the full scheme.

Furthermore, to mitigate the drawbacks of the centralized battery-approach, an MMC-BESS configuration based on distributed batteries was proposed. This approach utilizes the MMC's modular structure, as well as improving both the reliability and efficiency. Moreover, by placing bidirectional DC-DC converters, base on the dual active bridge (DAB) topology, in the interface between the converter submodules and the batteries, a galvanic isolation of the batteries could further improve both the safety and reliability of the scheme.

Finally, a proposed approach with the main purpose of reducing space, components and cost, was to replace the two-level VSC stations of the HVDC transmission system with the MMC-BESS based on distributed batteries employing DAB converters. This solution offers the possibility to also improve the performance of the HVDC system. However, more effort should be made in verifying these assumptions.

The modeling and simulation-part analyzed the initially proposed MMC-BESS configuration in the design-part. The MMC was modeled as a simplified MMC, with an AC-side

and DC-side representation and a power balance equation coupling the two sides together. The modeling approach was based on the scientific paper draft presented in [70], as well as the paper presented in [25]. The centralized battery was modeled according to the linear battery model with a small equivalent series resistance (ESR). A state-of-charge (SoC) measurement system was modeled as a part of the BMS, to monitor the charging and discharging processes of the centralized battery. Furthermore, the HVDC transmission system was provided by Prof. Tedeschi and Post.doc. Sanchez Acevedo at the Department of Electric Power Engineering, NTNU. Moreover, the offshore wind farm and the AC grid on land where implemented as ideal AC voltage sources.

The simulation verified the MMC's ability to provide a controlled bidirectional power exchange with the centralized battery. The results showed the MMC operating satisfactorily with an active power flow in the range of 1.0 and -1.0 pu, and well-tuned current and energy controllers. The SoC measurements further verified the charging and discharging processes of the battery, where the battery SoC varied between 100% and 73% SoC. The MMC-BESS ability to provide grid support for variable wind power delivered to the AC grid was also investigated. The results showed the MMC-BESS was able to inject active power to the AC grid, as well as absorb active power from the wind farm. The SoC varied between 100% and 85% throughout the simulation. The last case to be investigated, was a comparison between the MMC-BESS presented in this thesis, where the scheme was connected to the AC-grid, and a BESS solution connected to the HVDC-link of the transmission system. The latter solution is based on the master's thesis of Marta N. Hellesnes, in [38]. Both solutions where able to support the AC grid by smoothing the varying wind power from the offshore wind farm.

Samandrag

Batterilagringssystem (BESS) som nyttar sekundærbatteriteknologi kan syne seg å ha størst potensial for storskalaintegrering av fornybare energikjelder (RES), og er eit nøkkelelement for å gjere smarte nett mogleg for framtidige kraftsystem. Dei to hovudkomponentane i BESS er effektomformingssystemet (PCS) og batteristyringssystemet (BMS). Ved val av PCS-topologi er to av dei viktigaste eigenskapane til PCS-omformaren pålitelegskap og verknadsgrad. Omformarteknologien som oftast vert nytta i PCS har vore dei konvensjonelle to- og trenivåspenningskjeldeomformarane (VSCs), men PCS-teknologien som er valt for BESS-en i denne oppgva er den modulære fleirnivåsomformaren (MMC).

MMC har fleire fordelar i høve til dei vanlege VSC som modularitet og skalerbarheit, låg total harmonisk forvrenging (THD), utmerkt verknadsgrad og pålitelegskap. Batteriteknologien valt for BESS er basert på litium-ionbatteriteknologi. Litium-ion tilbyd ynskjelege eigenskapar som høg verknadsgrad, god responstid, relativt høg lading og utlading, små dimensjonar og/eller låg vekt, og låge vedlikehaldskrav. Alle dei ovannemnde omformar- og battrieigenskapane inneber at heile MMC-BESS-innretninga vil kunne få ein auka verknadsgrad og pålitelegskap, med høg rundtursverknadsgrad, høveleg for større BESS-applikasjonar.

Systemet MMC-BESS vert undersøkt i består av ein havvindpark, eit tonivå-VSC-basert høgspent, likestraumsoverføringssystem og vekselstraumnettet på land. Ut frå dei problemstillingane som vert undersøkte, kan denne oppgåva delast inn i to hovuddelar: utforminga av MMC-BESS, og modellering og simulering av MMC-BESS. Utformingsdelen fokuserar i hovudsak på ein meir realistisk tilnærming til MMC-BESS-konfigurasjonen ved å utføre ulike berekningar med omsyn til både batteri- og omformarkrav. I den opprinnelege MMC-BESS-konfigurasjonen er det sentraliserte batteriet kopla til den felles DC-lenkja til MMC-en. Denne tilnærminga er moglegvis den enkleste løysinga å implementere, men den påverkar systemets pålitelegskap og verknadsgraden negativt.

Vidare vart det føreslått ein MMC-BESS-konfigurasjon basert på distribuerte batteri for å redusere ulempene ved sentral-batteriløysinga. Denne tilnærminga nyttar MMC-en sin modulære struktur, samt forbetrar både pålitelegskap og verknadsgrad. Ved å plassere tovegs DC-DC-omformarar basert på dual active-bruteknologien (DAB teknologien) mellom omformaren sine submodular og batteria, kan fordelen ved galvanisk isolasjon av batteria ytterligare forbetre både sikkerheit og pålitelegskap av systemet.

Til slutt vart ein føreslått tilnærming med hovudføremål å redusere arealstorleik, komponentar og kostnadar, å erstatte VSC-stasjonane på HVDC-overføringssystemet med MMC-BESS med distribuerte batteri og DAB-omformarar. Denne løysinga gir mogelegheit til også å forbetre ytinga til HVDC-systemet. Likevel bør det gjerast meir innsats ved å verifisere desse antakingane.

Modellerings- og simuleringsdelen analyserte den opprinneleg føreslåtte MMC-BESS-konfigurasjonen i utformingsdelen. MMC-en blei modellert som ein forenkla MMC, med ein AC-side- og ein DC-side-representasjon, samt ein effektbalanse som kopla dei to sidene saman. Modelleringsmetoden var basert på dei vitskapelege artiklane presentert

i [70] og [25]. Det sentraliserte batteriet vart modellert ut frå den lineære batterimodellen med ein liten ekvivalent serieresistans (ESR). Eit ladetilstandsmålesystem (SoC-målesystem) vart modellert som ein del av BMS, for å overvake opplading og utlading av det sentraliserte batteriet. HVDC-overføringssystemet vart gitt av Prof. Tedeschi og Post.doc. Sanchez Acevedo ved Institutt for elkraftteknikk, NTNU. Vidare vart havvindparken og straumnettet på land implementert som ideelle vekselstraumskjelder.

Simuleringane stadfesta MMC-en si evne til å utføre ein kontrollert tovegseffektutveksling med det sentraliserte batteriet. Resultate synte velfungerande MMC med straum- og energiregulatorar, der den aktive effektflyten varierte mellom 1.0 og -1.0 pu. SoC-målingane stadfesta opplading og utlading av batteriet, der ladetilstanden varierte mellom 100% og 73% SoC. MMC-BESS vart òg testa for støtte av kraftnettet for varierande vindkraft. Resultata stadfesta at MMC-BESS kunne forsyne nettet med aktiv effekt, og absorbere aktive effekt frå havvindparken. SoC varierte mellom 100% og 85% gjennom heile simuleringa. Det siste tilfellet som vart undersøkt, var ei samanlikning mellom MMC-BESS presentert i denne oppgåva, der tilkoplinga vart gjort ved vekselstraumsnettet, og ei BESS-løysing som var kopla til HVDC-lenkja til overføringssystemet. Sistnemnde løysing er basert på masteroppgåva av Marta N. Hellesnes, i [38]. Begge løysingane stadfesta støtte av straumnettet, der varierande vindkraft vart jamna ut.

Preface

This thesis concludes my master's degree in Energy and environmental engineering with specialization in electrical energy conversion at Norwegian university of science and technology in Trondheim, June 2017. This thesis is a continuation on the specialization project completed in fall of 2016, where the topic and scope of work was proposed by Statoil ASA. The scope of work for the thesis was later redefined to serve as comparative study together with master student, Marta N. Hellesnes, where two different solutions of the given topic were investigated. The topic for my thesis was to investigate a battery energy storage system connected to an AC grid, whereas Marta investigated a battery energy storage system connected to the HVDC-link of an HVDC transmission system.

Throughout this work several people have contributed with academic support and guidance. First of all I wish to thank my supervisor at NTNU, Assoc. Prof. Dimosthenis Peftitsis, as well as Prof. Elisabetta Tedeschi for supervision and structuring my thesis. I would also like to thank Marta N. Hellesnes for the collaboration on the MMC model and for our many meetings and discussions, and Post.doc. Santiago Sanchez Acevedo for helping both me and Marta with the challenges regarding modeling and simulation of the stand-alone MMC. Furthermore, I would like to thank Prof. Arne Nysveen for an interesting discussion and elaboration on transformers. Last but not least, I wish to sincerely thank my co-supervisor at Statoil ASA, Dr. Ing. Kamran Sharifabadi, for his guidance and support, and for always being available for questions.

Ida Pria Reite
Trondheim, June 2017

Contents

List of Figures

List of Tables

Abbreviations

AAC Alternate arm converter

AC Alternate current

APOE Active power oscillation elimination

BESS Battery energy storage system

BJT Bipolar junction transistor

BMS Battery management system

BPSC Balanced positive-sequence current

CAES Compressed air energy storage

CHB Cascaded H-bridge

CSC Current source converter

DC Direct current

DoD Depth-of-discharge

EES Electrochemical energy storage

EMF Electromotive force

ESR Equivalent series resistance

ESS Energy storage system

FC Flying capacitor

FES Flywheel energy storage

GTO Gate turn-off

HV High-voltage

HVAC High voltage alternate current

HVDC High voltage direct current

IGBT Insulated-gate bipolar transistor

IGCT Integrated gate-commutated thyristor

LCC Line-commutated converter

LCO Lithium cobalt oxide

LFP Lithium iron phosphate

LMO Lithium manganese oxide

LNO Lithium nickel oxide

LV Low-voltage

MMC Modular multilevel converter

MT Multi-terminal

NaS Sodium-sulphur

NLM Nearest-level modulation

NPC Neutral point-clamped

PCC Point of common coupling

PCS Power conversion system

PHES Pumped hydro energy storage

PI Proportional-integral

PLL Phase-locked loop

PS-SPWM Phase-shifted pulse-width-modulation

RES Renewable energy source

RMS Root-mean-square

RoCoF Rate-of-change-of-frequency

RPOE Reactive power oscillation elimination

SCES Super-capacitor energy storage

SI Systéme international

SM Submodule

SMES Super-conducting magnetic energy storage

SoC State-of-charge

SRF Synchronous reference frame

SSC System supervisory control

SVM Space-vector modulation

THD Total harmonic distortion

UPS Uninterruptable power supply

VRB Vanadium redox battery

VSC Voltage source converter

ZnBr Zinc-bromine

Part I

Introduction

CHAPTER 1

Background

This chapter covers some background theory on the challenges of renewable energy source integration, particularly offshore wind energy. Furthermore, the power transfer of offshore wind power to the onshore AC grid is done by the means of high-voltage transmission systems. Moreover, HVAC and HVDC transmission systems are reviewed in terms of power capability, losses and the economic break-even distance. Various advantages and drawbacks of each transmission scheme are presented at the end of this chapter.

1.1 Renewable energy source integration

The significant share of renewable energy sources (RES) being integrated onto the grids requires a substantial transformation of the existing networks. Some of these changes include various technologies to ensure proper operation of the grid, where voltage, frequency and power balance must be maintained. Solutions based on energy storage to store energy from RES' increases the supply flexibility and security of the power system [64]. As of today, the balancing power is commonly provided by thermal power plants and rotating reserves.

1.1.1 Challenges of integrating renewable sources

Today's power systems cannot handle the variable and uncertain nature of RES such as wind and solar power often impose. The power system stability relies on a balance between generation and consumption, and the intermittency of wind and solar is of concern when it comes to voltage stability in power systems. Voltage stability regards the ability of the power system to maintain its voltage at all buses in the system under normal operation and after having been subjected to a disturbance [50].

Solar energy can be highly predictable since the movement of the sun is very well documented and understood. Wind energy, however, is less predictable although still sub-

jected to daily and seasonal weather patterns. Studies have shown that wind energy is more available during winter or at nighttime when the wind blows stronger. Yet, the changes in wind power generation is typically more slowly than that of solar power generation which is subjected to fast, second-to-second changes [83].

Nonetheless, whether the RES is wind or solar, they are both posing challenges regarding integration of renewables on to the grid. RES' can be classified into two main categories: dispatchable and non-dispatchable energy resources. Wind and solar energy fall under the latter category, due to their inability to dispatch power when demanded. Dispatchable energy resources involve energy sources such as hydroelectric, biomass and geothermal energy, and are resources that could be called upon at any instant when needed [74].

To better understand why large penetration of RES' pose challenges and complications in the grid, it is important to have an understanding of how the power flows in the system. Active and reactive power flow is controlled by the power angle (i.e. prime mover torque) and voltage relationships, which in turn can be controlled directly by the governor and field current in synchronous generators in the power system. Non-dispatchable energy resources usually lack the capability to provide these controls, which are essential for maintaining the stability and quality control of the power system. They are simply not designed to provide these functions to the grid. However, if the right amount of energy storage and controls were applied, they could be designed to provide these functions [74].

1.1.2 Offshore wind energy

Wind farms provide energy that is a safe, clean and cost competitive alternative for the conventional energy sources such as oil, coal and gas. Yet, the drawbacks with wind farms as they increase in size and capacity are the occupation of large areas, as well as producing audible noise emissions and interference. By placing wind farms offshore rather than taking up space on land, these problems can be mitigated. Additionally, more frequent and more powerful winds are available as opposed to the wind available on land. This implies that the offshore wind power contribution in terms of energy supplied is higher [57].

Offshore wind farms consist of several wind turbines connected together, which in turn are connected to an offshore collection system. From the collection system, the energy is transferred to the AC grid on land via a transmission link. Commonly the collection system can either be a ring (single-sided or double-sided ring) or radial configuration, however in offshore wind farm projects ring configurations have commonly been used. The transmission link from the offshore wind farm to land can either be HVAC, conventional HVDC with line-commutated converters (LCCs), or VSC-based HVDC technology [17], [22], [10].

1.2 Transmission systems: HVDC versus HVAC

There are considerably more HVAC cable installations, both underground and subsea, worldwide than HVDC installations. This is due to the HVAC scheme being less expensive than HVDC, where the converter stations at each end of the transmission system are the main drivers of the cost. However, when cables for HVAC power transmission exceeds a

certain length, HVDC transmission systems become a necessity. Generally, HVDC cable are chosen for power transfer requirements greater than 150-300 MW and if one or more of the following conditions apply [4]:

- Long subsea cable link or interconnection (typically $\geq$ 40 km), with length limits mainly dependent on ampacity[1]
- Intermediate-long subsea cable interconnections (typically 8-40 km) between large HVAC transmission networks, where power transfer control and network stability could lead to serious problems.
- The cost of HVAC power losses becomes higher than the HVDC cable losses and converter losses combined.

One important aspect to consider is that the relationship of cable length to the AC or DC transmission voltage is strongly influenced by the capacitance of the cable. As the length of AC cables and voltage increases, the cable capacitance and thus the charging current increases proportionally. At a certain cable length, the charging current equal the thermal current rating of the cable. This is called the critical length, and at this length no active power can be transmitted. Therefore, for very long cable DC power transmission becomes necessary [4]. Figure 1.1a shows the power capabilities of AC and DC cables [82].

Another term worth noting is the economic break-even distance. At distances greater than the break-even distance, HVDC transmission system will always provide the lowest cost. This distance for selecting HVDC over HVAC transmission systems are for overhead lines approximately 700-800 km, and typically about 40-90 km for subsea cables. Furthermore, some advantages and drawbacks of HVAC and HVDC transmission is listed in Table 1.1 [82].

Figure 1.1b presents the total power losses of HVAC and HVDC transmission system for different cable lengths. As the cable length increases, the resistance of he cable

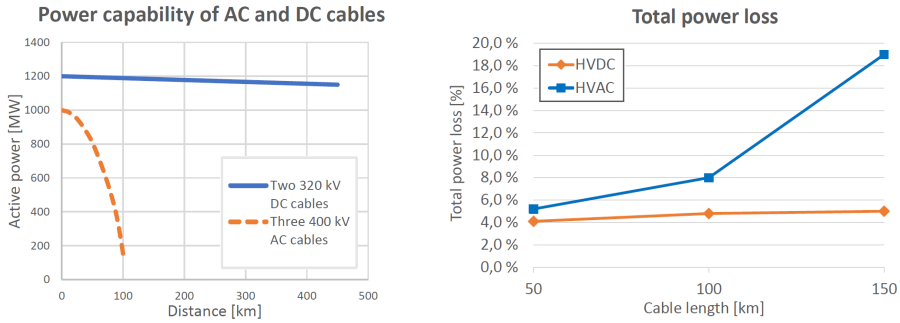

(a) (b)

Figure 1.1: HVAC and HVDC transmission; (a) the power capability for HVAC and HVDC cables, and (b) the total power losses of HVDC and HVAC transmission systems for different cable length.

[1]Defined by National Electrical Safety Codes; ampacity meaning current capacity (current rating or current-carrying capacity) for a device or conductor.

Table 1.1: Advantages and disadvantages of HVDC and HVAC transmission systems.

Transmission system	Advantages	Disadvantages
HVDC	- Greater power per conductor - No skin or proximity effects - Simpler line construction, less environmental impact - No charging current, no need for reactive compensation - Higher power and transmission capacity - Allows for interconnection of asynchronous systems - Power controllability in tie-lines - Limited contribution to short-circuit currents in AC systems - Low short-circuit current on DC lines - Less corona loss and interference - Can be used to increase transfer capability of existing transmission corridors (in parallel links) - Can be used to stabilize AC systems during large disturbances in the power system	- Higher converter losses for smaller transmission distances - Cost of converter stations - Limited overload capability of converters - Conventional HVDC converter stations require reactive power - Harmonic pollution, filtering is required - Lack of HVDC circuit breakers (zero-crossing, arcing and wear)
HVAC	- At lengths less than the economic break-even distance, HVAC is less expensive - Easier transformation of voltage levels - Lower terminal cost	- Lower reliability (bipolar HVDC more reliable than three-phase HVAC) - Thicker conductors (skin effect) - Bigger environmental impact - Requires more conductors

increases accordingly. The higher the resistance, the greater the power losses in the transmission cable. In HVAC transmission systems the power losses mostly occur in the cable, whereas for HVDC transmission systems the converter stations contribute the most to the total power loss [58].

CHAPTER 2

Case Description

This chapter provides information about the system forming the base of the cases to be investigated. The scope of work is presented, as well as an outline of the thesis. A brief overview of the programming tools used in the thesis is given at the end of this chapter.

2.1 System description

An offshore wind farm is connected to the onshore AC grid through an HVDC transmission system, as shown in Figure 2.1. The point of common coupling (PCC) connects a battery energy storage system (BESS) to the AC grid, via a line-frequency transformer with a turns-ratio of n. The BESS' main function is to support the AC grid during variations in power delivered from the offshore wind farm. The power conversion system (PCS) for the BESS is the modular multilevel converter (MMC), due to its excellent characteristics such as modularity, scalability, low total harmonic distortion (THD) and high efficiency. The BESS scheme with its PCS will throughout the thesis be termed MMC-BESS.

System ratings are specified in Figure 2.1, where the MMC-BESS is rated for 10-20% of the nominal active power from the offshore wind farm. The rated active power of the wind farm, HVDC transmission system and the AC grid is 1000 MW. The MMC-BESS rated power was chosen to be 18%, implying the active power flow to and from the PCC is 180 MW. The power factor is set to 0.95, implying that the ratio of active power to the apparent power of the system is high. The power capacity and voltage level increases and the losses decreases with a high power factor, making the power system more efficient.

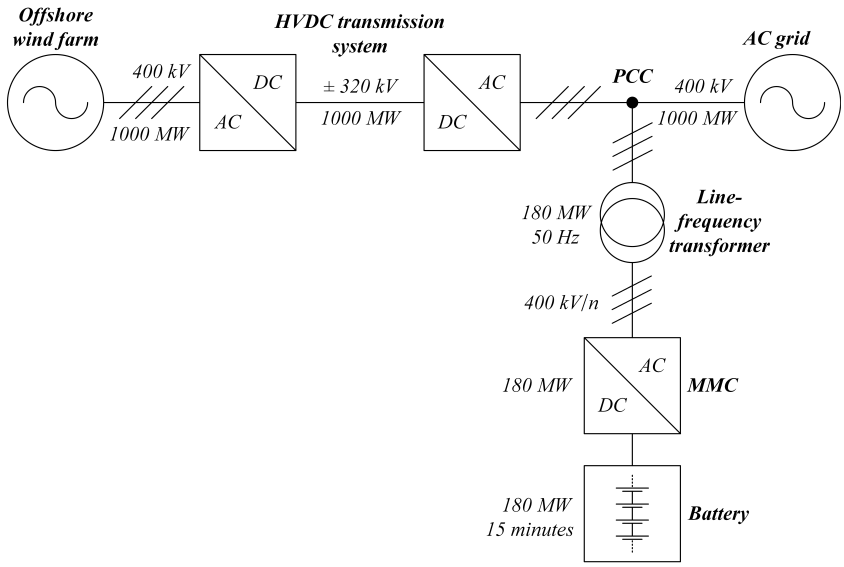

Figure 2.1: Single-line diagram of the power system with given system ratings.

2.1.1 System data

The system parameters are given in Table 2.1.

Table 2.1: System parameters.

Parameter	Value
Nominal active power of the system	1000 MW
Power factor	0.95
Nominal line voltage of the system	400 kV
HVDC-link voltage	$\pm$ 320 kV
Line voltage at PCC	400 kV
Transformer's nominal active power	180 MW
Nominal active power of the MMC	180 MW
Nominal battery discharge power	180 MW
System frequency	50 Hz

2.2 Scope of work

The scope of work in this thesis can be divided into two main objectives:

1. Design of the MMC-BESS: This part investigates the design criteria for an MMC-BESS scheme, based on battery technology and configuration and the power semiconductor devices chosen for the MMC. The structure of the MMC-BESS is also

presented. The aim in this part is to propose a configuration of the scheme with the use of commercially available technologies for a more realistic approach. Losses, cost, area requirements and other factors influencing the design are discussed throughout the design, and form the basis for further improvements of the MMC-BESS scheme.

2. Modeling and simulation of the MMC-BESS: The modeling and simulation offers valuable insight in developing an understanding of the dynamics and interaction of different parts of a MMC-BESS scheme, and of the system as a whole. Although implemented as a simplified model where the macroscopical dynamics are of interest, the MMC-BESS model can still be used to verify the test cases investigated in the thesis. These include the proper operation of the MMC as a PCS responsible for the charge and discharge processes of the batteries in the BESS, and its main function to offer grid support during variable wind power delivered to the AC grid. The MMC-BESS will be modeled as an MMC with a centralized battery connected across its common DC-link.

The main focus is therefore to further analyze and understand the MMC as a promising multilevel converter technology, as well as investigate how it can be implemented as a PCS in grid-scale BESS for simulation purposes. Assumptions and simplifications are provided in each of the parts. Further system information and Matlab scripts for both the design- and the modeling and simulation-part are included in the appendices.

2.3 Thesis outline

The thesis is divided into five parts:

- Part I: Introduction
- Part II: Theory
- Part III: Design of MMC-BESS
- Part IV: Modeling and simulation of MMC-BESS
- Part V: Discussion, conclusion and future work

Part I presents a general introduction of the thesis, as well as a short background on RES and the challenges associated with the increasing share of RES, particularly wind energy, integration into the grid. Transmission systems are shortly reviewed, where HVDC and HVAC transmission are presented. These are not the main focus of this thesis, but offers some basic background knowledge which can be useful to have in mind. Part II provides a short theory-part, mainly focusing on energy storage (ES) technology and voltage source converter (VSC) technology. Conventional and emerging technologies are presented in both topics. The theory is kept intentionally short since it can be found in the specialization project completed in the fall semester of 2016. Part III revolves around the design of the MMC-BESS, where different design criteria form the basis of the selection of

technology and topology. Various design criteria are presented and discussed by comparing different proposed MMC-BESS schemes. Part IV is the modeling and simulation-part of the MMC-BESS, where the modeled system is an MMC with a centralized battery connected to its common DC-link. A line-frequency transformer is placed in the interface of the MMC-BESS and PCC to step the voltage of the MMC to the AC grid voltage level. Three different test cases are simulated and presented, mainly focusing on the MMC-BESS' ability to provide grid support during wind power fluctuations. Part V comprises of discussion, conclusion and future work based on cases investigated in Part III and IV. The discussion takes on other technical aspects of the MMC-BESS' design in Part III, as well as the simulation results and challenges in Part IV.

A short summary is given at the beginning of each chapter to aid the reader with a quick overview of the chapter's content, and to serve as a quick recapitulation for later reviews of the thesis.

2.4 Implementation

2.4.1 Programming tools

The tools used in the thesis are listed below.

1. MATLAB® R2016: Scripts and plots.
2. Simulink: Modeling and simulation.
3. Microsoft Excel 2016: Diagrams and graphs.
4. Microsoft Visio 2013: Figures.
5. LaTeX: Typesetting the thesis.

Part II

Theory

CHAPTER 3

Energy Storage Technology

This chapter presents different energy storage technologies, both commercially and under development, mainly focusing on electrochemical energy storage with rechargeable batteries. The rechargeable batteries can be categorized as conventional batteries and flow batteries, where the main concept and basic structure are shown. Lastly, comparisons between characteristics and properties, as well as cost are presented in tables.

For the grid to accommodate higher percentage of RES and to aid the development towards smart grids, energy storage systems (ESS) are needed. These are essential for compensating the variations and fluctuations in the amount of power generated from the RES,being highly dependent on the time of day, season, and weather conditions [66].

Some ES technologies have already been used for decades and are regarded as mature energy storage technologies, being hydroelectric or pumped hydro (PHES) and flywheels (FES) [68]. Other ES technologies, such as super-capacitors (SCES) and super-conducting magnetic energy storage (SMES) are under development but show great potential as ES [14].

A technical comparison between various ES technologies is presented in Table 3.1. One additional ES category not presented in Table 3.1, but has gained substantial amount of attention over the recent years, is electrochemical energy storage (EES). The next section covers electrochemical energy technology more in depth, focusing on battery technology.

3.1 Electrochemical energy storage

ESS technology covers primary batteries, secondary batteries and chemical ES such as hydrogen, biofuel and biodiesel. Primary batteries are usually not rechargeable and hence not suitable nor applicable for repetitive ES. Secondary batteries however, are rechargeable and have already been used for several decades in a wide variety of applications [68].

Table 3.1: Technical comparison of energy storage technologies [14], [92].

Category	Technology	Maturity	Efficiency	Power	Discharge time	Service life	Application
Mechanical	Pumped hydro energy storage (PHES)	Commercial	70-80%	1000 MW	Days	40-50 yrs	Peak load regulation, frequency regulation, phase shift, reverse, black start
	Flywheel energy storage (FES)	Commercial	>95%	0-20 MW	Seconds-minutes	20 yrs	Frequency regulation, auxiliary service, power quality, UPS
Thermodynamic	Compressed air energy storage (CAES)	Commercial	48-52%	5-300 MW	Days	30-50 yrs	Peak load regulation, reverse, grid-connected renewable energy
Electromagnetic	Super-capacitor energy storage (SMES)	Developing	>90%	0-10 MW	Seconds-minutes	15 yrs	Distributed generation and micro-grids
	Super-conducting magnetic energy storage (SCES)	Developed to 10 MW	>95%	10-100 MJ	Seconds-minutes	30 yrs	Power quality, system stability, low frequency oscillation

Installations of large-scale EES have had an exponential growth in global project installations the past two decades, where storage technologies based on lithium-ion and lead-acid have predominantly been used [68]. The BESS' based on secondary batteries may offer the greatest potential regarding the integration of RES, and the key element for enabling smart grids [83].

3.1.1 Battery technology

The dominating technology for EES is by far based on secondary battery technology. It can further be divided into two categories: conventional battery technology and flow battery technology. Commonly, the conventional batteries are lithium-ion, lead-acid, sodium-sulphur and nickel-cadmium, whereas flow batteries usually consider vanadium redox and zinc-bromine [68].

Conventional batteries versus flow batteries

The basic structure and main components of the conventional and flow battery technology are shown in Figure 3.1 [9]. Conventional batteries consist of positive and negative electrodes, electrolyte and a separator, as depicted in Figure 3.1a. Flow batteries also consist of positive and negative electrodes, however the electrolyte commonly contains two chemical components dissolved in liquids. These liquids are separated by an ion exchange membrane. Additional electrolyte are stored in tanks and pumped through the cells, as shown in Figure 3.1b. The fundamental difference between conventional batteries and flow batteries comes down to *how* the energy is stored. In conventional batteries the energy is stored as the electrode material, while in flow batteries the energy is stored as the electrolyte in the cells [68].

Battery technology comparison and costs

A comparison of the different battery technologies have been made in terms of characteristics and properties, as well as various costs. The comparisons are presented in Table 3.2 and Table 3.3 below. A more detailed discussion and comparison on the battery technologies presented in this thesis can be found in [68].

Table 3.2: Characteristics and properties of various battery technologies [68].

Characteristics and properties	Conventional battery technology				Flow battery technology	
	Lithium-ion	Lead-acid	Sodium-sulphur	Nickel-cadmium	Vanadium redox	Zinc-bromine
Nominal cell voltage [V]	3.7	2.0	2.08	1.3	1.4	1.8
Rated power [MW]	50	20	8	40	3	2
Energy density [Wh/l]	400	80	300	150	35	65
Power density [W/l]	10,000	700	180	600	2	25
Cycle efficiency [%]	97	80	90	83	85	75
Cycle life [cycles]	10,000	1,800	4,500	2,500	12,000	2,000
Daily self-discharge rate [%]	0.10	0.10	0	0.20	0	0

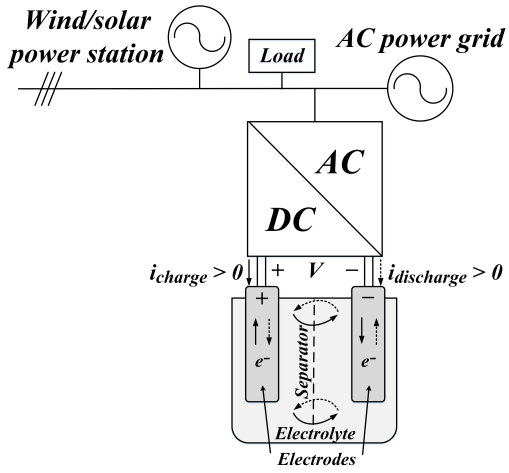

(a) Basic principle of conventional battery technology.

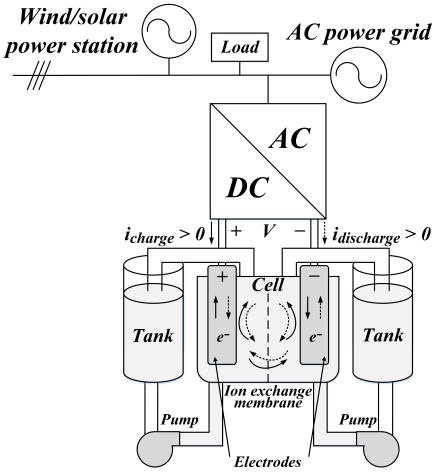

(b) Basic principle of flow battery technology.

Figure 3.1: Battery technologies connected to an AC power grid.

Table 3.3: Various costs of battery technologies [68].

Battery technology cost	Conventional battery technology				Flow battery technology	
	Lithium-ion	Lead-acid	Sodium-sulphur	Nickel-cadmium	Vanadium redox	Zinc-bromine
Capital power cost [US$/kW]	1,200-4,000	300-600	1,000-3,000	500-1,500	600-1,500	700-2,500
Capital energy cost [US$/kWh]	600-2,500	200-400	300-500	800-1,500	150-1,000	150-1,000
Capital cost per cycle [US$/kWh/cycle]	15-100	20-100	8-20	20-100	5-80	5-80

CHAPTER 4

Converter Technology

The aim of this chapter is to give a brief overview of different voltage source converter technologies, ranging from the simple and basic two-level and earlier multilevel voltage source converters to cascaded, modular voltage source converters. The main focus is laid on the modular multilevel converter technology. Basic structure and operation, as well as advantages and disadvantages are presented. More on voltage source converters, with discussions and various comparisons, can be found in the specialization project [68].

Power electronics is another key enabling technology for integration of RES such as wind and solar power, and a crucial part of the development of smart grids and to meet energy efficiency and power quality requirements [78]. Particularly high-power power electronics has gained increasingly more attention over the recent years. Figure 4.1 shows a hierarchical overview of high-power converters [90]. These are power converters capable of handling very high voltages and currents, in the range of kilo-volts and kilo-amps [68].

High-power converters can be classified as direct or as indirect power converters. Direct power converters are capable of power conversion without the need of an intermediate energy storage stage, whereas indirect power converters make use of at least one stage to temporarily store energy. As shown in Figure 4.1, indirect power converters are further divided into two subcategories: current source converters (CSC) and voltage source converters (VSC). CSCs operate with a smooth DC current provided by a reactor [71], and are generally applied for very high power applications (greater than 10 MVA) since it becomes the cheaper choice [23]. CSCs will not be reviewed further, as it lies outside the scope of this thesis.

The converter technology of interest is the VSC technology, which covers the high-power two-level VSC, as well as conventional and cascaded multilevel VSCs.

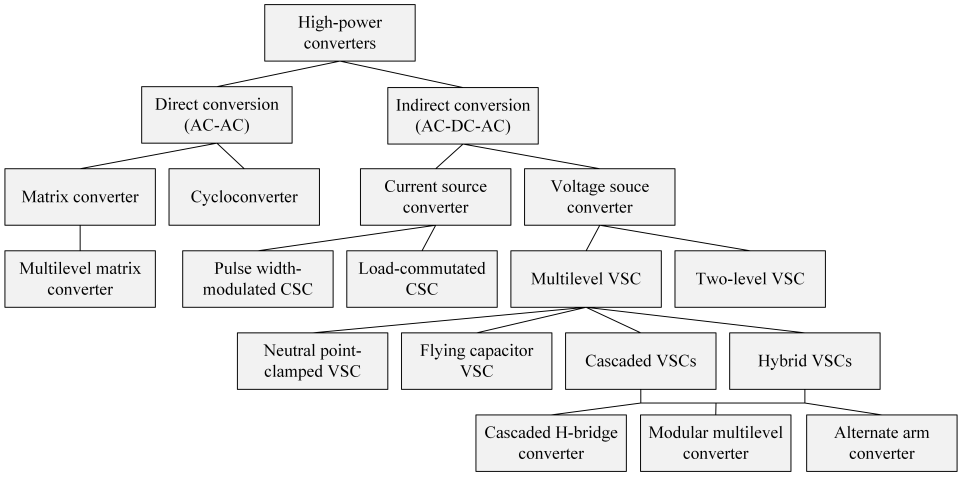

Figure 4.1: Overview of high-power converter technologies.

4.1 Voltage source converters

VSCs, regardless of topology, are converters termed AS self-commutated converters. Self-commutated converters are not dependent on an AC system to operate, which distinguish them from LCCs[1]. VSCs operate with a smooth steady DC voltage provided by a short-term energy storing capacitor [71]. This section will give a short review of five common high-power VSCs, particularly two-level, neutral point-clamped, flying capacitor, cascaded H-bridge and modular multilevel converter.

4.1.1 Two-level voltage source converter

The two-level voltage source converter (2L-VSC) is by far the most commonly used VSC for applications with DC-side voltage up to approximately 1.8 kV. The wide range of applications include industrial drives, automotive drive systems, household appliances and low-voltage grid-tied converters [73]. From the first VSC-based HVDC transmission system[2] installed up until 2012, most VSC-based HVDC transmission systems were based on 2L-VSCs [30], [77].

Figure 4.2 shows the topology of a three-phase 2L-VSC, where each phase contains a number of power semiconductor devices forming a set of switches (S_1 to S_3'). Practically, the switches comprise of an IGBT in anti-parallel with a diode. This arrangement enables a bidirectional current flow of the converter. Each phase-leg contains two converter valves, and a common practice is to directly series-connect switches within the valves to increase the voltage blocking capability of the converter. Furthermore, a DC capacitor provides an approximately constant DC-side voltage for a fraction of the fundamental cycle regardless

[1]Line-commutated converters: Rely on the line voltage of the AC system which forces the current to commutate from one phase to another.

[2]First VSC-HVDC transmission scheme was the Hellsjn-Grngesberg project in central Sweden in 1997.

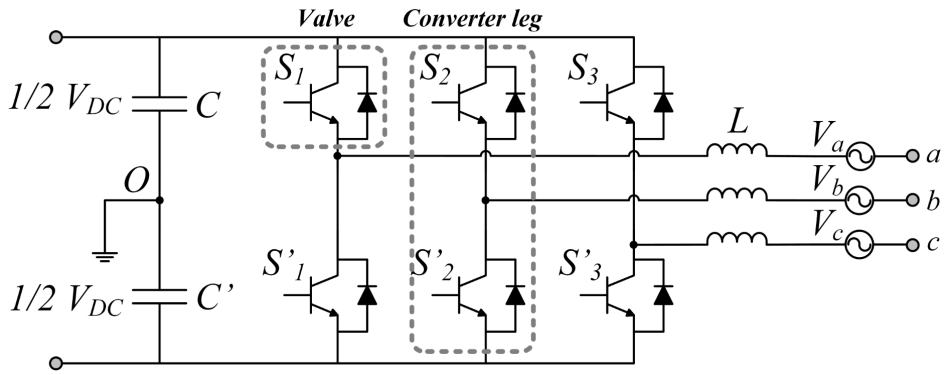

Figure 4.2: Three-phase 2L-VSC.

of the AC currents [73].

The terminals of the DC capacitor ($C + C'$) forms the DC-side terminals of the 2L-VSC. The terminals of the AC-side of the converter are formed by the mid-point of each phase-leg, a, b and c. An inductor L is connected in series with the AC-side terminals to maintain fairly constant AC currents in the short time-frame between commutations within the phase-leg [73].

As the name implies, the 2L-VSC is able to generate only two voltage levels at the output of each phase with respect to the midpoint O: +½V_{DC} and -½V_{DC}. The basic operation and the phase voltage output, v_s, of the 2L-VSC are presented in Figure 4.3, where one phase-leg is shown and the current is assumed to be directed out of the AC-side terminal. Furthermore, Table 4.5 at the end of this chapter summarizes the advantages and disadvantages of the 2L-VSC [68].

4.1.2 Conventional multilevel voltage source converters

The conventional multilevel converters have been on the market long before the MMC was proposed in the early 2000s. Two of the most commonly known multilevel converters are the neutral-point clamped voltage source converter and the flying capacitor voltage source converter, which have been extensively used both in medium- and high-voltage applications. For higher voltage levels, direct series-connection of switches within the valves is necessary, as in the case of the 2L-VSC. Another common feature shared with the 2L-VSC is the use of one or several capacitors managing the DC-side voltage [73].

Neutral point-clamped voltage source converter

The NPC-VSC is a type of diode-clamped topology where the number of voltage levels is mainly limited to three levels. NPC-VSC is the only diode-clamped converter topology to have had significant commercial success in medium-voltage applications. They have also been used for grid integration of wind turbines. Figure 4.4 shows the topology of a three-phase NPC-VSC. It contains twice the number of valves than that of 2L-VSCs, and

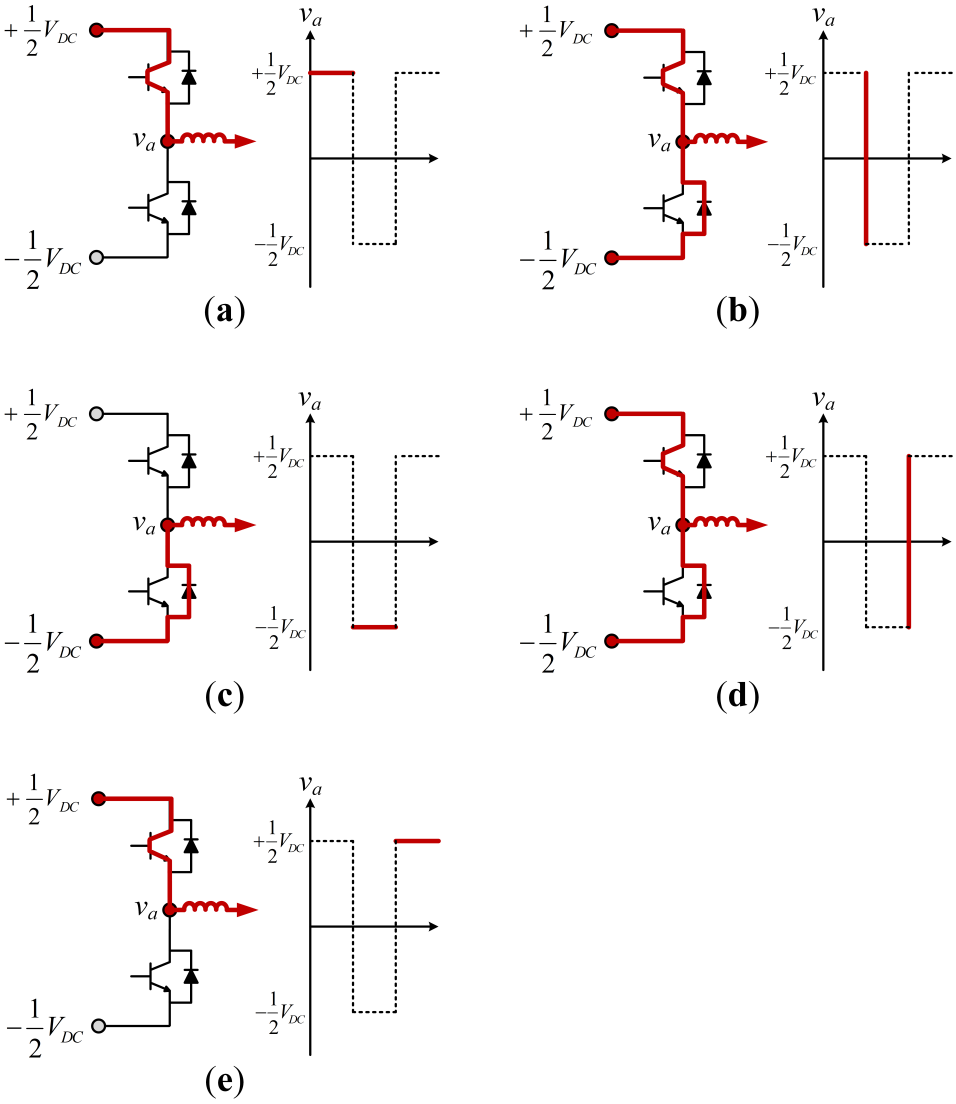

Figure 4.3: The different switching states of one phase-leg of a 2L-VSC.

additionally six clamping diodes connect the AC terminals to the midpoint of the common DC-link. The midpoint may be of neutral potential, hence the name neutral point-clamped VSC [68].

As previously indicated, the NPC-VSC is capable of generating three voltage levels at its phase output: +½V_{DC}, 0 and -½V_{DC}, with respect to midpoint O [68]. The basic switching operation of the NPC-VSC is summarized in Table 4.1 for one phase. Furthermore, advantages and disadvantages of the converter are presented in Table 4.5.

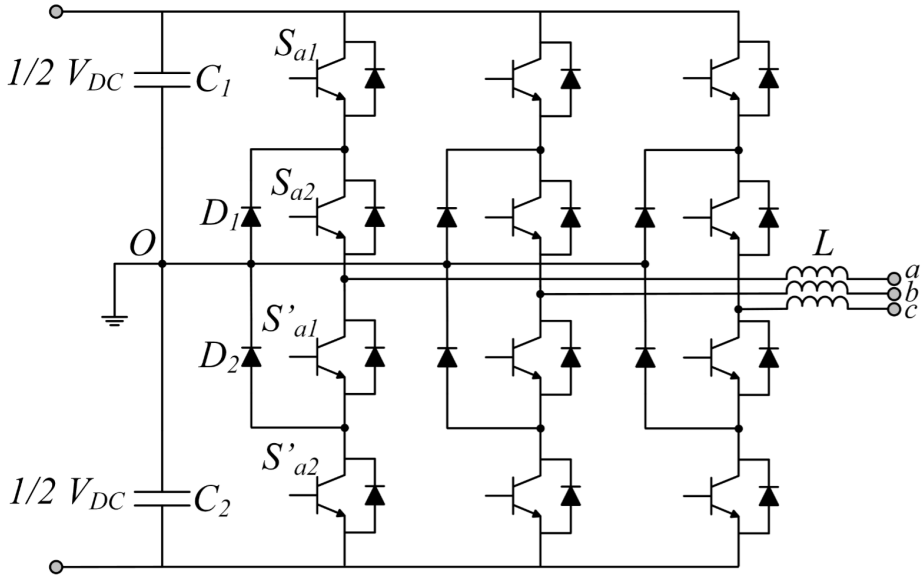

Figure 4.4: Topology of the three-phase three-level NPC-VSC.

Flying capacitor voltage source converter

The flying capacitor voltage source converter (FLC-VSC) is shown in Figure 4.5. The three-level FLC-VSC contains the same number of valves as the three-level NPC-VSC, however instead of clamping diodes the FLC-VSC uses three clamping capacitors, one for each phase. Due to these clamping capacitors, the FLC-VSC is also known as a capacitor-clamped converter.

The voltage levels generated by the three-level FLC-VSC are +½V_{DC}, 0 and -½V_{DC} (with respect to midpoint O), as in the case for the NPC-VSC. However, it has two states which generate zero voltage at the output, and as a result it offers more redundancy than

Table 4.1: Switching states of the three-level NPC-VSC.

Switching states				Phase voltage	Capacitor SoC	
S_{a1}	S_{a2}	S'_{a1}	S'_{a2}		C_1	C_2
ON	ON	OFF	OFF	+½ V_{DC}	unchanged	unchanged
OFF	ON	ON	OFF	0	charging or discharging	charging or discharging
OFF	OFF	ON	ON	-½ V_{DC}	unchanged	unchanged

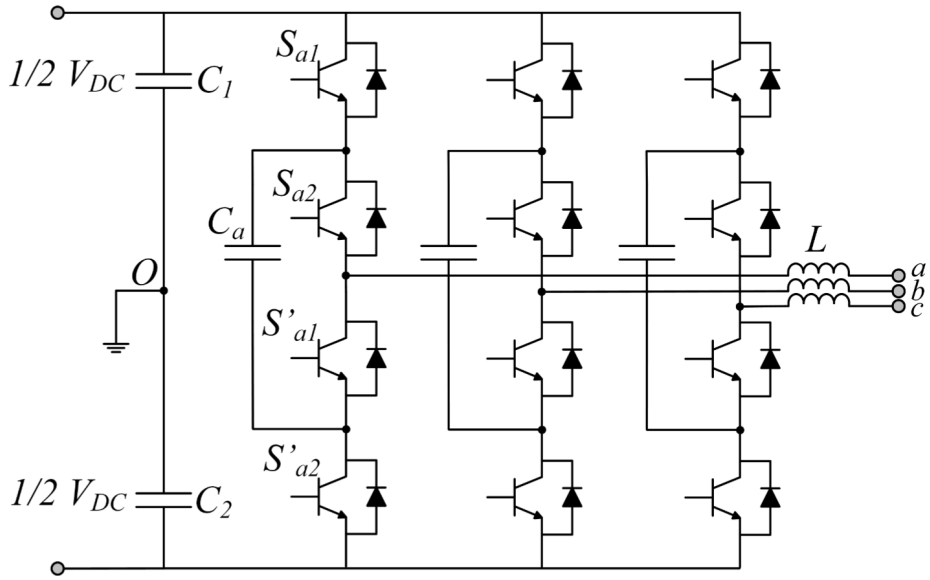

Figure 4.5: Topology of a three-phase, three-level FLC-VSC.

its NPC-VSC counterpart. The direction of the current in the two redundant states are opposite, thus enabling proper voltage balancing of the capacitors. The switching states are summarized in Table 4.2. Additionally, Table 4.5 presents the advantages and disadvantages of the FLC-VSC.

Table 4.2: Switching states of the three-level FLC-VSC.

Switching states				Phase voltage	Capacitor SoC
S_{a1}	S_{a2}	S'_{a1}	S'_{a2}		C_a
ON	ON	OFF	OFF	+½ V_{DC}	unchanged
OFF	ON	ON	OFF	0	charging or discharging
OFF	OFF	ON	ON	-½ V_{DC}	unchanged

4.1.3 Cascaded voltage source converters

The conventional multilevel converters NPC-VSC and FLC-VSC are well suited for applications in the medium-voltage range. The voltage can be increased to a certain degree, however for high-voltage applications the short-comings clearly come into sight. The number of voltage levels cannot be easily extended as previously indicated, especially for the NPC-VSC, resulting in very complex circuitry [73].

As a possible solution to increase the number of voltage levels and to handle higher voltages, a new approach was adapted. Rather than directly series-connect several power semiconductor devices (i.e. switches) within the valves such as for the conventional VSCs, series-connecting converter submodules can be done instead. By adding more submodules higher voltage levels can be achieved, with little or no effort. The submodules contain the main components of any VSC: DC capacitors and unidirectional semiconductor valves [73]. This approach offers modularity and higher degree of redundancy [68]. Two VSC topologies based on the cascaded structure will be reviewed: the cascaded H-bridge converter and the modular multilevel converter.

Cascaded H-bridge converter

The cascaded H-bridge voltage source converter (CHB-VSC) has a topology based on series-connection of H-bridge submodule-strings [68]. By adding the voltage levels generated by each submodule, a multilevel phase voltage is established. This can be illustrated in Figure 4.6, which represents one phase-leg of the CHB-VSC with three H-bridge submodules connected in series. The voltage levels of each submodule can be added or subtracted in order to generate the desirable phase voltage waveform, i.e. a waveform closer to the fundamental sinusoidal waveform. The DC-link voltages of the H-bridge submodules are identical, whereas for the case of different DC-link voltages the converter is commonly termed hybrid multilevel converter [68]. Table 4.5 presents some advantages and drawbacks of the CHB-VSC.

4.2 Modular multilevel converter

The modular multilevel converter (MMC) was initially proposed for HVDC transmission application by Prof. Marquardt in 2003 [52], and first put in commercial use in the Trans Bay Cable project in San Francisco in 2010 [89].

4.2.1 Basic structure and operation

The basic structure of the conventional three-phase MMC with half-bridge submodules is shown in Figure 4.7. As for the case of the CHB-VSC, the MMC is also based on series-connection of submodules, which are essentially controllable VSCs. The three-phase MMC comprises of six converter arms with a certain number of submodules and an inductor, L_a, termed arm inductor. This topology is both modular and scalable, and provides high-quality output voltage waveform with excellent efficiency. Thus, it requires almost no filtering at the output [68].

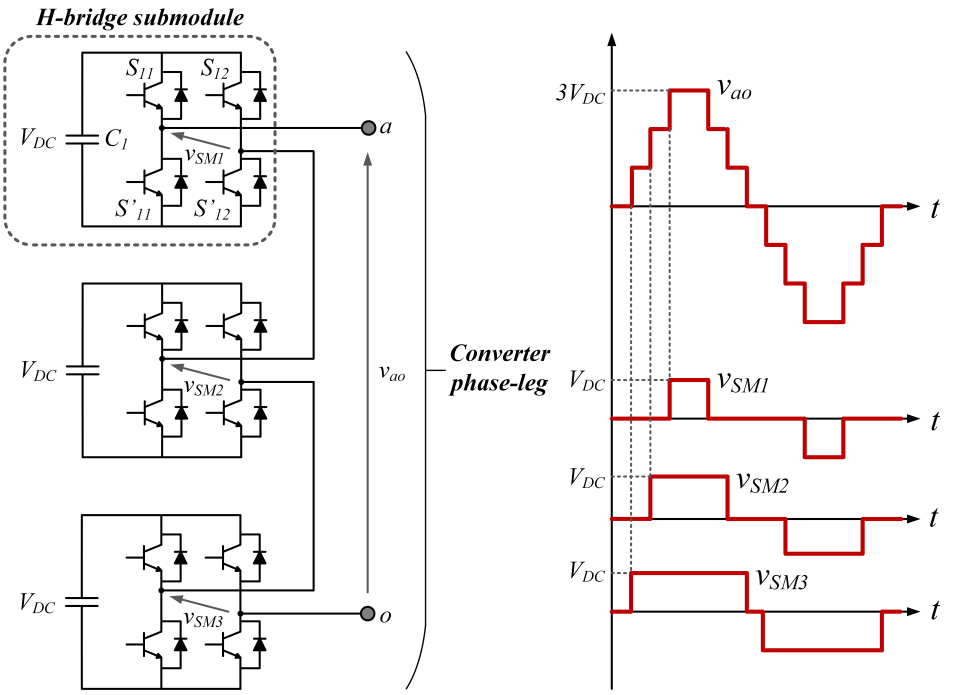

Figure 4.6: One phase-leg of the CHB-VSC with three submodules generating the output phase voltage, v_{ao}.

The proposed structure of the MMC was initially based on half-bridge submodules, however other submodule configurations have been proposed such as the full-bridge submodule. Different submodule configurations for the MMC, with focus on half-bridge and full-bridge submodules, are discussed in detail in Chapter 6.

Furthermore, in contrast to the conventional VSCs, the MMC requires the arm inductors to avoid directly parallel connecting the submodules as they are acting as controllable voltage sources. This is due to the potentially high transient currents that could occur between the phase-legs of the MMC. These arm inductors are usually small [73].

4.2.2 Half-bridge submodule

The half-bridge submodule consists of two controllable power semiconductor devices (commonly IGBTs) and two freewheeling diodes connected in anti-parallel, as shown in Figure 4.8. They form the switches, S_1 and S_2, of the submodule. Additionally, an energy storage device in the form of a capacitor of V_c is connected across the switches to maintain the DC voltage of the submodule [73].

By switching in a complementary manner, the half-bridge is able to generate two discrete voltage levels, $+V_c$ and 0. Apart from maintaining the submodule DC voltage, the purpose of the submodule capacitor is also to limit the voltage across the submodule switches, and allow the MMC to safely generate its multilevel voltage waveform [6]. The

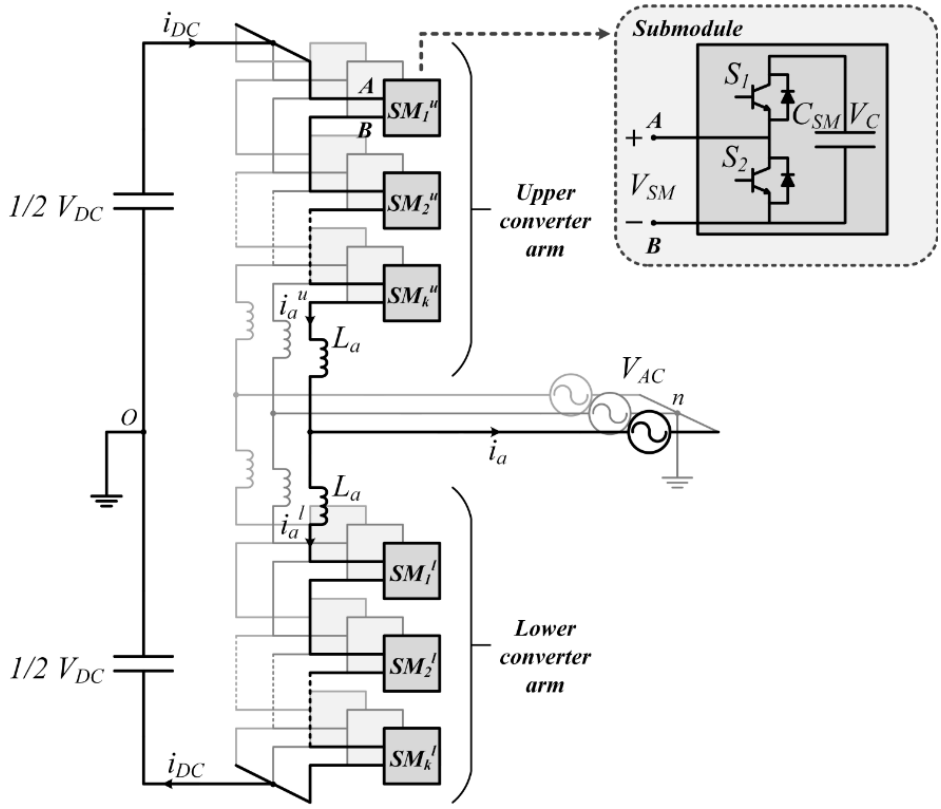

Figure 4.7: Topology of a conventional three-phase MMC with half-bridge submodules.

switching states can be summarized by Table 4.3, as well as visualized in Figure 4.8. A third state termed *blocking* is not used under normal operation, but during start-ups and for certain emergency conditions [73].

Table 4.3: Switching states of the half-bridge submodule.

Switching state	Switch position	Submodule voltage	Capacitor state-of-charge	
			$I_x > 0$	$I_x < 0$
Insertion	S_1 = ON; S_2 = OFF	$V_{SM} = +V_c$	Current is flowing into the submodule, capacitor is in charge mode	Current is flowing into the submodule, capacitor is in discharge mode
Bypass	S_1 = OFF; S_2 = ON	$V_{SM} = 0$	The submodule is bypassed, and the capacitor's state-of-charge is unchanged	The submodule is bypassed, and the capacitor's state-of-charge is unchanged

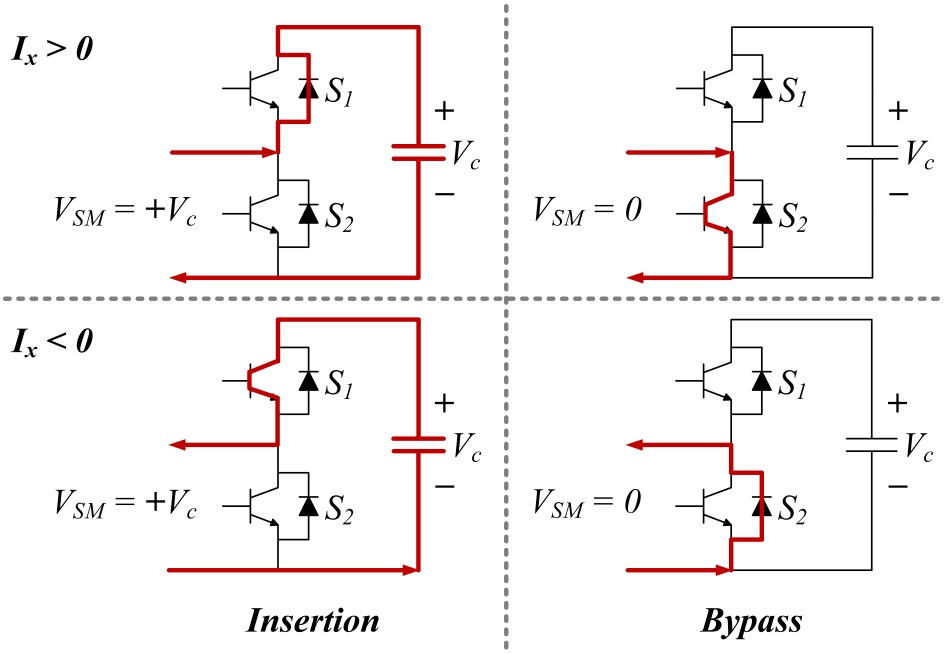

Figure 4.8: Switching states of the half-bridge submodule.

4.2.3 Full-bridge submodule

The full-bridge submodule consists of four switches (S_1 to S_4), where each switch is made up of one controllable power semiconductor device and one freewheeling diode. As for the case of half-bridge submodule, the full-bridge commonly uses IGBTs as controllable power semiconductor devices [44].

The switch pairs S_1 and S_2, and S_3 and S_4, are switched in a complementary manner to form three discrete voltage levels, $-V_c$, 0 and $+V_c$, at submodule terminals. Unlike the half-bridge submodule, the full-bridge is able to handle DC-side faults by generating a counter-voltage to control the current into the DC fault. That is, the counter-voltage generated by the full-bridge opposes the driving AC voltage and provides a negative back EMF to the fault current flow from the DC-side fault [73]. However, the negative voltage level, $-V_c$ is generally not used in normal full-bridge MMC operation [93].

The switching states of the full-bridge submodule are presented in Table 4.4, as well as visualized in Figure 4.9 for positive load current, and in Figure 4.10 for negative load current. As for the half-bridge submodule, a *blocking* state is achieved where all switches are open, i.e. in the OFF-state.

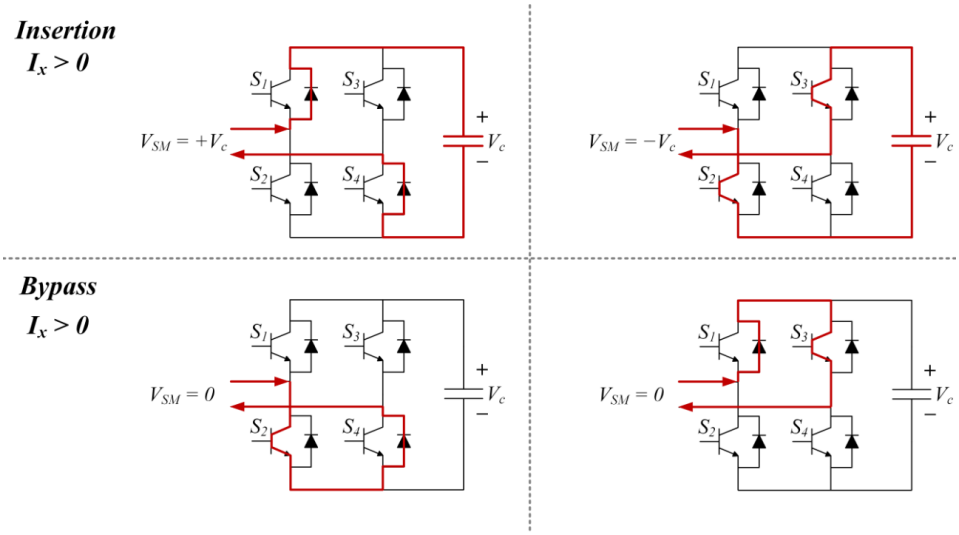

Figure 4.9: Switching states of the full-bridge submodule, for positive load current.

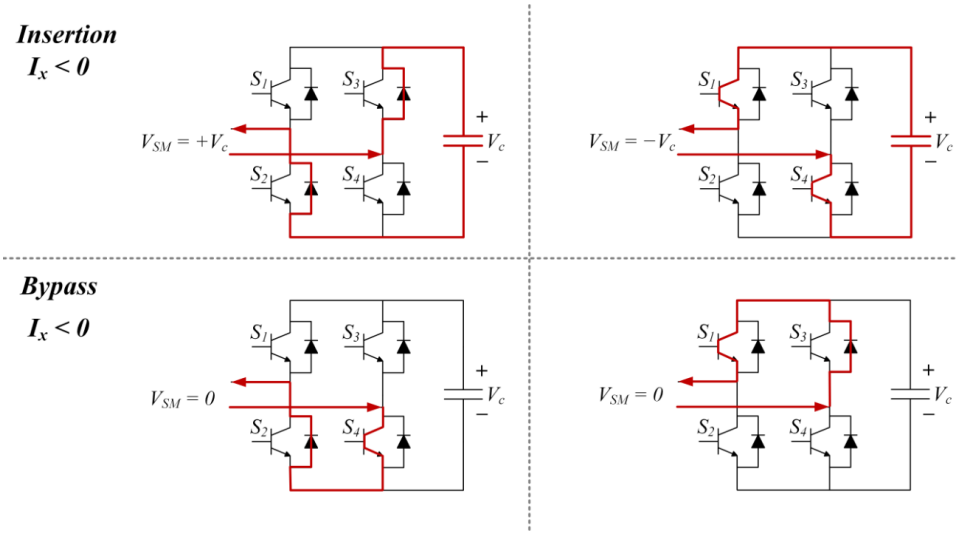

Figure 4.10: Switching states of the full-bridge submodule, for negative load current.

Table 4.4: Switching states of the full-bridge submodule.

Switching state	Switch position	Submodule voltage	Capacitor state-of-charge	
			$I_x > 0$	$I_x < 0$
Insertion	S_1 = ON; S_2 = OFF S_3 = OFF; S_4 = ON	$V_{SM} = +V_c$	Current is flowing into the submodule, capacitor is in charge mode	Current is flowing into the submodule, capacitor is in discharge mode
	S_1 = OFF; S_2 = ON S_3 = ON; S_4 = OFF	$V_{SM} = -V_c$	Current is flowing out of the submodule, capacitor is in discharge mode	Current is flowing out of the submodule, capacitor is in charge mode
Bypass	S_1 = OFF; S_2 = ON S_3 = OFF; S_4 = ON	$V_{SM} = 0$	The submodule is bypassed, and the capacitor's state-of-charge is unchanged	
	S_1 = ON; S_2 = OFF S_3 = ON; S_4 = OFF	$V_{SM} = 0$	The submodule is bypassed, and the capacitor's state-of-charge is unchanged	

4.2.4 Control and modulation techniques

One of the main advantages of the MMC is the ability to generate excellent output voltage waveform that is close to sinusoidal, thus ensuring lower THD and high efficiency. The harmonic content of the MMC is closely related to the number of voltage levels at the output and the modulation technique. Parallel to the advancement of multilevel VSCs, a large number of multilevel modulation techniques have been developed. As the number of voltage levels and consequently the number of controllable power semiconductors increase, the complexity of the modulation algorithm increases [61], [19].

The three most commonly used modulation techniques are the phase-shifted sinusoidal pulse-width modulation, space-vector modulation, and nearest-level modulation, where each modulation technique offers their own sets of advantages and drawbacks [61].

Phase-shifted sinusoidal pulse-width modulation

The phase-shifted sinusoidal pulse-width modulation (PS-SPWM) technique has gained popularity due to its easy digital implementation. The technique involve phase shifts between its multiple triangular carrier signals of the same frequency and magnitude [19]. An MMC with $N + 1$ levels requires N carrier signals to generate the phase-shifted switching pattern which in turn generates the multilevel voltage waveform[3]. In addition to being easily implemented, the PS-SPWM technique also has the advantage of a constant number of submodules in the ON-state at the same time[4]. This reduces the capacitor voltage ripple. Nonetheless, the drawback with PS-SPWM becomes apparent for higher number of levels. As the number of levels increases, the phase shift between the carrier signals becomes very small, implying that the carrier signals must be extremely accurate [61].

[3] N is the number of submodules per converter arm of the MMC.
[4] Regarding $N + 1$ PS-SPWM technique.

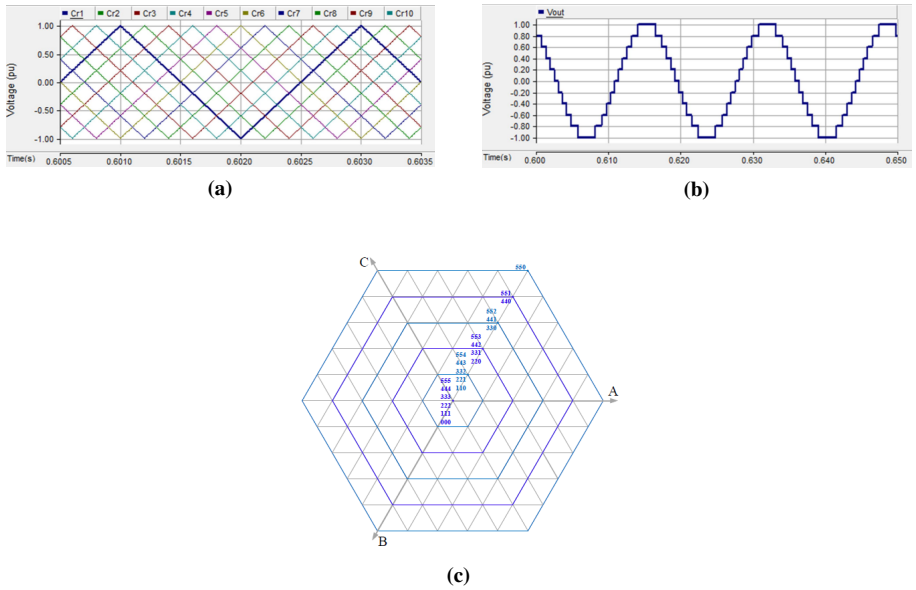

(a) **(b)** **(c)**

Figure 4.11: Modulation techniques; (a) PS-SPWM, (b) NLM and (c) SVM [19],[61].

Space-vector modulation

Another modulation technique which has gained success is the space-vector modulation (SVM) technique. It offers the advantages of being highly flexible to optimize switching waveforms, where the main objective is to improve the DC voltage utilization. The modulation technique computes the switching times based on a three-phase space vector representation of the reference voltage and the switching states of the converter. The reference voltage is linear combination of the switching state vectors to obtain an average output voltage equal to the reference voltage over one switching period. For higher number of levels, the complexity of the SVM algorithm becomes inconvenient as modulation technique [61].

Nearest-level modulation

The nearest-level modulation (NLM) technique has the advantage of offering more flexibility, as well as easy digital implementation, even for higher number of voltage levels. The modulation technique selects the nearest voltage level that the converter can generate to the desired output voltage reference. It avoids using any carrier signals by directly computing the switching states and the duty cycle for each of the converter phases [61].

4.3 Advantages and disadvantages of VSCs

Table 4.5: Advantages and disadvantages of various VSC technologies [68].

Converter technology	Advantages	Disadvantages
Two-level	- Simple - Cheap - Compact - Robust - Small footprint	- High harmonic distortion - High conduction losses - High switching losses - Lower efficiency - Large filters are required
Neutral point-clamped	- Requires half the blocking capability of the two-level VSC - Lower conduction losses - Lower switching losses - Lower harmonic distortion - Smaller filters	- Capacitor voltage balancing difficulties - Limited to three voltage levels - Higher voltage levels lead to higher and uneven distribution of losses, particularly the clamping diodes
Flying capacitor	- Capacitor voltage balancing is less of a problem - Not limited to only three voltage levels - More flexible topology - Large numbers of capacitors allows for short-term ride-through of outages and sags	- Higher cost - Larger capacitors - Double the switching losses than that of NPC-VSC (for constant carrier frequency) - Pre-charging of capacitors are challenging - Complex start-ups
Cascaded H-bridge	- Modular structure, scalable - High degree of redundancy - Well suited for high-voltage applications - Semiconductor devices experience only a small fraction of the total DC-link voltage - Reduced filter requirements - Lower power losses	- Large numbers of separate and isolated DC sources, which must be supplied by a phase-shifting isolation transformer (complex, bulky and lossy, have been used to improve the power factor and current harmonics) - Complex control scheme - Expensive
Modular multilevel converter	- Excellent AC voltage waveform, low harmonics, filtering requirements are greatly reduced - Very low power losses, since low switching frequency is used, hence efficiency is very high - Modular structure, scalable, well-suited for high voltage and high power applications - Increased number of voltage levels does not add considerably to the mechanical and control complexity - Can be made with power semi-conductor with lower voltage ratings	- Still more complex and costly than two-level and conventional multilevel VSCs - Requires a higher number of power semiconductors and submodule capacitors (dependent on submodule configuration) - Need a robust capacitor voltage balancing control scheme to control the voltage stress across each semiconductor device (capacitor voltage must be measured continuously) - Conventional MMC with half-bridge submodules cannot handle DC-side faults

Part III

Design of MMC-BESS

CHAPTER 5

Design of Battery Energy Storage System

This chapter takes on the design of the battery storage system for the MMC-BESS. The specifications and requirements of the batteries are determined, where high-power lithium-ion batteries where chosen as the preferable battery technology. Furthermore, ABB's EssPro™ Grid BESS is chosen as a basis for the configuration of the BESS scheme, where several battery containers (battery modules) are connected in series and parallel. Advantages, drawbacks and challenges are discussed regarding the different proposed configurations. Finally, the technical requirements and the configurations are summarized in a table at the end of this chapter.

5.1 Battery specifications and requirements

The battery power is estimated to be in the range of 10-20% of the total active power from the offshore wind farm. The nominal active power of the offshore wind farm is 1000 MW, with a power factor of 0.95. This implies that the active power of the battery should be in the range of 100-200 MW. A nominal battery power or discharge power, $P_{battery}$, of 180 MW is chosen for this thesis.

Further, the battery discharge time, $t_{discharge}$, is set to 15 minutes (0.25 hours), meaning the battery will go from fully charged (100% SoC) to discharged (at a certain cut-off voltage[1]) in that duration of time. The nominal energy capacity of the battery is the total watt-hours available when the battery is discharged at a certain battery discharge current. In other words, the energy of the battery determines how much power is being delivered and for how long.

[1]The cut-off voltage is the minimum allowable voltage of the battery, defining the battery as "empty" or discharged [80].

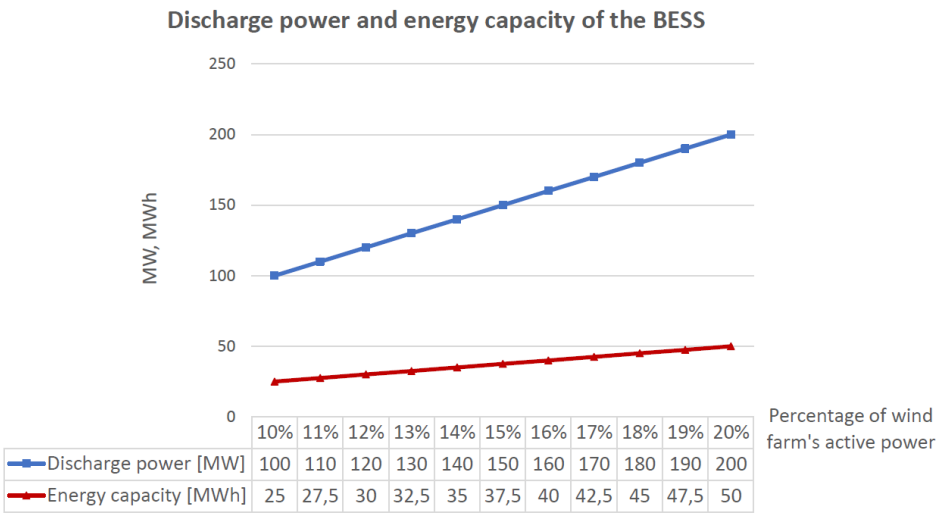

	10%	11%	12%	13%	14%	15%	16%	17%	18%	19%	20%
Discharge power [MW]	100	110	120	130	140	150	160	170	180	190	200
Energy capacity [MWh]	25	27,5	30	32,5	35	37,5	40	42,5	45	47,5	50

Figure 5.1: The BESS discharge power and energy capacity with discharge time of 15 minutes.

The energy capacity is calculated by multiplying the battery discharge power by its discharge time:

$$E_{battery} = P_{battery} \cdot t_{discharge} = 180\,\text{MW} \cdot 0.25\,\text{h} = 45\,\text{MWh} \tag{5.1}$$

The discharge time varies with charging and discharging processes of the battery [80], however for simplicity it is assumed constant. By varying the discharge power between 100-200 MW with constant discharge time, the energy capacity of the battery varies accordingly between 25-50 MWh. The discharge time is shown in Figure 5.1.

5.2 High-power versus high-energy batteries

The application of the BESS may impose several requirements on the battery specifications, such as safety, size, weight and cost constraints. The next step is to determine whether the application is better suited for high-energy or high-power batteries.

Since large-scale BESS generally provide high power capability in relation to energy capacity [84], the batteries should be high-power batteries. The power-to-energy ratio is in this case $180\,\text{MW}/(45\,\text{MWh}) = 4$, implying that the BESS must be designed to maximize its power rating. The lithium-ion battery technology has received much attention over the last several years due to desirable characteristics and properties, as well as offering the possibility to assemble high-power or high-energy battery cells [43], [68].

Figure 5.2 shows a Ragone chart, which are logarithmic curves of available energy versus power demand of various battery technologies at cell level. The lithium-ion battery does not refer to a specific type, but rather to a group of batteries that stretches from high-power area to high-energy area (yellow graph) [68]. Typical high-power lithium-ion

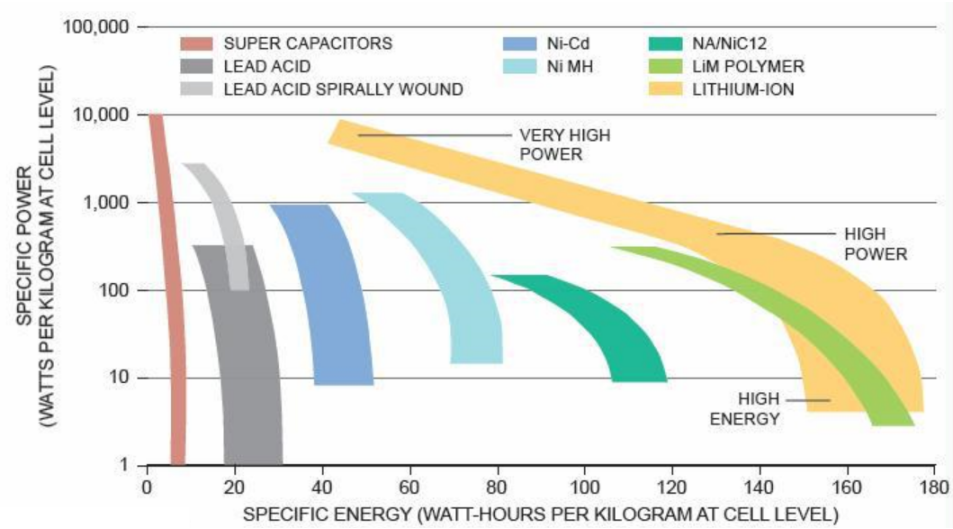

Figure 5.2: Ragone chart showing the relationship between power and energy for specific battery technologies [33].

batteries are lithium iron phosphate (LFP) and lithium manganese oxide (LMO), whereas high-energy lithium-ion batteries are lithium cobalt oxide (LCO) and lithium nickel oxide (LNO) [24].

5.3 Battery technology for energy storage

The batteries used in grid-scale BESS applications have mainly been deep-cycle batteries with nominal energy capacity ranging from 17 to 40 MWh, and efficiencies of about 70 to 80%. Some of the battery technologies used for grid-scale BESS applications are conventional batteries such as lead-acid (both flooded and valve regulated type) and sodium-sulphur (NaS), and flow batteries such as vanadium redox (VRB) and zinc-bromine (ZnBr) [26].

Lead-acid battery is the oldest and most mature battery technology, and has been used for a majority of power system applications [26]. Yet it suffers from short cycle life and slow charging, and regular maintenance is required [68]. Sodium-sulphur was the leading battery technology on the market for high-power energy storage, but as of today it competes with lithium-ion batteries. The drawbacks of sodium-sulphur batteries are the high operating temperature which reduces the efficiency and safety issues regarding fire and explosion hazards, as well as high annual operating costs [68]. Flow batteries have desirable characteristics and properties such long cycle life, fast response and no hazardous emissions, and are not as affected by DoD as conventional batteries. In addition, the scalable nature of the flow battery technology offers almost unlimited energy capacity. Compared to conventional batteries, the flow batteries require pumps, which decrease the overall efficiency by approximately 3%. Active cooling requirements result in additional

cost and losses, as well as increased complexity [45], [68]. Out of the battery technologies discussed in this section and briefly reviewed in Chapter 3, the versatile lithium-ion battery technology has rapidly become one of most popular options for grid-scale BESS applications [59]. Lithium-ion will therefore be further reviewed in this chapter.

5.3.1 BESS with lithium-ion batteries

Lithium-ion batteries offer many great advantages such as high cycle efficiency, high energy and power density, low self-discharge rate, high nominal cell voltage and long cycle life. Other advantages are reasonably fast charge and discharge rate, and the charging process can be intermittent. In addition, the charging process is easier than that of nickel-based batteries. Lithium-ion batteries do not need to saturate as for the case of lead-acid batteries, and little maintenance is required. All of the abovementioned assets pose major advantages for storing renewable energy, especially for solar and wind energy since they cannot always charge the batteries completely [68].

Although having many desirable features, additional safety and control measures are necessary fo the lithium-ion battery. It requires control systems to manage its operation, due to the cycle depth-of-discharge (DoD) affecting the battery lifetime. There are also limitations regarding maximum charge and discharge current. Moreover, lithium-ion batteries require temperature management and protection circuits for safe and efficient operation. Lithium-ion batteries are highly flammable and fragile, and if stressed thermal runaway can occur. Regarding the environmental aspect, the use of organic electrolyte reduces the battery's appeal as an environmentally friendly BESS solution [68].

Being one of the most costly battery technology on the market, trends have shown that lithium-ion batteries have experienced the most rapid decline in cost compared to other emerging battery technologies (advanced lead-acid and flow batteries) over the recent years. This will further strengthen the competitive position against low-cost batteries such as conventional lead-acid and sodium-sulphur [68].

5.3.2 ABB's EssPro^{TM} Grid BESS

The battery module used as the basis for the BESS configuration in this thesis is the ABB's EssPro^{TM} Grid [1]. Other commercially available BESS solutions provided by different manufacturers are listed in Table 5.1.

Applications

According to ABB, the EssPro^{TM} Grid is suitable for a wide range of applications: frequency regulation, spinning reserves, smoothing out rapid voltage and power fluctuations caused by intermittent RES', peak shaving and load leveling, improving power quality, serving as uninterruptable power supply (UPS), and help maintaining the grid voltage by injecting or absorbing reactive power [1].

Table 5.1: Manufacturers of grid-scale BESS solutions.

Manufacturers	BESS technology
Siemens	SIESTORAGE
Alstom	MaxSine^{TM} eStorage
AEG Power Solutions	AEG BESS
Toshiba	Battery Energy Storage System
GE	GE Energy Storage
Bosch	Power Storage Solution
Eos	Eos Aurora® 1000|4000
AES	Advancion® 4 Energy Storage

Technical specifications

The EssPro^{TM} Grid BESS is battery technology independent, meaning the system can be modified for different types of batteries depending on application and requirements. The batteries can either be lithium-ion, sodium-sulphur, nickel-cadmium, lead-acid or flow batteries [1].

The maximum DC voltage of the EssPro^{TM} Grid is 1.2 kV. The output active power ranges from 100 kW up to 30 MW, with a nominal energy capacity from 200 kWh up to 7.2 MWh. Figure 5.3 shows an example of a 1 MW, 15 minutes EssPro^{TM} Grid-configuration [1]. More information regarding the EssPro^{TM} Grid BESS can be found in the technical brochure on ABB's website [1].

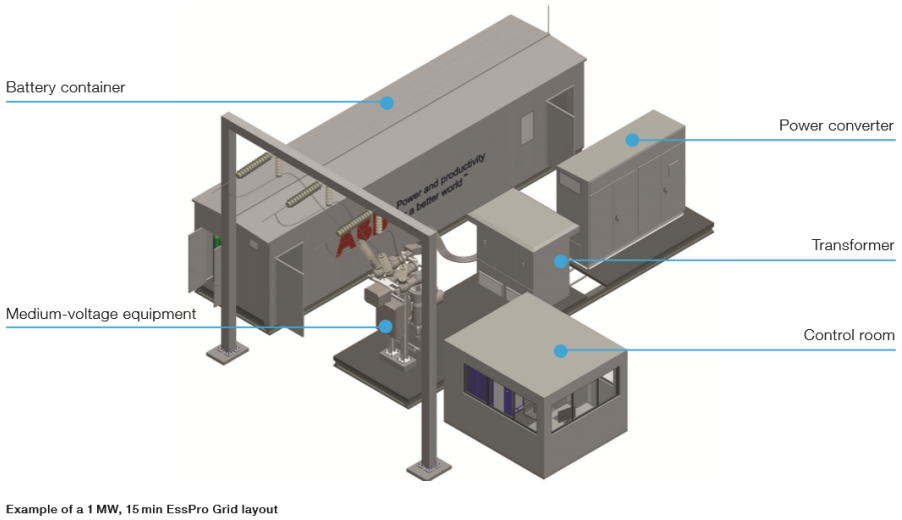

Figure 5.3: One EssPro^{TM} Grid-container. Source: ABB.

Table 5.2: Assumed technical specifications for one EssPro™ Grid-container [1].

Parameter	Symbol	Value	
Discharge power	P_{EssPro}	1 MW	0.5 MW
Max. DC voltage	V_{EssPro}	1.2 kV	1.2 kV
Battery current	I_{EssPro}	833.3 A	416.7 A
Discharge time	t_{EssPro}	0.25 h	0.25 h
Energy capacity	E_{EssPro}	0.25 MWh	0.125 MWh

5.4 Configuration of BESS

5.4.1 Assumptions

Based on the configuration in Figure 5.3, it is assumed that one EssPro™ Grid-container is rated for the maximum DC voltage, 1.2 kV. The output power of one container is further assumed to be either 500 kW or 1 MW, since the the active power range of the container could be changed. Furthermore, the charge and discharge currents of the EssPro™ Grid are not specified, as it is dependent on the battery technology and its internal dynamics. Commonly, these currents differs to some extent from each other due to different internal resistances for the charge and discharge processes, the battery's state-of-charge (SoC), temperature and age [80]. However, in this thesis the currents are assumed equal, and determined by the following equation:

$$I_{EssPro} = I_{charge} = I_{discharge} = I_{battery} = \frac{P_{EssPro}}{V_{EssPro}} \tag{5.2}$$

where P_{EssPro} is the output power (discharge power) and V_{EssPro} is the DC voltage of one EssPro™ Grid-container. This is a fair assumption, since the internal battery dynamics is beyond the scope of the thesis. Additionally, how the battery cells and modules in the container are connected internally is not specified in the technical brochure [1], which also affects the battery current.

The assumptions above for one EssPro™ Grid-container are summarized and presented in Table 5.2 for constant DC voltage of 1.2 kV and a discharge power of 500 kW and 1 MW. Based on Equation (5.2), the battery current will differ, as well as the energy capacity of the container according to Equation (5.1).

5.4.2 Proposed configurations

Generally, battery cells and modules can be connected in various ways in order to get the desired output power. By connecting the modules in series, the voltage of the string increases but the current remains the same through the string. Connecting the battery modules in parallel increases the current but keeps the voltage across the strings constant, cf. Figure 5.4 [68].

Since the required battery power fo 180 MW is very high, it is evident that a large number of EssPro™ Grid-containers are needed. Additionally, these have to be connected in such

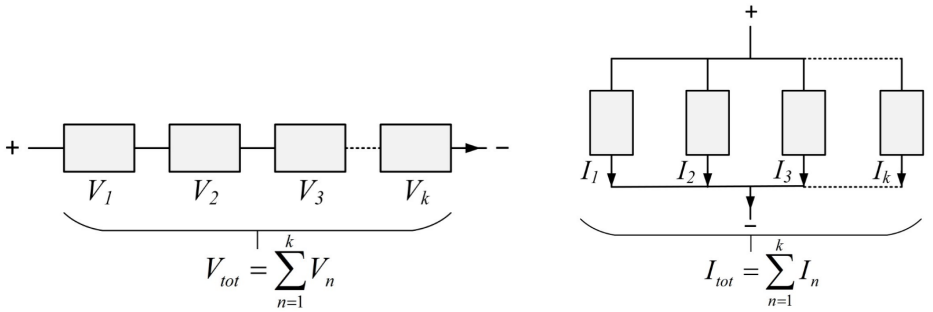

(a) Series-connection of batteries to increase the voltage.

(b) Parallel-connection of batteries to increase the current.

Figure 5.4: Different ways of connecting battery cells together to achieve the desired power.

a way so that the battery power becomes 180 MW by keeping the resulting battery voltage acceptably high, in order to keep the battery current low. A high DC current is undesirable for various reasons: larger cross-section of conductors implying higher cost, heat generation and power losses, and difficulties in breaking DC current as it has no zero-crossings.

By first assuming an EssPro^{TM} Grid-container with ratings of 1.2 kV and 1 MW, 180 containers connected in series would be required for 180 MW output power for the BESS. A configuration solely based on series-connection results in highest possible voltage with lowest possible current at the BESS output. Despite its simple structure, this configuration offers the least desirable solution. If one battery module fails, the rest of the BESS will not be able to deliver or absorb power. Furthermore, if one module is weak or defect, the rest of the BESS becomes as strong as the weakest module. The battery module may not fail immediately but will wear down more quickly - it overcharges longer than the other modules, and drains to the point where reverse polarity might occur. Eventually, the battery module will fail. Maintenance and replacement of battery modules would not be possible for continuous operation of the BESS if the configuration is solely based on one large battery string.

Another aspect is the high resulting battery voltage across the string. With 180 EssPro^{TM} Grid-containers connected in series, where each one has a maximum voltage of 1.2 kV, the resulting voltage at the terminals of the BESS configuration becomes 216 kV, according to the equation below:

$$V_{battery} = N_{series} \cdot V_{EssPro} \tag{5.3}$$

where N_{series} is the number of containers series-connected in the string. Such high voltage levels are commonly used for transmission, and would lead to deterioration of the insulation and possibly arc flash (flash over) in the BESS scheme. This implies the need for high voltage insulation which adds to the cost. These insulators are thicker, in order to lower the breakdown voltage. However, the generated heat in the conductors rises due to the increased insulation thickness which in turn leads to higher thermal resistance [49].

By connecting several shorter battery strings of 1.2 kV, 1 MW EssPro™ Grid-containers in parallel, the resulting battery voltage of the BESS configuration would decrease. Additionally, the operating conditions would improve since the BESS is able to deliver and absorb power if one or more strings get disconnected, however at reduced capacity. This is indeed directly dependent on the number of paralleled strings and the resulting output power of the BESS configuration. The higher the number of parallel-connections of EssPro™ Grid-containers, the more reliable the BESS scheme becomes. However, this comes at a cost of higher resulting battery current, which adds up at the output of the BESS terminals. This is particularly important when selecting suitable power semiconductors for the MMC. Moreover, by paralleling several battery strings the chances of unequal voltages across the strings increases [47].

The number of parallel connections depends on the resulting battery voltage, $V_{battery}$, and the output power, $P_{battery}$ of the BESS configuration, as well as the battery current, I_{EssPro}, of one EssPro™ Grid-container:

$$V_{battery} = \frac{P_{battery}}{N_{parallel} \cdot I_{EssPro}} \tag{5.4}$$

By varying the number of parallel connections, keeping $P_{battery}$ and I_{EssPro} constant and equal to 180 MW and 833.3 A, respectively, different configurations can be realized. Furthermore, by assuming a rating of 1.2 kV and 500 kW for one EssPro™ Grid-container, yields a lower battery current of the BESS configuration. As previously mentioned, the resulting battery current is an important parameter in designing the MMC at a later stage.

Different configurations of the BESS are proposed and presented in Figure 5.5, as well as summarized in Table 5.3. The calculations are done by using Matlab® for quick and easy calculations, and the script can be found in the Appendix A. In Table 5.3, N_{max} is the the number of strings allowed to be disconnected in the BESS configuration, while simultaneously being able to operate satisfactorily. $p_{coverage}$ is the percentage of the wind farm's rated power, which must lie in the specified range of 10-20% as specified in earlier in Chapter 2.

From Table 5.3, it is evident that the proposed configurations 1, 2 and 4 will not be chosen for the BESS. None of the configurations are able to perform within the limits of 10-20% coverage of the wind farm's active power, even if one battery string is disconnected. Configurations 2 and 4 would only be able to cover 9% or 90 MW of the wind farm's active power, while configuration 1 would not be able to operate at all.

Configurations 3, 5 and 6 offer some reliability since one or more battery strings can be disconnected while still ensuring a coverage between 10 and 20%. Configurations 3 and 5 can only disconnect one string and cover 12% and 13.5% (i.e. 120 MW and 135 MW), respectively, while configuration 6 can disconnect up to two strings and still cover 12% or 120 MW. Nonetheless, the two latter proposed configurations require twice the number of EssPro™ Grid-containers, increasing both area and cost of the entire BESS configuration.

Before selecting a specific BESS configuration, the MMC design must be specified. More specific, power semiconductor devices must be chosen according to the arm current of the MMC and the voltage each device must block.

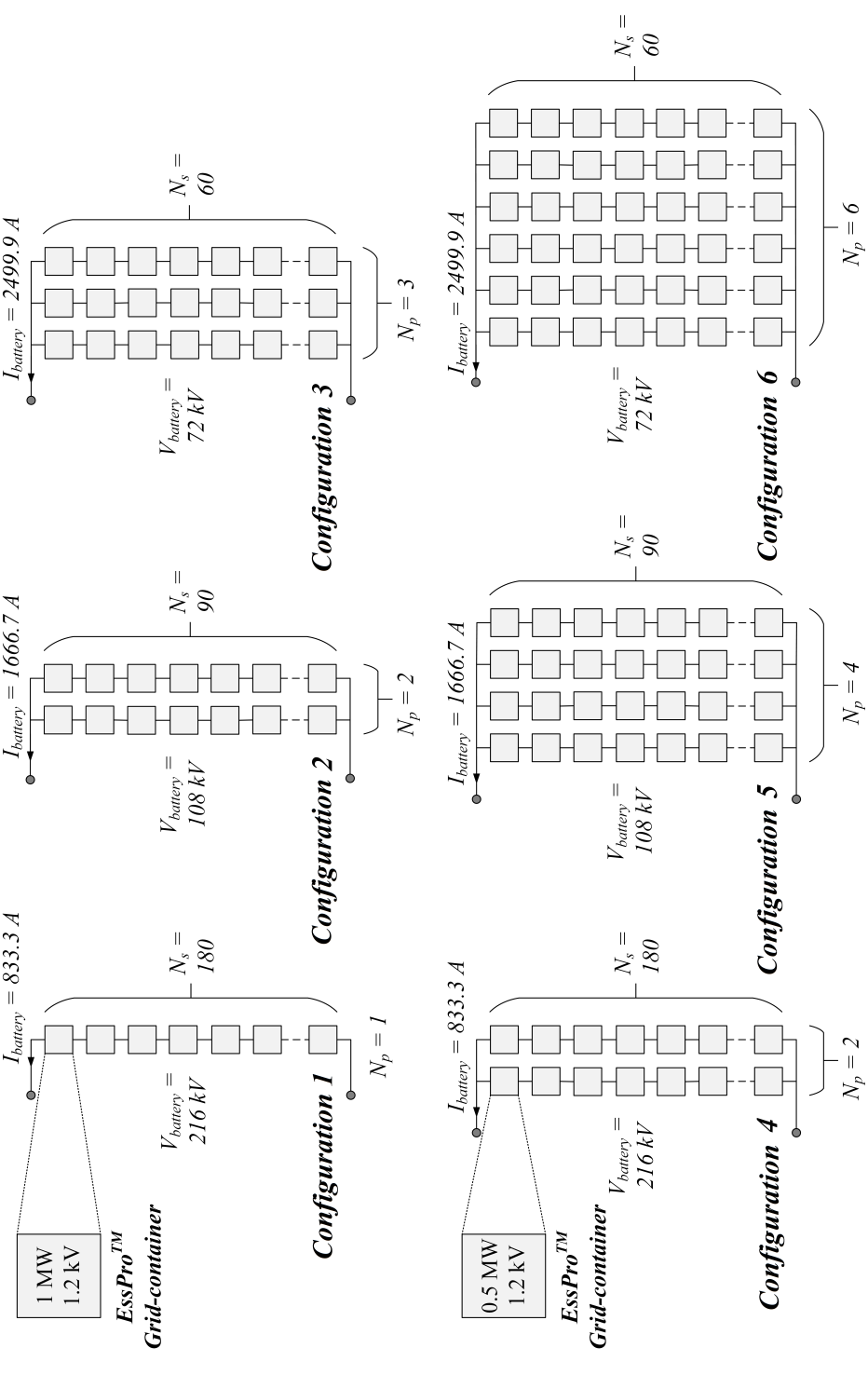

Figure 5.5: Proposed configurations of the 180 MW, 45 MWh BESS.

Table 5.3: Proposed configurations for the 180 MW, 45 MWh BESS.

Rating of one EssPro Grid™-container	Proposed BESS config.	Number of containers in series	Number of paralleled strings	Resulting voltage of confi.	Resulting current of config.	Resulting power of each string	Max. allowable number of disconnected strings	Power coverage of remaining strings when N_{max} are disconnected
		N_s	N_p	$V_{battery}$	$I_{battery}$	P_{string}	N_{max}	$p_{coverage}$
1 MW	1	180	1	216 kV	833.3 A	180 MW	0	18.0%
1.2 kV	2	90	2	108 kV	1666.7 A	90 MW	0	18.0%
833.3 A	3	60	3	72 kV	2499.9 A	60 MW	1	12.0%
0.5 MW	4	180	2	216 kV	833.3 A	90 MW	0	18.0%
1.2 kV	5	90	4	108 kV	1666.7 A	45 MW	1	13.5%
416.7 A	6	60	6	72 kV	2499.9 A	30 MW	2	12.0%

CHAPTER 6

Design of the MMC

This chapter focuses on the design of the MMC, specifically the choice of submodule configurations and controllable power semiconductor devices. Different submodule configurations are briefly reviewed, with the main focus on half-bridge and full-bridge submodules. Additionally, the insulated-gate bipolar transistor and the integrated gate-commutated thyristors are presented and compared for the selection of controllable power semiconductor devices. Finally, three proposed MMC configurations based on the BESS configuration in Chapter 5 are presented.

Conventionally, BESS with conventional two- and three-level VSCs as PCS have been used for megawatt/megawatt-hour applications with batteries connected across the common DC-link of the converter. However, the drawbacks of conventional VSCs include negative impacts on the round trip efficiency[1], cost and reliability of the BESS scheme. Therefore the MMC is considered as the better choice as a PCS due to its modular structure, high round trip efficiency and wide application range as the voltage ratings is easily scalable [76]. The design of the MMC in this thesis is determined by the following steps:

1. Selecting a suitable submodule configuration, based on one or more submodule topologies
2. Calculating the converter arm current to determine the current rating of the power semiconductors
3. Selecting appropriate power semiconductor devices
4. Calculating a number of submodules in one converter arm

[1] Round trip efficiency is the overall efficiency of the BESS scheme, defined as the square of the converter efficiency. E.g. MMC-BESS typically has a round trip efficiency of approximately 98.6%, whereas the 2L-VSC-BESS is approximately 96.0% [76]

5. Calculating the voltage each power semiconductors must be able to withstand, if necessary revise the power semiconductor selection in 3. to meet both current and voltage requirements

It is further assumed that the arm inductors and submodule capacitance are properly sized for the MMC design, and will therefore not be evaluated in this thesis. Moreover, the MMC is assumed to be a three-phase converter, with three phase-legs formed by one upper and one lower converter arm, in total six converter arms.

6.1 Submodule configurations

Several submodule topologies have been proposed in the literature, and can broadly be divided into two categories: unipolar submodules and bipolar submodules. As the name implies, the unipolar submodule is only able to provide unipolar voltage (positive or zero) across its terminals (V_{SM}). The bipolar submodule, however, is able to generate both positive, zero and negative voltages at its terminals. The unipolar submodules are typically simpler, but on the other hand lacks DC fault handling capability. The bipolar submodules have the DC fault ride-through capability, but come with the cost of more complex circuitry and additional power semiconductor devices [48].

Figure 6.1 shows five different unipolar submodule configurations: (1) half-bridge, (2) flying capacitor, (3) diode-clamped, (4) T1, and (5) T2 submodules. Figure 6.2 shows six different bipolar submodule configurations: (1) full-bridge, (2) single-clamped, (3) clamped-double, (4) asymmetrical, (5) mix-connected, and (6) cross-connected submodules. Out of the submodules presented in Figure 6.1 and 6.2, the most common configurations are the half-bridge and the full-bridge submodules [48]. The basic operation of the half-bridge and the full-bridge submodule were reviewed earlier in Chapter 4.

6.1.1 MMC with half-bridge submodules

The half-bridge submodule is by far the dominating submodule configuration used in MMCs. Lower losses, lower cost, as well as having the simplest topology are the main advantages of the half-bridge submodule. The low cost and losses are linked to the low number of power semiconductors.

However, as previously mentioned, the major drawback of the half-bridge as a unipolar submodule is lacking the ability to block DC-side fault within the converter arms. This implies that additional measures of protection are required. As of today, one common method for clearing such faults is to rely on AC circuit breakers connected between the converter and the AC grid [73].

According to CIGRÉ Paper 164 [65] there are two fundamental aspects related to DC-side fault protection:

- Controlling converter current contribution from the AC-side to the DC-side during DC-side faults.
- Isolate the faulty branch (or branches) on the DC-side from the rest of the grid.

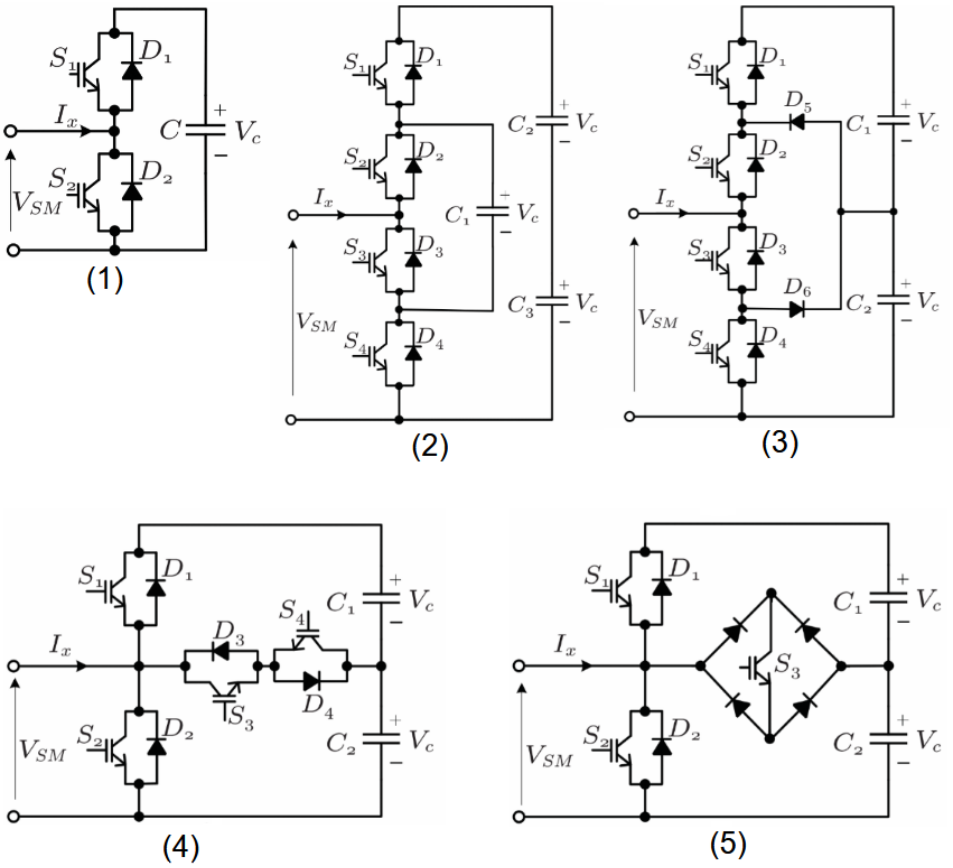

Figure 6.1: Different configurations of unipolar submodules [48].

The former bullet-point is related to the different alternative MMC topologies which have been proposed, in order to establish strategies for handling DC-side faults. One of these alternatives considers replacing the half-bridge submodules in the MMC with full-bridge submodules. The latter bullet-point considers fast DC circuit breakers rather than modifying the converter itself, and will not be reviewed further as it is beyond the scope of this thesis.

6.1.2 MMC with full-bridge submodules

To address the short-comings of the half-bridge submodule regarding DC-fault handling capabilities, several alternative converter topologies have been proposed. One proposed solution has been to replace the half-bridge submodules with full-bridge submodules [65].

Nevertheless, the full-bridge submodule requires twice the number of power semiconductor devices, implying greater power losses and increased cost of a full-bridge MMC, compared to the conventional MMC. A full-bridge submodule is generally not considered

as the optimal choice for fault-blocking in VSCs[2] [65].

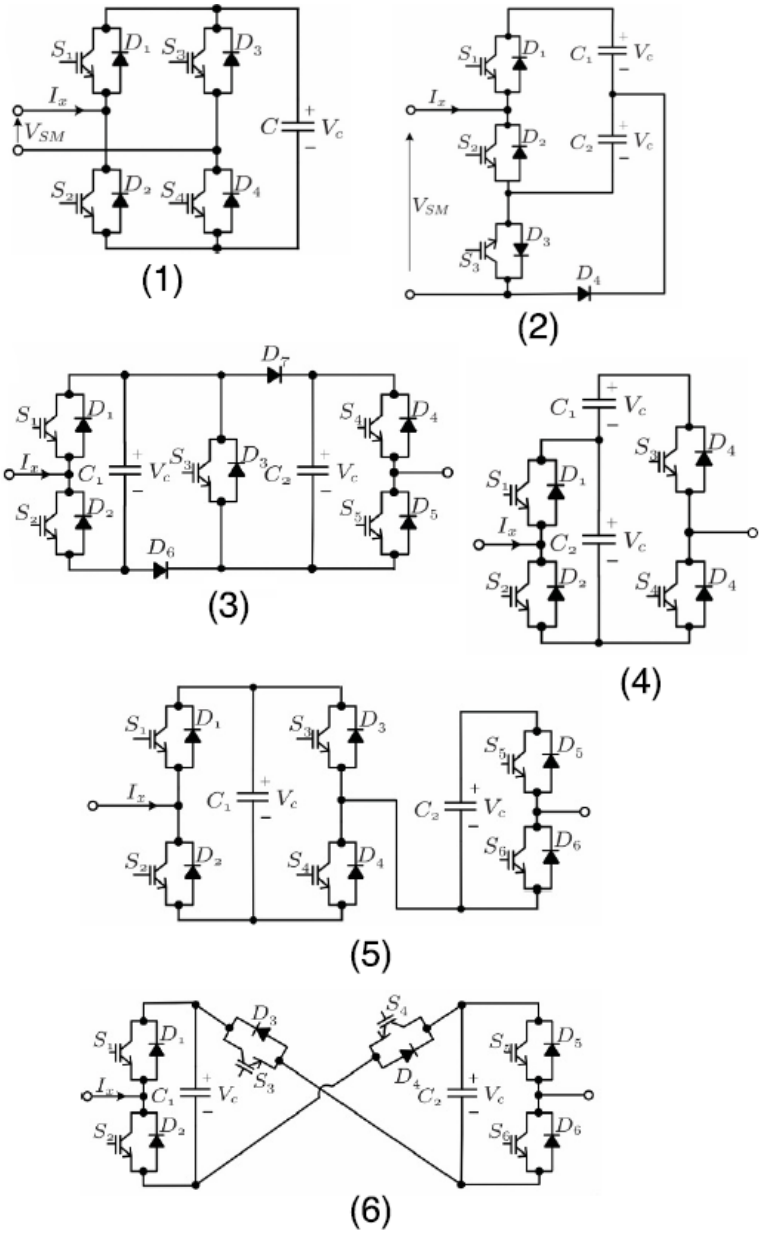

Figure 6.2: Different configurations of bipolar submodules [48].

[2]The shortcomings of the full-bridge MMC was addressed by Alstom, which has developed an improved fault-blocking converter for HVDC applications based on ACC technology, termed HVDC MaxSine^{TM} [39].

6.1.3 Hybrid MMC with half-bridge and full-bridge submodules

Another option is to combine a mix of half-bridge submodules and full-bridge submodules in a converter arm of the MMC. This configuration is commonly known as hybrid MMC. By defining the total number of submodules in each converter arm as N, and the number of full-bridge submodules as N_{FB}, then $N - N_{FB}$ is the number of half-bridge submodules.

For the MMC to successfully block DC faults, the number of full-bridge and half-bridge submodules must comply with the following equation [93]:

$$N_{FB} = \frac{\sqrt{3}}{4} N \approx 0.43N \tag{6.1}$$

Thus, a hybrid MMC configuration where the fraction of full-bridge and half-bridge submodules are equal, i.e:

$$\frac{N_{FB}}{N} = 0.5 \qquad \text{and} \qquad \frac{N - N_{FB}}{N} = 0.5 \tag{6.2}$$

offers the same possibilities of controlling the currents in the AC- and DC-side of the MMC, both during stiff DC-side faults and under normal operating conditions. The half-bridge submodules need to be blocked as in the case of the conventional MMC [93], [65].

With N_{FB} equal to 0.5, the structure of the submodules can be simplified to form a new, hybrid submodule, based on series-connection of half-bridge and full-bridge submodules. Assuming normal operation where voltage level $-V_c$ is not used, S_3 is permanently in the OFF-state and can therefore be removed. This is shown in Figure 6.3, where the number of switches are reduced by one, and a diode D is added to provide a path for the fault current during DC-faults. Based on the aforementioned assumption, the switching states of the hybrid submodule in Figure 6.3a are presented in Table 6.1 [93].

The cost and power losses of the hybrid submodule configuration will be lower than that of the full-bridge MMC, since half of the submodules are full-bridges. However, compared to the conventional half-bridge MMC the cost and power losses become higher. Figure 6.4 shows the normalized losses of the conventional MMC, the full-bridge MMC and the hybrid MMC presented in this chapter. Valve losses, as well as cost are shown in Table 6.2. The cost and losses shown in Figure 6.4 and Table 6.2 are normalized with

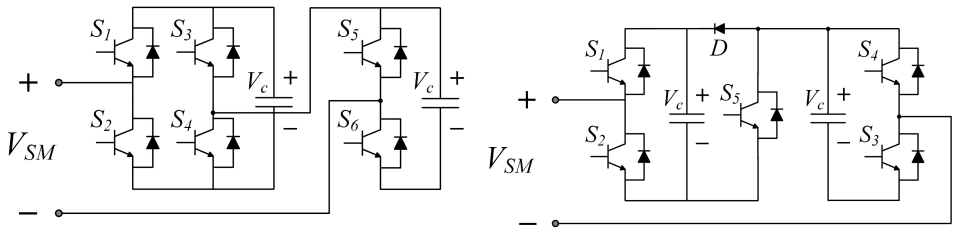

(a) Series-connection of full-bridge and half-bridge submodules.

(b) Hybrid submodule.

Figure 6.3: Simplification of the hybrid submodule.

Table 6.1: Switching states of hybrid submodule under normal operation [93].

Switching state	Switches						Submodule voltage
	S_1	S_2	S_3	S_4	S_5	S_6	V_{SM}
Insertion	ON	OFF	OFF	ON	OFF	ON	$2V_c$
	ON	OFF	OFF	ON	ON	OFF	V_c
	OFF	ON	OFF	ON	OFF	ON	V_c
Bypass	OFF	ON	OFF	ON	ON	OFF	0
Block	OFF	OFF	OFF	OFF	OFF	OFF	–

Table 6.2: Valve cost and power losses, normalized with respect to the conventional MMC [65].

Submodule topology	Valve cost [pu]	Power losses [pu]	DC-fault blocking
Conventional MMC	1.00	1.00	No
Full-bridge MMC	2.00	1.61	Yes
Hybrid MMC	1.50	1.31	Yes, cf. Eq (6.1)

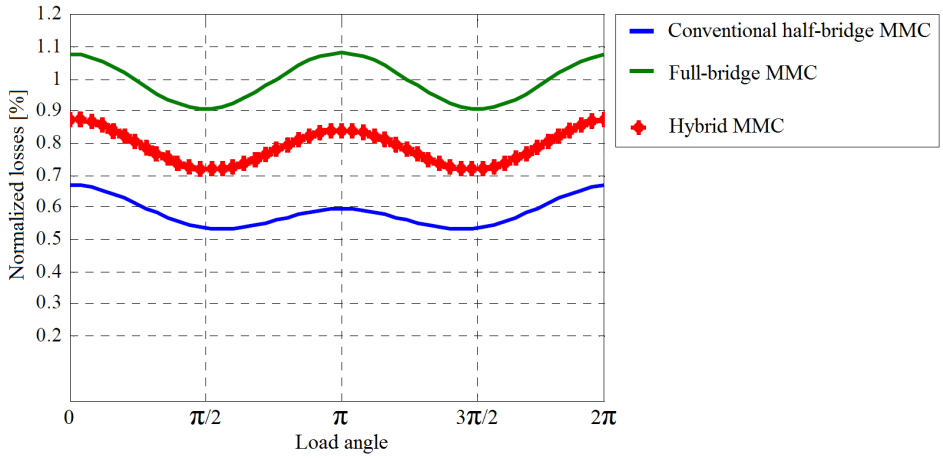

Figure 6.4: Normalized power losses at nominal apparent power as a function of power angle. Normalized with respect to the conventional MMC [65].

respect to the conventional MMC, with a normalized switching frequency of 3 which corresponds to 150 Hz. DC-fault blocking capability is also shown in Table 6.2 for the three different submodule configurations [65].

Despite the drawbacks presented in this section, the conventional, half-bridge MMC is chosen over the hybrid MMC for simplicity reasons. Additionally, viewed from a cost and loss perspective, the conventional MMC generates 31% less power losses and are ap-

parently 50% less costly (in terms of power semiconductor requirements) than the hybrid MMC.

6.2 Converter arm current

The next step in designing the MMC is to calculate the current flowing through the converter arm. This is an important parameter, because it directly influences the choice of power semiconductor devices. The current that the devices must be rated to handle can be found by calculating the current flowing in one arm of the MMC:

$$I_{arm} = \frac{I_{DC}}{3} + \frac{I_{RMS}}{2} + I_{marg} \tag{6.3}$$

where I_{DC} is the DC current from the battery ($I_{battery}$), I_{RMS} is the RMS phase current and I_{marg} is a current margin. This margin accounts for the circulating current within the MMC which in turn increases the rated current of power semiconductor devices [91]. The margin is assumed to be 15-20% of i_{RMS} at full load [27].

The DC current is determined by the proposed BESS configurations presented in Chapter 5. Three proposed BESS configurations were selected: BESS configuration 3, 5 and 6. The selection was based on a compromise between system reliability and the number of battery containers and hence, the system cost. According to Table 5.3 in Chapter 5, configuration 3 and 6 has a battery current of 2499.9 A, whereas configuration 5 has a battery current of 1666.7 A.

The RMS phase current, I_{ph}, can be found by the apparent power and the RMS phase voltage of the MMC. For the MMC, the apparent power simply becomes the required battery power of 180 MW divided by the system's power factor of 0.95, determined in Chapter 2 and 5. Thus, the apparent power of the MMC-BESS becomes 189.5 MVA. The MMC RMS phase voltage is determined by using the relationship between RMS line voltage and the DC voltage, then converting the RMS line voltage to RMS phase voltage dividing by $\sqrt{3}$:

$$V_{line,RMS} = \sqrt{\frac{3}{2}} V_{DC} \tag{6.4}$$

The common DC-link voltage, V_{DC}, is the resulting battery voltage of the proposed BESS configurations 3, 5 and 6. From Table 5.3, the battery voltages are 72 kV for configuration 3 and 6, and 108 kV for configuration 5. The RMS phase current is 1204.5 A for configuration 3 and 6, and 872.0 A for configuration 5. With the apparent power (S_{MMC}), the RMS phase voltage (V_{RMS}) and RMS phase current (I_{RMS}) of the MMC can be obtained by the following equation:

$$I_{RMS} = \frac{S_{MMC}}{3 \cdot V_{RMS}} \tag{6.5}$$

From Equation (6.4) and (6.5), the converter arm current, I_{arm}, of the MMC for the three proposed BESS configurations becomes 1640 A for configuration 3 and 6, and 1093 A for configuration 5, where the current margin, I_{marg}, of 15% of the RMS phase current,

i_{RMS}, is used. The calculations for the arm current of the MMC can be found in Appendix A.

6.3 Power semiconductor devices

The arm current of the MMC is an important parameter for selecting appropriate controllable power semiconductor devices. The two main candidates for high-power applications are the insulated-gate bipolar transistor (IGBT) and the integrated gate-commutated thyristor (IGCT) [51], [18]. It is assumed that the submodule diodes, as for the arm inductors and submodule capacitors, are sufficiently rated for the MMC and will not be further discussed as it lies beyond the scope of the thesis.

6.3.1 IGBT

IGBT is the most commonly used power semiconductor device for multilevel converters. Due to its low gate-power requirement and low switching losses, the IGBT replaced the gate turn-off (GTO) thyristors and bipolar junction transistors (BJT) in motor-drive applications during the 1990s. The IGBT has superior current conduction capability, as well as excellent forward and reverse blocking capabilities [8]. It offers scalability, meaning both series and parallel connection of IGBT can be made.

IGBTs are commercially available as power modules with freewheeling diodes. Different topologies and technologies exist, e.g. ABB offers single IGBT modules, phase-leg IGBT modules, choppers and dual IGBT modules. Figure 6.5a shows ABB's single IGBT module commercially termed HiPak, which is an IGBT connected with a freewheeling diode in anti-parallel [3]. HiPak modules are commonly used in demanding high-power applications such as traction, transmission and distribution, renewable energy (wind, solar) and industrial drives [2].

6.3.2 IGCT

The IGCT is a gate-controlled turn-off power semiconductor device. It turns off like a transistor but conducts like a thyristor, with very low conduction losses as well as negligible turn-on losses. The IGCT is well established in high-power and high-current applications due to its low losses, high surge current capabilities, achievable switching frequencies up to 1 kHz and simple mechanical integration. Additionally, like the IGBT the IGCT is also scalable in terms of both series and parallel connections, however snubbers are required [87].

Figure 6.5b shows the IGCT, with the gate-drive circuit integrated into the package of the device [3]. Unlike the IGBT, IGCTs do not come as standardized power modules, meaning additional semiconductor devices such as diodes must be chosen separately and in accordance to the voltage and current requirements of the system.

An overview over power semiconductor manufacturers and their IGBT power modules with maximum ratings are shown in Figure 6.6 and Table 6.3 [3], [41], [34], [60], [42], [40]. ABB's IGCT is also included in the overview.

(a) Single IGBT power module (HiPak). **(b)** IGCT power semiconductor device.

Figure 6.5: Controllable power semiconductor devices from ABB.

6.3.3 Comparison

Table 6.4 compares a number of characteristics and properties of the IGBT and IGCT. The choice of power semiconductor devices for the MMC submodules has a significant influence on the system's performance. Although IGBTs have had a dominating position in MMCs, IGCTs have gained a lot of attention due their desirable characteristics. High power ratings and low overall losses are key factors favouring the use of IGCTs in high-power applications, cf. Table 6.4. Low conduction losses of the IGCT is particularly

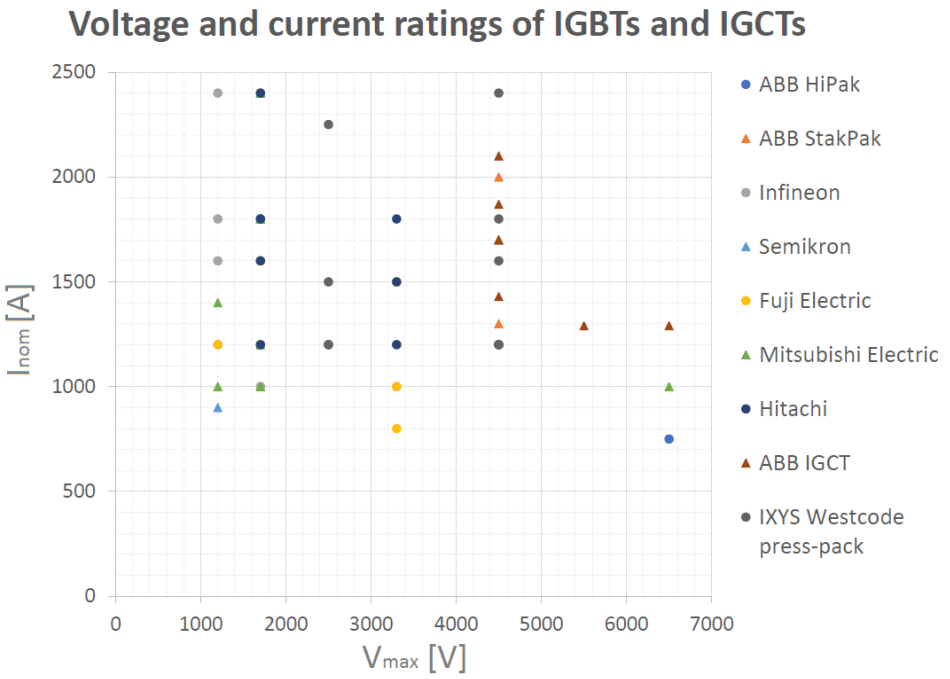

Figure 6.6: Overview of power semiconductor devices provided by different manufacturers. The ratings are for blocking voltages above 1000 V, and currents above 500 A.

advantageous, since MMCs utilize low switching frequencies of a few hundred hertz [68].

Regarding reliability, the IGCT is more reliable than the IGBT due to simpler construction yielding lower component-count. This also implies lower cost compared to the IGBT [51]. On the other hand, the IGBT is more reliable than the IGCT during short-circuit faults, yet the fault needs to be detected quickly and turned off within 10 μs. The IGCT must be protected as it lacks inherent current-limiting capability. Additionally, series- and parallel-connections are easier with IGBTs than with IGCTs [18].

Another important aspect is that converters with IGBTs has shown to generate less losses than IGCTs in applications which often work with strongly fluctuating power [18]. Since the MMC-BESS is connected to the AC grid to provide grid support during fluctuating power from the offshore wind farm, IGCTs may not be the preferable choice of power semiconductors from a loss perspective.

6.3.4 Press-pack IGBT

Ever since its commercialization in the 1980s [13], the IGBT have had many significant technological innovation contribution to size, loss and cost reduction of PCS' [46]. Recent advances in IGBT involve the technology termed press-packs. The IGBT press-pack provides low inductance and simple module stack suitable for high-power and high-voltage applications [55].

Additionally, the press-packs offer the potential for higher power capability, where the package is hermetically sealed and can be double-sided cooled. Simple mechanical stacking greatly simplifies for high-voltage applications. The press-packs also feature a short-circuit failure mode, allowing series-redundancy for high-voltage applications. This in turn simplifies the converter design even further, resulting in higher reliability and lower cost [55].

Press-pack IGBT modules are available from several manufacturers in the range of 2.5 to 6.5 kV, and with current ratings from 160 A to 3.0 kA for high-power applications. The module chosen for the MMC is the ABB's press-pack IGBT technology, commercially

Table 6.3: Power semiconductor ratings for blocking voltages above 1000 V, and currents above 500 A.

Manufacturer	Type	Voltage range [V]	Current range [A]
ABB	IGBT HiPak	4500-6500	750-1200
ABB	IGBT StakPak	4500	1300-2000
ABB	IGCT	4500-6500	1290-2100
Infineon	IGBT	1200-4500	1000-3600
Fuji Electric	IGBT (U and V series)	1200-3300	800-2400
Mitsubishi Electric	IGBT (HVIGBT)	1200-6500	1000-2400
Hitachi	IGBT	1700-4500	1200-2400
IXYS (Westcode)	IGBT PressPack	2500-4500	1200-2400
Semikron	IGBT	1200	900

Table 6.4: Characteristics and properties of IGBTs and IGCTs [18], [32].

Characteristics	IGBT	IGCT
Total loss	Medium	Low
On-state losses	High	Low
Turn-on losses	High (due to hard switching)	Low (due to clamp circuit)
Turn-off losses	Lower than a comparable IGCT	Higher than a comparable IGBT
Clamp losses	No (due to hard switching)	Yes
On-state voltage	High	Low
Turn-off capability	Low	High
Scalability	Yes, parallel and series	Yes, parallel and series (with snubber)
Series connection	Simple, gate unit control (dv/dt, active clamping) + static balancing resistor	Complex, bulky external balancing network
Parallel connection	Simple, low parameter deviation and adjustment by gate unit	Complex, bulky external balancing network
Switching time	Medium	Fast
Current sensing capability	No	No
Voltage scalability	Best	Good
Positive temperature coefficient	Good	Poor
Overvoltage limitation	Low stray inductance and suitable gate driving	By clamp circuit
Overload capacity	High	High
Clamp circuit	Necessary	Not required
Maximum surge current	Low	High
Short-circuit current	Limited	Not limited
Control power needed	Low	High

Figure 6.7: ABB's IGBT press-pack StakPak with six submodules.

named IGBT StakPak (4.5 kV and 1.3/2.0 kA), cf. Table 6.3. The StakPak submodule is shown in Figure 6.7 [3].

The press-pack IGBT modules are commonly used in applications where devices are series-connected mechanically and/or electrically, and where redundancy is required. Such applications can be HVDC transmission systems and FACT [2].

6.4 Number of submodules

The following step in designing the MMC-BESS is to determine the number of submodules required in the MMC. The number of submodules in one converter arm can be determined by the resulting battery voltage of the BESS, $V_{battery}$, and the blocking voltage of the power semiconductor devices, V_{block}:

$$N_{SM} = \frac{V_{battery}}{0.67 \cdot V_{block}} \tag{6.6}$$

where a safety margin of 67% (2/3) is used to get sufficiently large number of submodules in the converter arm to block the voltage, and V_{block} is the blocking voltage for the chosen power semiconductor device (i.e. power module) in the submodule. For ABB's StakPak power module, the rated blocking voltage is 4.5 kV, cf. Table 6.3. The number of submodules per converter arm with BESS configurations 3 and 6 becomes 24. Assuming a three-phase topology of the MMC, yields a total of six converter arms comprising of 144 submodules in total. For the BESS configuration 5, the number of submodules in one arm becomes 36, with a total of 216 submodules for the three-phase MMC. The latter topology shows a 50% increase in the number of submodules, implying higher cost of the converter for the same power module.

6.5 Power semiconductor voltage requirements

The power semiconductor devices chosen for the submodules of the MMC must be rated to handle the arm currents, as well as have a sufficiently high blocking voltage rating. The voltage each power semiconductor must be able to withstand is determined by the number of submodules, N_{SM}, found in the previous section, and the battery voltage , $V_{battery}$:

$$V_{SM} = \frac{V_{battery}}{N_{SM}} \tag{6.7}$$

The voltage each submodule, i.e. the power semiconductors, must be able to block is 3.0 kV for all three proposed BESS configurations. Since ABB's press-pack IGBT submodules is rated to withstand 4.5 kV under normal operating conditions, this voltage level lies within its blocking capability limits. The rated voltage of the StakPak is 50% higher than the required blocking voltage of each submodule, in addition to the safety margin added in Equation (6.6).

6.6 Proposed MMC configuration

Based on the proposed configurations of the BESS in Chapter 5, two different conventional MMC configurations can be realized as the PCS. These are summarized and presented in Table 6.5.

Table 6.5: Proposed MMC configurations for the 180 MW, 45 MWh BESS scheme.

Proposed BESS configurations	MMC				
	Arm current	Submodule voltage	Number of submodules per arm	Number of converter arms	Total number of submodules
	I_{arm}	V_{SM}	N_{SM}	N_{arm}	N
3, 6	1640 A	3.0 kV	24	6	144
5	1093 A	3.0 kV	36	6	216

CHAPTER 7

Structure of MMC-BESS

This chapter presents and compares different structures of the MMC-BESS described in Chapter 5 and 6. These include the implementation of centralized or distributed batteries, and the use of a transformer or DC-DC converters. Two different DC-DC converters are presented at the end of the chapter: the buck-boost converter and the active dual bridge converter. The advantages and drawbacks of each solution is discussed.

With the three proposed BESS configurations in Chapter 5, whereupon two different MMC configurations where suggested for the PCS, a total of three different MMC-BESS schemes could be realized. The MMC is based on the conventional, half-bridge MMC, where ABB's press-pack IGBT module StakPak is used, cf. Chapter 6. The rated voltage and current of the StakPak is 4.5 kV and 1.3 kA/2.0 kA[1]. The three different MMC-BESS schemes, termed I, II and III, are presented in Table 7.1. All MMC-BESS schemes are rated for 180 MW active power, and with an energy capacity of 45 MWh.

Figure 7.1 shows a single-line diagram of the investigated MMC-BESS scheme connected to the PCC via a line-frequency transformer. Apart from the PCS, additional requirement for any BESS includes a battery management system (BMS). The BMS measures the SoC, maintains a safe and optimal operation of each battery module and serves as a system supervisory control (SSC) to monitor the full MMC-BESS scheme. The BMS will not be further reviewed in this part[2], however it is important to account for in terms of additional power losses and cost of the whole system.

7.1 Centralized batteries versus distributed batteries

The MMC-BESS structure proposed in this thesis was initially based on a solution with centralized batteries, i.e. the batteries are connected across the common DC-link of the

[1] For StakPak with IGBT-to-diode ratio of 1.1.

[2] The SoC measurement will be regarded in the simulations in Part IV as a part of the BMS.

Table 7.1: Proposed systems for the 180 MW, 45 MWh MMC-BESS scheme.

	MMC-BESS	Manufacturer	Technology	Ratings	EssPro^{TM} Grid-containers in BESS ($N_s \times N_p$)	Submodules in MMC (per arm $\times$ no.of arms)
I	BESS 3 Press-pack IGBT	ABB ABB	EssPro Grid BESS StakPak	1.0 MW, 1.2 kV 4.5 kV, 2.0 kA	180 (60×3)	144 (24×6)
II	BESS 5 Press-pack IGBT	ABB ABB	EssPro Grid BESS StakPak	0.5 MW, 1.2 kV 4.5 kV, 1.3 kA	360 (90×4)	216 (36×6)
III	BESS 6 Press-pack IGBT	ABB ABB	EssPro Grid BESS StakPak	0.5 MW, 1.2 kV 4.5 kV, 2.0 kA	360 (60×6)	144 (24×6)

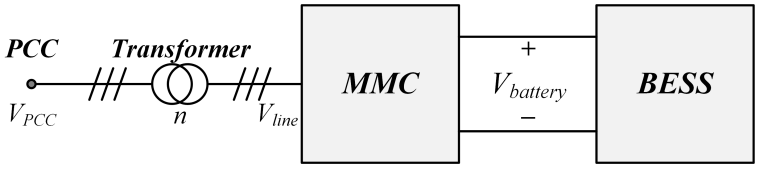

Figure 7.1: The structure of the investigated MMC-BESS scheme.

MMC. The drawback of the centralized battery-approach is the long battery strings required, which negate most of the advantage of the cascaded structure of the MMC [88]. Additionally, the efficiency decreases and the voltage requirements for the battery module increases [21]. Figure 7.2a shows the MMC with centralized battery-solution connected to the common DC-link.

To utilize the modular characteristic of the MMC, an approach with distributed batteries was proposed. This approach has shown to be the most feasible solution for large-scale BESS applications in terms of performance, redundancy and cost [88], [21]. The battery cells or modules are connected to each submodule, thereby forming an energy storage submodule [75]. Figure 7.2b shows the conventional MMC with distributed battery-solution, where a battery module is connected across the submodule capacitor, C, of the half-bridge.

7.2 Transformer versus DC-DC converter

The line-frequency transformer, cf. Figure 7.1, is used to step the AC grid voltage from several hundreds of kilo-volts at PCC (V_{PCC}) to several tens of kilo-volts (V_{line}) at the AC-side of the MMC[3]. The primary side (HV-side) of the transformer is connected to the

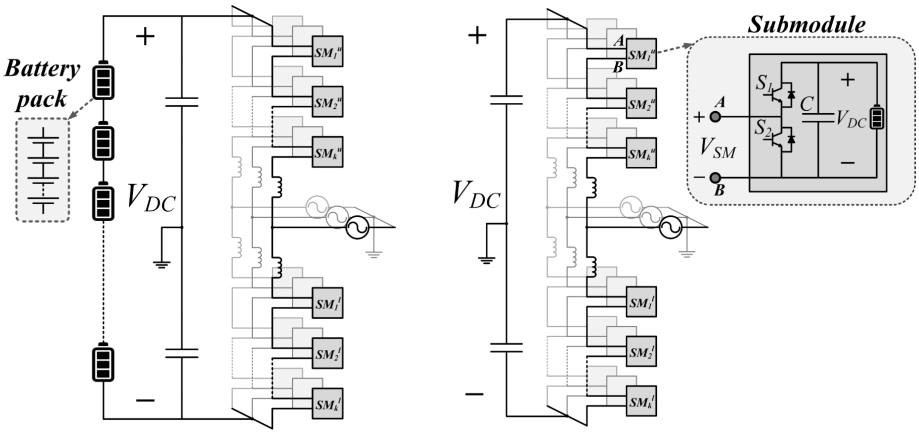

(a) MMC with centralized batteries.

(b) MMC with distributed batteries.

Figure 7.2: MMC with batteries for BESS applications.

[3] dependent on the battery-side DC-link voltage.

PCC, whereas the the secondary side (LV-side) is connected to the AC-terminals of the MMC. For the three proposed MMC-BESS schemes, the transformer turn ratio, n, is less than 5. For MMC-BESS scheme I and III, n is 4.54 (4.54:1), and for II n is 3.02 (3.02:1).

In an MMC-BESS scheme, it is desirable that the PCS is as efficient as possible since BESS' generally are lossy net energy consumers [88]. Adding a line-frequency transformer not only adds to the losses of the MMC-BESS scheme, but adds to the cost and space requirements as well. Moreover, faults or loss of one phase results in a complete shut down of the transformer, due to the common core shared for all three units[4].

Due to the abovementioned drawbacks of the line-frequency transformer, solutions with directly grid-connected MMC-BESS have been developed and proposed. These solutions are based on bidirectional DC-DC converter technology. Since the voltage at PCC is much higher than the voltage across a typical battery strings, a direct coupling cannot be made without stepping down the voltage. By employing DC-DC converters connected across each submodule the battery voltage can be stepped to the desired levels [88].

Using bidirectional DC-DC converters rather than a large, lossy transformer, offers several desirable advantages for the system. By connecting the battery to the DC-DC converter, the battery becomes decoupled from the submodule offering higher redundancy of the scheme [21]. Additionally, the required battery string voltages and the number of batteries needed can be reduced [88], and the battery charges and discharges with a better DC current [21]. These factors also help increase the expected life time of the batteries and lowers the system cost [88].

Two bidirectional DC-DC converter topologies are commonly considered for MMC with distributed batteries: the buck-boost converter and the dual active bridge (DAB) converter. The converter topologies are shown in Figure 7.3, where the main difference between the two topologies is the high-frequency isolation transformer, T, present in the DAB. The high-frequency transformer provides a galvanic isolation between the battery and the DC-link [21]. Due to its high frequency (commonly 5 to 20 kHz), the transformer becomes relatively small and light, however the insulation must be rated for the complete phase-to-ground voltage if the batteries are grounded [88].

One possible solution to go even further in reducing components, area and cost, while increasing the reliability of the MMC-BESS is to replace the 2L-VSC stations of the HVDC transmission system with MMCs. One of the converter stations could be implemented as the MMC-BESS, eliminating the original PCS from the scheme [21].

More specifically, one of the MMC-converter stations in the HVDC transmission system is implemented as a three-port MMC: the AC-side terminals of the converter is connected to the 400 kV AC grid, the split batteries are distributed on the DC-side of the DC-DC converter submodules, and the common DC-link of the MMC is connected to the HVDC-link of the HVDC transmission system. Figure 7.4 shows the new approach for the MMC-BESS as an HVDC converter station, and the topology is depicted in Figure 12.3.

With this approach the control flexibility, with a master-slave controlled HVDC transmission system, would be improved. Additionally, the overall power losses of the system would decrease, due to the 2L-VSCs suffering from high switching losses, which in turn

[4]If one unit of the transformer is defective, the core of this unit would quickly saturate due to the absence of an opposing magnetic field. This leads to greater escape of magnetic flux to the core metal enclosures, further heating the metallic parts to the point where fire might occur. Hence, a three-phase transformer must be shut down if any of the phases is defected [28].

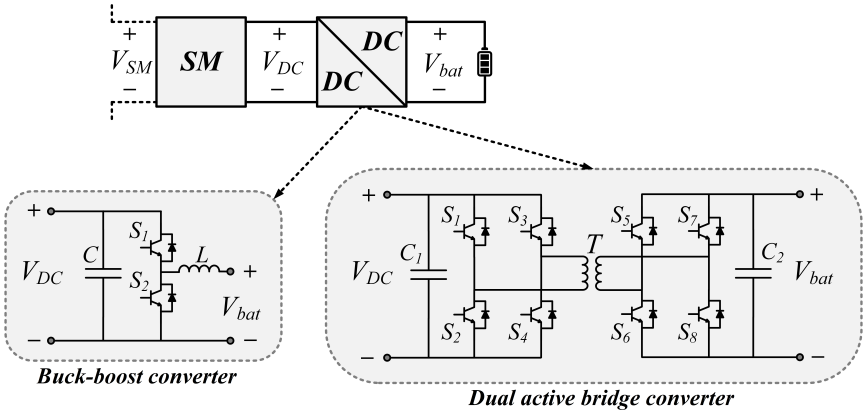

Figure 7.3: Submodule with DC-DC converter; buck-boost and dual active bridge converter.

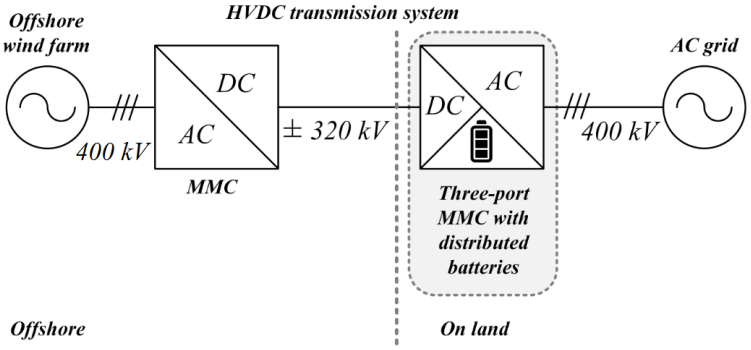

Figure 7.4: Three-port MMC with distributed batteries as a converter station for the HVDC transmission system. The common DC-link of the MMC-BESS is connected to the HVDC-link of the transmission system.

affects the efficiency of the transmission system. Furthermore, the MMC is able to exchange power with the AC grid and HVDC system. Currently, MMCs are the prevalent VSC technology for HVDC applications, and an increasing share of HVDC transmission systems are based on MMCs [16]. Thus, with the MMC the transmission current capability increases, power losses decreases, and the dynamic behaviour under external faults and fault ride-through gets optimized [7].

Part IV

Modeling and Simulation of MMC-BESS

CHAPTER 8

Modeling the MMC

This chapter offers a short review of different modeling approaches for converters, based on [69]. The chosen modeling approach of the MMC in this thesis is thoroughly presented, with assumptions and simplifications based on [70] and [25]. The controller structure as well as the controller tuning methods based on modulus optimum and symmetrical optimum, are describe and discussed. The response of the system is also analyzed and satisfactory operation of the controllers is verified by Bode diagrams.

8.1 Simplified models of the MMC

Full physics-based models of the MMC offer advantages such as great accuracy regarding internal dynamics, such as switching losses, circulating arm currents, submodule capacitor voltage ripple. However, such detailed and complex models are extremely time-consuming and usually not used for power system simulations [53], [69]. Consequently, average value models (AVMs) can be approximated by neglecting the switching dynamics, which uses significantly less computational time and resources without affecting. Different types of MMC models exist in the literature, which are presented in Table 8.1 [69].

8.2 Modeling approach

The modeling approach of the MMC in this thesis is based on the approach derived in [70] and [25], in order to investigate the external system dynamics effects. The simplified model of the MMC shown in Figure 8.1, is able to accurately represent the interface variable dynamics on the AC- and DC-side. These are generally considered as the main concern from a macroscopic viewpoint. The model comprises of a DC-side and an AC-side representation, as well as the power (energy) balance linking the two sides. The model is based on controlled voltage sources and does not contain any explicit submodules or switches (i.e. IGBTs with anti-parallel diodes). Therefore no modulation technique is applied. In theory, this modeling approach can support any modulation technique but

Table 8.1: MMC model types, from most complex and time-consuming to simpler, averaged models with significantly less computational time [69].

Model number	Model type	Description
1	Full physics-based model	Offers great accuracy in terms of switching losses, however the complex model is extremely time consuming. Not usually used for power system simulations.
2	Detailed non-linear IGBT-based model	Valves consisting of an ideal controlled switch and non-ideal diodes, offers great accuracy in modeling the IGBTs and conduction losses. High computational efforts for large numbers (thousands) of components. Manly used as an accuracy reference for validation of simplified MMCs.
3	Simplified IGBT-based model	The bidirectional switch represented by IGBTs and diodes are replaced by a two-state resistance: a small conductive value, and a large open-circuit value.
4	Detailed equivalent-circuit-based model	Based on model type 3 with circuit reductions of eliminating internal intermediate nodes and replacing each arm with a Thévenin equivalent. Offers advantages such as greatly improved computational performance, reduction of electrical nodes, and applicability to any number of submodules.
5	AVMs based on switching functions	IGBTs are not explicitly represented and the behavior of the MMC is modeled by controlled voltage and current sources. The models assume all internal variables being perfectly controlled, capacitors within the submodules being perfectly balanced and circulating currents perfectly suppressed. A converter loss function is included to account for the converter losses. Requires significantly less computational resources.
6	AVMs based on fundamental frequency	Based on model type 5, but suppresses the modulation block which results in keeping only the fundamental frequency-controlled AC-side voltage sources, DC-side remains the same. This further increase simulation times, as switching patterns are not represented.

for practical reasons, the NLM technique should used for higher number of levels since it offers higher efficiency. PWM-based and SVM techniques are cumbersome to implement for higher number of levels.

8.2.1 Simplified MMC model

The dynamics of the simplified MMC model are presented in Equation (8.1) to Equation (8.3), based on the synchronous reference frame (SRF) representation. The phase voltages and currents transformed in the SRF become DC-signals under balanced (sinusoidal) operating conditions [11]:

$$L_{AC}\frac{d\mathbf{i_{AC}}}{dt} = \mathbf{E} - \mathbf{v_{AC}} - R\mathbf{i_{AC}} - j\omega L\mathbf{i_{AC}} \tag{8.1}$$

$$L_{DC}\frac{di_{DC}}{dt} = -R_{DC}i_{DC} + v_{DC} - 2v_{CZ} \tag{8.2}$$

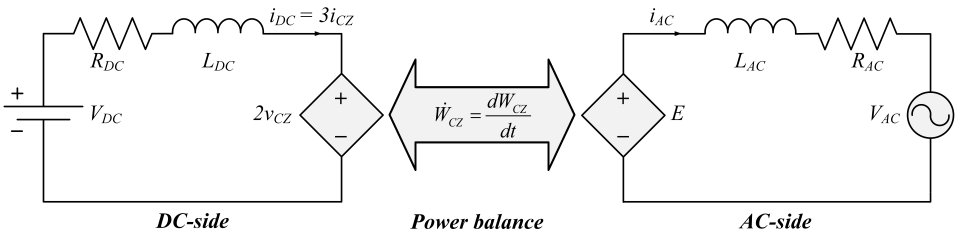

Figure 8.1: Simplified model of the MMC with AC-side and DC-side representation, as well as the power balance.

$$\frac{dW_{CZ}}{dt} = 2v_{CZ}\frac{i_{DC}}{3} - \frac{1}{2}\Re\{\mathbf{E}^*\mathbf{i_{AC}}\} \tag{8.3}$$

where $\mathbf{i_{AC}} = i_d + ji_q$ is the current on the AC-side in the SRF, driven by the internal AC-side voltage[1] (i.e. EMF) $\mathbf{E} = E_d + jE_q$, while $\mathbf{v_{AC}} = v_d + jv_q$ is the voltage at the PCC. The zero-sequence energy W_{CZ} is derived from the addition of the energy of the aggregated submodule voltages, i.e. the voltages of the upper and lower converter arms, then divided by 3. In Equation (8.3) of the zero-sequence energy, v_{CZ} denotes the zero-sequence voltage. This voltage drives the zero-sequence circulating current i_{CZ}, where the relation between this current and the current of the DC-side of the MMC can be given as:

$$i_{CZ} = \frac{1}{3}i_{DC} \tag{8.4}$$

The zero-sequence circulating current, i_{cz}, is the parameter responsible for the active power transfer of the MMC. Furthermore, the AC-side equivalent resistance and inductance are defined as:

$$R_{AC} = R_f + \frac{R_a}{2} \tag{8.5}$$

$$L_{AC} = L_f + \frac{L_a}{2} \tag{8.6}$$

where R_{AC} and L_{AC} are the AC-side equivalent output filter resistance and inductance, and R_a and L_a are the equivalent resistance and inductance of the MMC's arm inductor. The DC-side equivalent resistance and inductance of the MMC are defined by the following relation using the arm resistance and inductance as shown below:

$$R_{DC} = \frac{2}{3}R_a \tag{8.7}$$

$$L_{DC} = \frac{2}{3}L_a \tag{8.8}$$

[1] In contrast to the 2L-VSC, the MMC does not provide a physical, measurable AC-side voltage [73].

8.2.2 MMC base values

Power system-quantities, i.e. voltage, current, impedance and power, are commonly expressed in per units that are percentages of specified base values. The per unit-system offers great advantages by making calculations and comparisons easier and more efficient when considering dimensionless values instead of real, numeral SI-values. Any quantity can be converted into per unit-quantity simply by dividing the real value by a base or reference value [36].

The base values are calculated based on the given base apparent power, S_b, and the base voltage, V_b, of the MMC. The values are phase quantities, i.e. the base voltage in this case is the AC RMS phase voltage and as a result the given nominal line voltage, $V_{line,RMS}$, of the system must be divided by $\sqrt{3}$. Thus, the following base values are defined below for the AC-side and the DC-side, respectively. All base values are denoted with a subscripted b.

AC-side base values

For a given S_b and V_b the following base values of the MMC are derived [70]. All AC-side base values are denoted with subscripted AC. The base electrical speed ω_b is common for both sides of the MMC:

$$S_b = S_{AC,b} \tag{8.9}$$

$$V_b = V_{AC,b} \tag{8.10}$$

$$I_{AC,b} = \frac{2}{3} \cdot \frac{S_{AC,b}}{V_{AC,b}} \tag{8.11}$$

$$Z_{AC,b} = \frac{V_{AC,b}}{I_{AC,b}} \tag{8.12}$$

$$\omega_b = 2\pi f_b \tag{8.13}$$

$$L_{AC,b} = \frac{Z_{AC,b}}{\omega_b} \tag{8.14}$$

$$C_{AC,b} = \frac{1}{Z_{AC,b} \cdot \omega_b} \tag{8.15}$$

where f_b is the base system frequency of 50 Hz.

DC-side base values

The DC-side base values of the MMC are derived accordingly [70]. All DC-side base values are denoted with subscripted DC:

$$P_{DC,b} = S_{DC,b} = S_{AC,b} = S_b \tag{8.16}$$

$$V_{DC,b} = 2\sqrt{\frac{2}{3}} \cdot V_{line,RMS} = 2V_{AC} \tag{8.17}$$

$$I_{DC,b} = \frac{S_b}{V_{DC,b}} = \frac{3}{4} I_b \tag{8.18}$$

$$Z_{DC,b} = \frac{V_{DC,b}}{I_{DC,b}} \tag{8.19}$$

$$L_{DC,b} = \frac{Z_{DC,b}}{\omega_b} \tag{8.20}$$

$$C_{DC,b} = \frac{1}{Z_{DC,b} \cdot \omega_b} \tag{8.21}$$

where the base apparent power is the same for both AC- and DC-side.

Zero-sequence energy

Derived from the power balance, the zero-sequence energy base and reference are given as [70]:

$$W_b = \frac{S_b}{\omega_b} \tag{8.22}$$

$$W_{ref} = 2 \cdot N_a C_{eq} V_b^2 \tag{8.23}$$

where N_a is the number of arms per phase leg of the MMC, and C_{eq} is the DC-side equivalent capacitance for a certain number of submodules per arm.

8.2.3 MMC parameters

The converter parameters are defined as pu-values and are based on the paper in [70], and are presented in Table 8.2.

Table 8.2: Converter data in per unit values for the simplified MMC.

Converter parameter	Symbol	Per unit-value
Filter resistance	R_f	0.0032
Filter inductance	L_f	0.1229
Arm resistance	R_a	0.0030
Arm inductance	L_a	0.0480
AC-side equivalent resistance	R_{AC}	0.0047
AC-side equivalent inductance	L_{AC}	0.1469
DC-side equivalent resistance	R_{DC}	$7.5212 \cdot 10^{-4}$
DC-side equivalent inductance	L_{DC}	0.0120
Submodules per arm	N_{valve}	200
DC-side equivalent capacitance	C_{eq}	0.0042

8.3 MMC controller design

The overall control structure of the modeled MMC, illustrated in Figure 8.2, is based on multiple control loops connected in a cascaded manner. The proportional integral (PI) controller, due to its simple structure and robustness [11], has proven to be a success in the power electronic industry [70]. A block diagram of a general PI controller is shown in Figure 8.3, where the output of the system (Y) is measured against a reference value (Y^*), where the deviation (error E) is the input of the PI controller. A disturbance term (D) is subtracted from the signal, which improves the controller performance. U is the PI controller output. The mathematical approach of the PI controller in Figure 8.3 in the Laplace domain with respect to the controller output can be expressed as [70]:

$$U = (Y^* - Y)(K_p + \frac{K_i}{s}) - D = E(K_p + \frac{K_i}{s}) - D \tag{8.24}$$

Since this is a simplified MMC model without any modulated switches, only controllers at top-level are realized. From Figure 8.2 it can be shown that the zero-sequence energy controller provides a reference for the active component of the grid current, i_d^*, to the AC current controller. The AC current controller further regulates the direct-axis current, i_d, to follow this reference and the output is an AC voltage reference, E, directly fed to the controlled voltage sources of the MMC's AC-side. The zero-sequence energy controller acts as the outer loop controller, whereas the AC current controller acts as the inner loop controller. The quadrature-axis current, i_q, is set to follow a reference of zero ($i_q^* = 0$). The DC current controller is implemented as a single control loop, which controls the zero-sequence circulating current, i_{CZ}, to follow its reference value, $i_{CZ}^* = 3i_{DC}^*$.

The block denoted 'PLL' in Figure 8.2 is the phase-locked loop controller, providing phase and frequency information of the AC grid voltage. It is based on a feedback control system which is able to generate an input signal, whose phase and frequency are synchronized with an output reference signal. It is an important part for ensuring normal operation and control of the MMC [35].

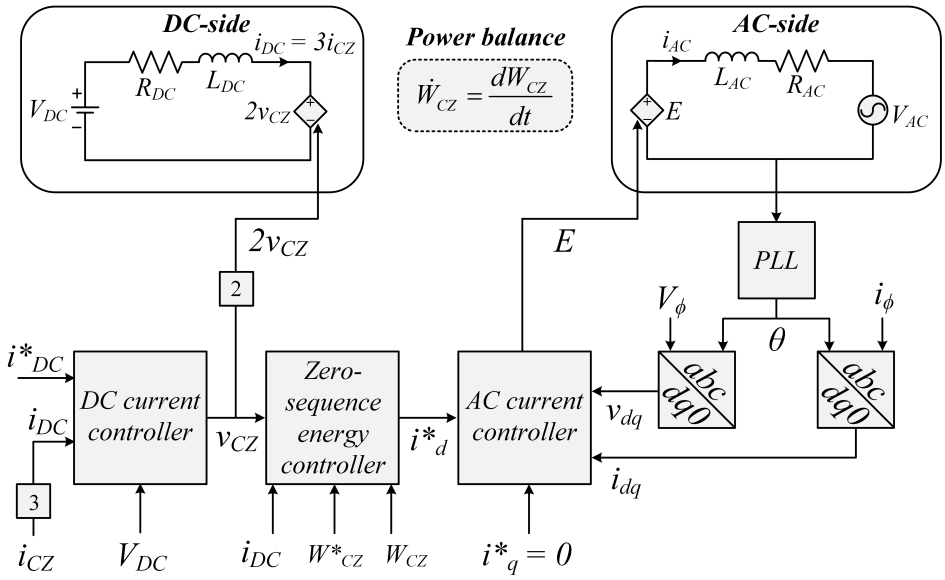

Figure 8.2: Block diagram of the simplified MMC with its associated controllers. All reference values are denoted with *.

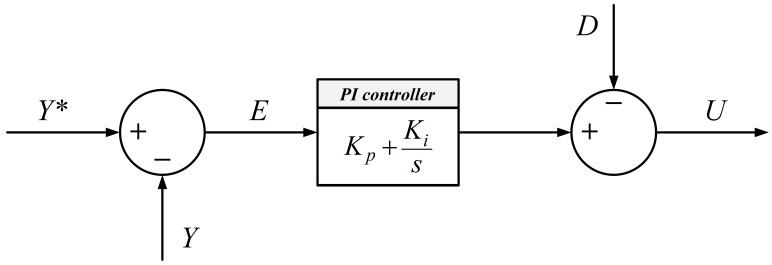

Figure 8.3: Block diagram of the PI controller in the Laplace domain.

8.3.1 Tuning of PI controllers

The objectives of a PI controller are to ensure fast response of the system, with minimal overshoot and adequate damping of oscillations. To achieve fast response the cut-off frequency, f_{co} is set to a large value of $40 \times f_b = 2kHz$. The selection of PI controller-parameters is one of the main factors influencing stability and dynamic performance of the control system of the converter. Two well-established tuning techniques commonly used for the tuning of PI controllers of grid-connected VSCs exist: modulus optimum and symmetrical optimum [11], [79]. The transfer function of a general PI controller is given as:

$$G(s) = K_p + \frac{K_p}{T_i s} = K_p + \frac{K_i}{s} \tag{8.25}$$

where K_p is the proportional gain, T_i is the controller time constant, K_i is the integral gain, the and $s = \sigma + j\omega$ is the complex Laplace-variable.

Modulus optimum

Modulus optimum criterion, or absolute value optimum criterion, is often used for low order-controlled systems (order less than 3), due to its simplicity and fast response [11]. If the controlled system has one dominant time constant and one minor time constant, the modulus optimum criterion is applied. This tuning technique is based on keeping the magnitude of the closed loop-transfer function equal to 1 for a wide frequency range as possible. This implies that the dominant time constant (pole) of the controlled system is cancelled, and the gain is selected to ensure that the relative damping of the closed loop-transfer function is given as $\varsigma = (\sqrt{2})^{-1}$ [79]. The frequency of the system's natural oscillation is given as $\omega_n = (T_a\sqrt{2})^{-1}$, where T_a accounts for the approximated, first-order delay time caused by the switches in the converter. T_a is thus a function of the switching frequency, f_{sw} [11]. The controller parameters for the modulus optimum criterion are given as [70]:

$$K_p = \frac{T}{2kT_f}, \qquad K_i = \frac{K_p}{T_i}, \qquad T_i = T \tag{8.26}$$

where T_f represents the dynamics of the filters and modulation of the converter, and k is a generic constant.

Symmetrical optimum

Symmetrical optimum criterion is applied when the controlled system has one of its pole near the origin or at origin itself (results in a marginally stable system). Cancellation of the dominating pole would lead to a double-pole at the origin, which in turn leads to system instability [56]. Thus, modulus optimum tuning technique cannot be applied. The benefit of tuning the controller according to symmetrical optimum is an enhanced phase margin, meaning the system is able to tolerate more delays. Additionally, the tuning criterion has shown to have a good disturbance rejection [11]. The symmetrical optimum criterion is obtained by using the Nyquist stability-criterion [12], and the controller parameters are given as [70], [25]:

$$K_p = \frac{\omega_m}{b}, \qquad \omega_m = \sqrt{pz}, \qquad K_i = \frac{K_p}{\alpha T_{eq}}, \qquad T_{eq} = 2T_f \tag{8.27}$$

where ω_m is the geometric mean of the zero and pole, b is a per unit-scaling factor, $p = T_{eq}^{-1}$ is the pole of the inner loop, $z = p\alpha^{-1}$ where α is a gain provided by the designer which is greater than 1.

A cascaded control system requires an inner loop control which can achieve fast response, whereas the outer loop control is responsible for stability and optimal regulation with respect to disturbances. For this case, it implies that the AC current controller is tuned

according to the modulus optimum criterion, and the zero-sequence energy controller is tuned according to the symmetrical optimum criterion [70].

A general, second-order transfer function of the controlled system, $H_c(s)$, is given by Equation (8.28). The transfer function represents the current behavior of the AC- and DC-side including the dynamics of switching and filters of the MMC:

$$H_c(s) = \frac{k}{(1+Ts)(1+T_f s)} \tag{8.28}$$

In Equation (8.28) above, the AC current controller will have the parameters:

$$k = \frac{1}{R_{AC,pu}} \qquad \text{and} \qquad T = \frac{L_{AC,pu}}{\omega_b R_{AC,pu}} \tag{8.29}$$

whereas the DC current controller will have the parameters:

$$k = \frac{1}{R_{DC,pu}} \qquad \text{and} \qquad T = \frac{L_{DC,pu}}{\omega_b R_{DC,pu}} \tag{8.30}$$

By using Equation (8.25), the PI current controllers can be referred to $G(s) = G_c(s)$. The PI controller for the zero-sequence energy will have a slightly different form, due to the pole p and gain α, cf. Equation (8.27):

$$G_e(s) = K_p + \frac{K_p z}{\alpha s} = K_p + \frac{K_p}{2\alpha T_f s} \tag{8.31}$$

The open-loop transfer function of the controlled current system (AC or DC current) can be obtained from Equation (8.25) and Equation (8.28):

$$H_{ol}(s) = H_c(s) \cdot G_c(s) \tag{8.32}$$

By including the feedback term in Equation (8.32), the closed-loop transfer function of the controlled current system becomes:

$$H_{cl}(s) = \frac{H_c(s) \cdot G_c(s)}{1 + H_c(s) \cdot G_c(s)} = \frac{H_{ol}(s)}{1 + H_{ol}(s)} \tag{8.33}$$

The closed-loop transfer function of the inner control loop, i.e. the AC current controller, is a second-order system in the from of:

$$H_{cl}(s) = \frac{0.5}{(T_f s)^2 + T_f s + 0.5} \tag{8.34}$$

By approximating the second-order system in Equation (8.34) to a first-order system, the transfer function of the inner loop controller becomes:

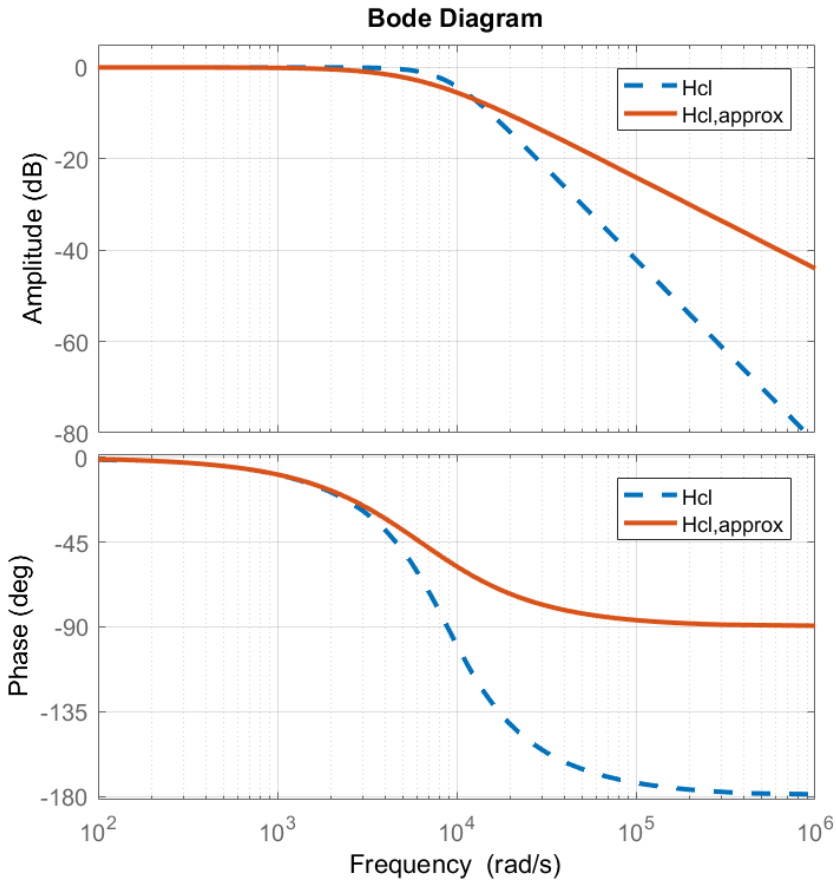

Figure 8.4: The approximated first-order model $H_{cl,approx}(s)$ compared with the second-order system $H_{cl}(s)$.

$$H_{cl}(s) = \frac{0.5}{(T_f s)^2 + T_f s + 0.5} \qquad \longrightarrow \qquad H_{cl,approx}(s) = \frac{1}{T_{eq} s + 1} \tag{8.35}$$

This approximation is used in the design of the controllers, and are presented in a Bode diagram with their amplitude and phase response in Figure 8.4.

The outer control loop, i.e. the zero-sequence energy controller, can be determined by making $T_{eq} = 2T_f$. A block diagram of the closed-loop systems with their respective controllers are shown in Figure 8.5.

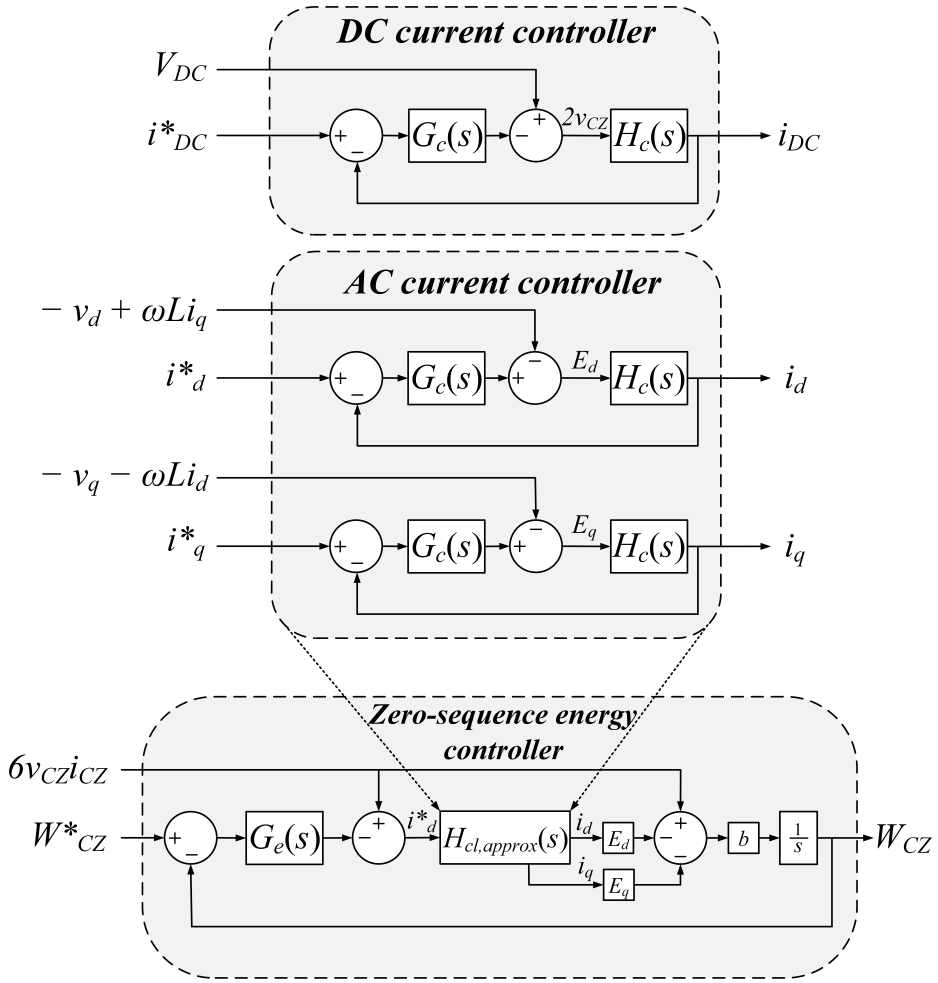

Figure 8.5: Closed-loop systems and their respective controllers. All parameters are expressed in per unit-values.

As aforementioned, the AC and DC current controllers are tuned according to modulus optimum by Equation (8.26), whereas the zero-sequence energy controller is tuned according to symmetrical optimum by Equation (8.27). Table 8.3 presents the parameters of the controllers.

8.3.2 The response of the systems

Figure 8.6 shows the Bode diagrams with amplitude in decibels (dB) and phase in degrees of the closed-loop current controllers and the zero-sequence energy controller. Since the amplitude response is close or equal to 0 dB, the measured values will therefore be equal

to the reference value. The phase is close or equal to 0 degrees, which implies that the output of the system will not lag. Thus, the aim is to achieve 0 dB at 0 degrees [12].

The bandwidth of the system gives an indication of how fast the system is responding, and is determined by the frequency at which the response of the close-loop amplitude response falls to -3 dB. The bandwidth or the cut-off frequency is the frequency at which the controller is unable to follow the reference [63]. To ensure a proper function of the cascaded control system the inner loop controller has to act faster than the outer loop controller, implying that the AC current controller must be faster than the zero-sequence energy controller. This is shown by analyzing the bandwidths of the systems; the amplitude responses of the current controllers[2] fall after the amplitude response of the zero-sequence energy controller. This corresponds to the bandwidth of the current controllers being larger than the bandwidth of the zero-sequence energy controller.

Figure 8.6 also shows the damping responses of the systems. The zero-sequence energy controller is slightly overshooting at $2 \cdot 10^3$ rad/s before falling below 0 dB. This implies that the system is slightly underdamped. The current controllers, however, both fall cleanly away from 0 dB at $5 \cdot 10^3$ rad/s, showing that they are critically damped.

Table 8.3: Parameters of the AC current, DC current and zero-sequence energy controller of the MMC.

Controller	Parameters						
	K_p	K_i	T_i	T_{eq}	ω_m	b	α
AC current controller	3.6	37.6691	0.0955	–	–	–	–
DC current controller	2.0	12.5664	0.1592	–	–	–	–
W_{CZ} controller	233.9371	$2.3398 \cdot 10^5$	–	$1.5915 \cdot 10^{-4}$	$2.5651 \cdot 10^3$	10.9649	6

[2]The Bode diagram of the AC and DC current controller coincide, meaning that they are acting equally fast.

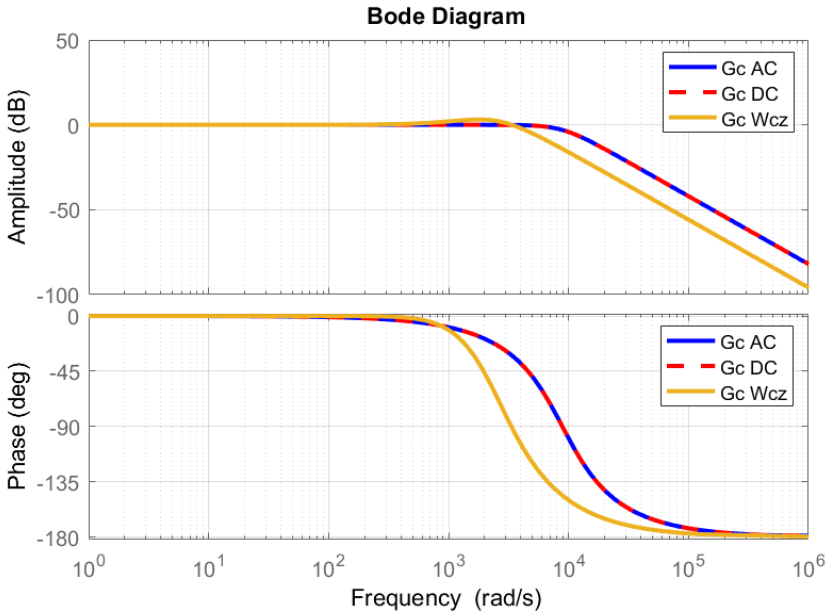

Figure 8.6: Bode diagram of the closed-loop transfer function of the current controllers and the zero-sequence energy controller.

CHAPTER 9

Modeling the Battery

This chapter briefly presents and explains some of the common methods of modeling a battery for simulation purposes. The battery model chosen to represent the centralized battery in the MMC-BESS model is based on the linear battery modeling approach. An SoC measurement is included at the end of this chapter for monitoring the charging and discharging processes of the battery.

When considering a battery model, one major challenge is the non-linear characteristic of the parameters in the equivalent circuit. Although fully physical battery models are more precise, they also result in great computational effort as well as being highly time-consuming. As a result to overcome these drawbacks, five basic battery models can be considered: ideal, linear, modified, Théveninv and improved Thévenin. The simplified battery models are shown in Figure 9.1, where V_{bat} represents the voltage at the terminals of the battery and E_o is the open-circuit voltage [67], [20]. Figure 9.2 shows the equivalent circuit of the improved Thévenin batter model.

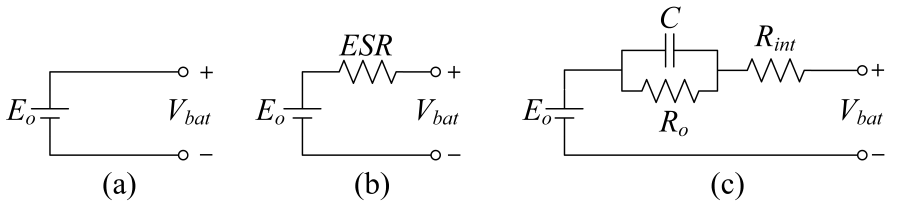

Figure 9.1: Basic battery models: (a) ideal, (b) linear or simplified, and (c) Thévenin model.

9.1 Ideal Battery Model

This battery model is the most simplified one, consisting of only an ideal voltage source which depicts an ideal battery and an open-circuit voltage, thus ignoring the internal parameters of the battery [67].

9.2 Linear battery model

This is a widely used battery model, consisting of an ideal voltage source as the battery and a constant internal equivalent series resistance, ESR. However, the model does not consider the varying characteristics of the internal impedance for varying SoC, concentration of electrolyte and sulfate formation [67], [20].

9.3 Modified battery model

By making ESR no longer constant, but rather varying it with the SoC a modified battery model can be made. This improved model proposed by J. P. Cun has been used by battery manufacturers for battery monitoring purposes [20].

9.4 Thévenin battery model

Another commonly used battery model is the Thévenin battery model. It consists of an open-circuit voltage, an internal resistance, a capacitance, and an over-voltage resistance The capacitance is the capacitance of the parallel plates, and the over-voltage resistance depicts the non-linear resistance offered by the contact resistance of the plate to the electrolyte. All elements are assumed to be constants [67], [20].

9.5 Improved Thévenin battery model

Since the Thévenin battery model presented in the previous section does not evaluate the battery conditions accurately, a new approach was proposed termed Improved Thévenin battery model. An electrical equivalent circuit model is shown in Figure 9.2, where the main circuit model comprises of several subciruits:

- E_{bat}: The voltage in the battery cells, represented as a DC voltage source.
- E_{polar}: The polarization effect[1].
- E_{temp}: The temperature effect on the terminal voltage of the battery.
- R_{bat}: The internal resistance of the battery. This value mainly depends on the relation between the battery's cell voltage and SoC.

[1] The polarization effect is due to the availability of active material in the battery cell.

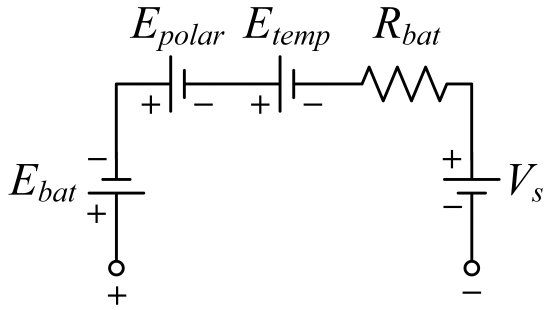

Figure 9.2: The battery equivalent circuit of the improved Thévenin battery model.

- V_s: A voltage source with 0 V, which is used to record the battery current.

By introducing these subcircuits, the battery model is capable of handling different modes of charge and discharge. Thus, the model is comparatively more precise, and only a few modifications are required in order to vary battery parameters such as load state, current density and battery temperature [67].

Since internal dynamics of the batteries in the MMC-BESS is not the main objective of the thesis, a simpler battery model with fewer parameters is chosen. Hence, the preferred battery model for modeling the MMC-BESS is based on the linear battery model described in section 9.2. A screenshot of the modeled battery in Matlab® Simulink is presented in Figure 9.3, where $Vbat$ is the battery terminal voltage and ESR is constant internal equivalent series resistance. The internal dynamics of the batteries are ignored without compromising the simulation results, and are therefore set to be 0.001 Ohm.

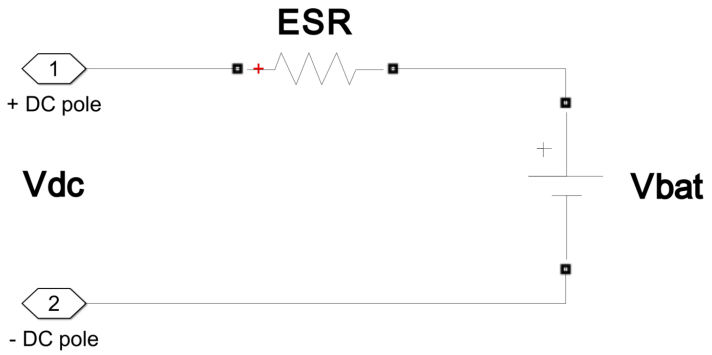

Figure 9.3: Centralized battery modelled as a linear battery model in Matlab® Simulink.

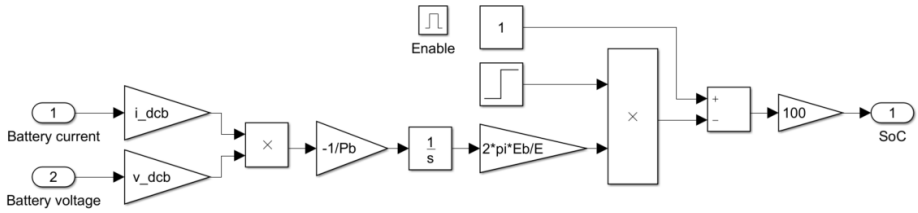

Figure 9.4: SoC measurement for the modeled battery in Matlab® Simulink.

9.6 State-of-charge monitoring

One of the major functions of the BMS is to determine the SoC of the batteries. The SoC equation based on the coulomb counting method [62] is given by:

$$SoC(t) = SoC(t_0) + \frac{1}{C_{bat}} \int_{t_0}^{\tau} (I_{bat} - I_{loss}) dt \tag{9.1}$$

where $SoC(t_0)$ is the initial SoC, C_{bat} is the rated capacity in ampere-hours, I_{bat} is the battery current, and I_{loss} is the current consumed by loss reactions. Figure 9.4 shows a screenshot of the SoC equation implemented in the MMC-BESS model. By modifying Equation (9.1), the battery power is integrated by the means of an integrator block to obtain the measured energy in the circuit. Furthermore, the energy is divided by the energy capacity where the system base frequency is used as the time base. The initial SoC in Figure 9.4 is 100%, i.e. the battery is fully charged, shown by adding 1 to the measured SoC.

CHAPTER 10

HVDC Transmission System Model

The aim of this chapter is to offer technical information and elaboration on the HVDC transmission system model, controllers and controller parameters. The active power flow of the HVDC model is presented. A Bode diagram of the controllers is given and their amplitude and phase response are briefly examined. The HVDC model was provided by Prof. Tedeschi and Post.doc. Sanchez Acevedo at the Department of Electric Power Engineering, NTNU.

A multi-terminal (MT) HVDC transmission system was provided in order to assemble the full system, with the MMC-BESS connected to the PCC of the HVDC transmission system and the AC grid. The HVDC system is modeled as a point-to-point transmission system with subsea cables (underwater or underground cables) for bulk power transmission. The HVDC system is based on VSC technology, where the converter stations comprises of a 2L-VSC. The cable length is 200 km, and it is obvious that the cable is too long for an HVAC transmission system to be made possible, cf. Chapter 1.

Furthermore, the converters in each converter station are modelled as average model-based 2L-VSCs, with a similar cascaded control scheme as for the simplified MMC presented in Chapter 8. For the point-to-point VSC-based HVDC transmission system employed for the connection of the offshore wind farm with the AC grid on land, the VSC station offshore controls voltage and frequency of the offshore AC network. The onshore VSC station has the function of controlling the HVDC-link voltage [15].

This centralized control strategy is known as master-slave control, which is an extension of the conventional point-to-point control of HVDC transmission systems: The master terminal (master-node or slack bus) controls the DC voltage in the MT-HVDC transmission system, and the rest (slave-nodes) control the current flow, and thus the power flow. Other control strategies, where the DC voltage control is shared between two or more converters, are based on voltage-droop control [85].

Figure 10.1 shows the per unit active power, DC current and DC voltage of the master and slave converters. A bidirectional power flow is demonstrated, where the DC current,

I_{DC}, is defined as positive when flowing into the HVDC-link and negative when flowing into the AC grid for the master converter. For the slave converter, the defined power flow is opposite. The HVDC-link voltage, V_{DC}, is constant and equal to 1.0 pu and results in the active power and DC current being identical:

$$V_{DC} = 1.0 \text{ pu} \longrightarrow P_{DC} = I_{DC} \tag{10.1}$$

When the DC current direction is defined as above, the direction of the active power flow in an HVDC transmission system can easily be visualized by Figure 10.2. In (1) the DC current (and hence the active power) flows from master to slave for $0 \leq t < 10.4$ seconds, while in (2) the DC current is in the opposite direction, flowing from slave to master for $10.4 < t < 15.4$ seconds. In (3) the DC current flows as for case (1), for $15.4 < t \leq 20.0$ seconds.

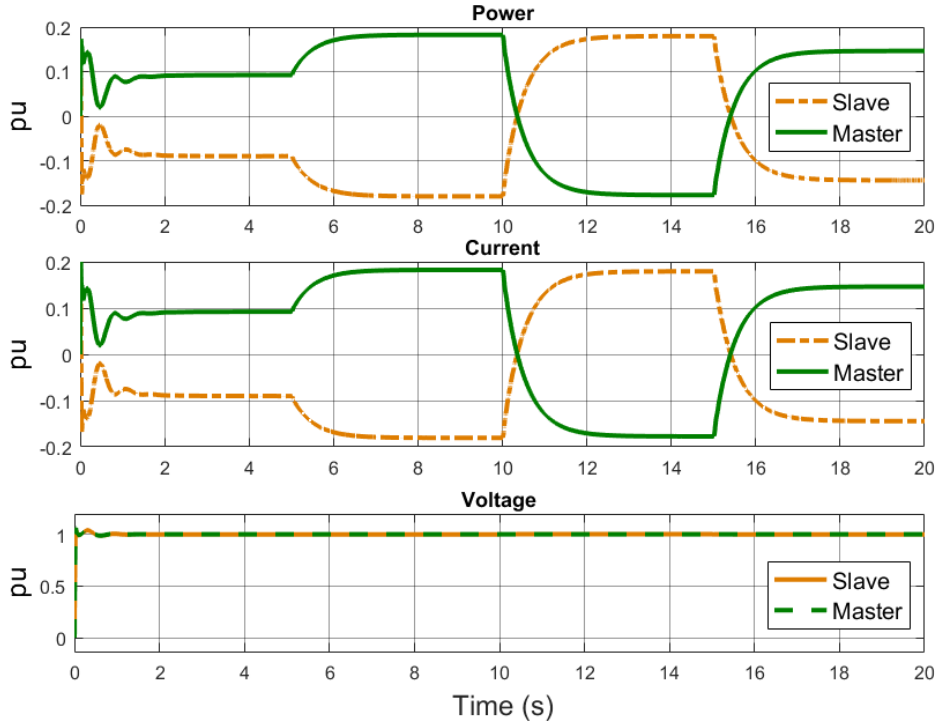

Figure 10.1: Master-slave configuration: power, current and voltage of the master and slave converters.

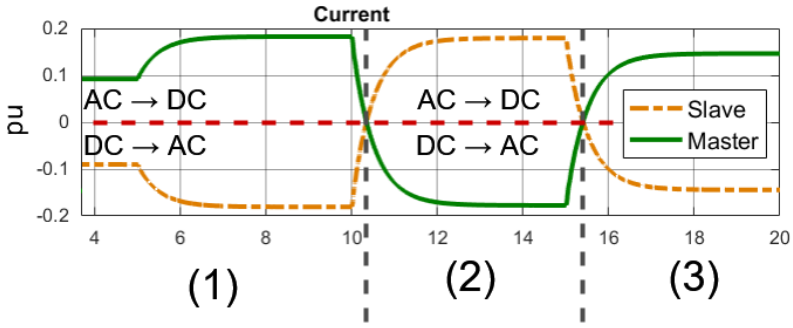

(a) Graphs showing the master-slave currents in pu-values.

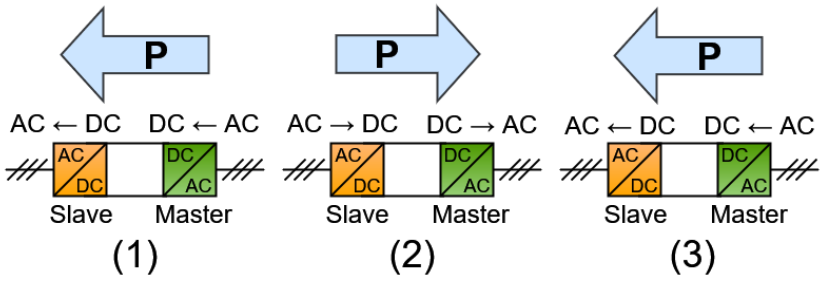

(b) The direction of active power flow.

Figure 10.2: Active power flow in the HVDC transmission system model.

Figure 10.3 shows an overview of the HVDC transmission system connecting the wind farm to the onshore AC grid. The PCC is where the MMC-BESS is connected through a line-frequency step-down transformer. The HVDC cable is modelled as a PI line model, where shunt capacitance and shunt conductance are connected across the converter's DC-side terminals. The parameters and values used in the simulation can be found in Appendix C.

The controllers used in the HVDC transmission system are the same as for the modeled simplified MMC. For the master converter the PI controller of the inner loop (AC current controller) are tuned according to modulus optimum criterion, whereas the PI controller of the outer loop (DC voltage controller) is tuned according to symmetrical optimum.

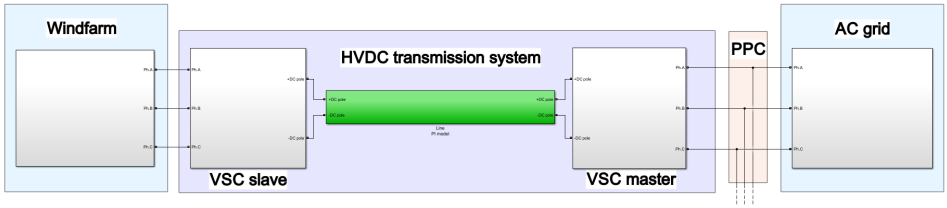

Figure 10.3: Screenshot of the HVDC transmission system modeled in Matlab® Simulink.

Table 10.1: Parameters of the AC current controller and DC voltage controller of the VSC-HVDC transmission system.

Controller	Parameters				
	K_p	K_i	T_i	T_{eq}	T_a
AC current controller	0.6764	8.3333	0.0508	–	$7.9577{\cdot}10^{-5}$
DC voltage controller	0.0650	9.0243	–	$1.5915{\cdot}10^{-4}$	$7.9577{\cdot}10^{-5}$

The PI controller of the slave converter is an AC current controller tuned according to modulus optimum as well. The q-axis current of the HVDC transmission system is set to follow a reference of zero, i.e. no q-axis current should flow in the system. The controller parameters of the converters in the HVDC transmission terminals are presented in Table 10.1.

Bode diagrams of the current and voltage controllers, $G_c\,AC$ and $G_c\,DC$ respectively, are shown in Figure 10.4. The magnitude and phase response of the first order systems show that the controllers have good response, with only a minimal overshoot for the DC voltage controller. Given that the AC current controller is the inner loop controller, it must act faster than the outer loop DC voltage controller providing its reference for proper operation.

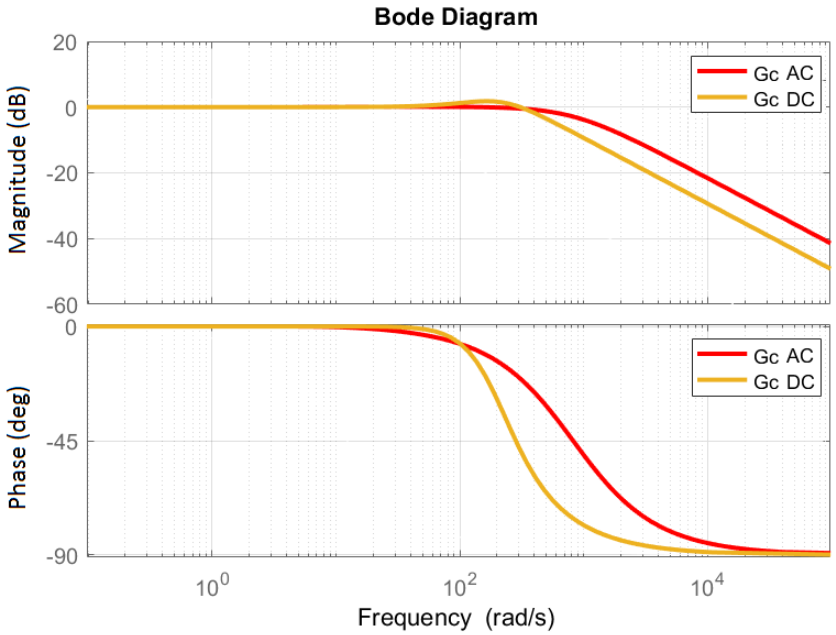

Figure 10.4: Bode diagram of the closed-loop transfer function of the AC current controller and the DC voltage controller.

CHAPTER 11

Simulations and Results of MMC-BESS

This chapter presents the results of three test cases. Test case 1 presents the results of the bidirectional power flow of the MMC-BESS, whereas test case 2 presents the results of the MMC-BESS providing grid support for varying wind power from the offshore wind farm. Assumptions, clarifications and simplifications are given for both test cases. Lastly, test case 3 compares the BESS scheme modeled in this thesis with a BESS scheme connected to the HVDC-link of the HVDC transmission system in terms of grid support. The latter BESS scheme is presented in the master's thesis of Marta N. Hellesnes [38].

A stand-alone model of the MMC-BESS was made in Matlab® Simulink based on the simplified model of the MMC in [70] and [25], and the modeling approach has been presented in the chapter 8. Figure 11.17 shows the stand-alone MMC-BESS model, and Figure 11.18 shows an overview of the MMC-BESS when connected to the offshore wind farm via an HVDC transmission system. A detailed overview of each of the MMC and its subsystems can be found in Appendix B.

The AC-side of the MMC is connected to the PCC between the HVDC transmission system and the AC grid through a three-phase, two-winding transformer. The DC-side of the MMC is connected to a centralized battery which is modeled according to the linear battery model with an SoC measurement, presented in Chapter 9. As aforementioned, the HVDC transmission system was provided as a ready-made model, where only slight changes were made in terms of visualizing results in $dq0$-reference frame and changing the reference signals of the slave converter. Results from three test cases will be reviewed:

- Test case 1: Bidirectional power flow of the MMC-BESS.
- Test case 2: Grid support by the MMC-BESS.
- Test case 3: Comparison between BESS connected to the AC grid and BESS connected to the HVDC-link of the HVDC transmission system for grid support.

All results are further elaborated and discussed in Chapter 12.

11.1 Test case 1: Bidirectional power flow

Test case 1 is to validate a bidirectional power flow to and from the MMC-BESS, where the MMC is responsible for charging and discharging the centralized battery. This is done by the means of step functions which are stepped at certain times during the simulation. The step function-signals are sent through a transfer function-block to imitate the nature of the inertia in the system's response. The battery is defined to be charging for battery power (battery current) between 0 and 1.0 pu, and discharging for battery power (battery current) between 0 and -1.0 pu. SoC-measurement is included as a part of the BMS to monitor the SoC of the centralized battery. This is to further validate the battery charging and discharging processes.

In order to avoid instability of the MMC-BESS when running the simulations, the converter needs to be energized before any changes can be applied. This is done by increasing the MMC d-axis current to a specified value of 0.5 pu, before allowing the AC- and DC-side of the converter to be coupled. The coupling between the AC- and DC-side is done by implementing a built-in switch block, placed inside the Energy and AC current controller-subsystem in Figure 11.17. The switch changes its state from 0 to 1 after 4 seconds of simulation, and enables the connection between the AC- and DC-side of the MMC. If the MMC d-axis current does not reach its specified value before the switch changes position connecting the two sides together, the system quickly becomes unstable and cannot be brought back to a normal operation.

The measurement of the SoC of the battery is enabled by the same switch signal connecting the MMC AC- and DC-side together, cf. Figure 9.4. Therefore no measurement of the battery's SoC is done prior to 4 seconds.

11.1.1 Results

MMC

The results of the MMC is presented in Figure 11.1 to 11.3. Figure 11.1 shows the AC- and DC-side voltages and currents, as well as the zero-sequence energy. The AC-side quantities are represented in $dq0$-transform, and the DC-side quantities are the common DC-link voltage and current. The zero-sequence energy is shown in the latter graph, with its reference signal.

Figure 11.2 shows the AC- and DC-side active power of the MMC in the upper and middle graph. The power balance is shown in the latter graph. As aforementioned, prior to 4 seconds the AC- and DC-side are not coupled together, hence no active power is flowing in the MMC.

Figure 11.3 shows the AC and DC current controllers, as well as the zero-sequence energy. The two leftmost graphs show the AC current controller, with the d- and q-axis currents and their respective references. The upper rightmost graph shows the DC current controller, with the common DC-link current and its reference. The zero-sequence energy and energy reference is shown in the lower leftmost graph.

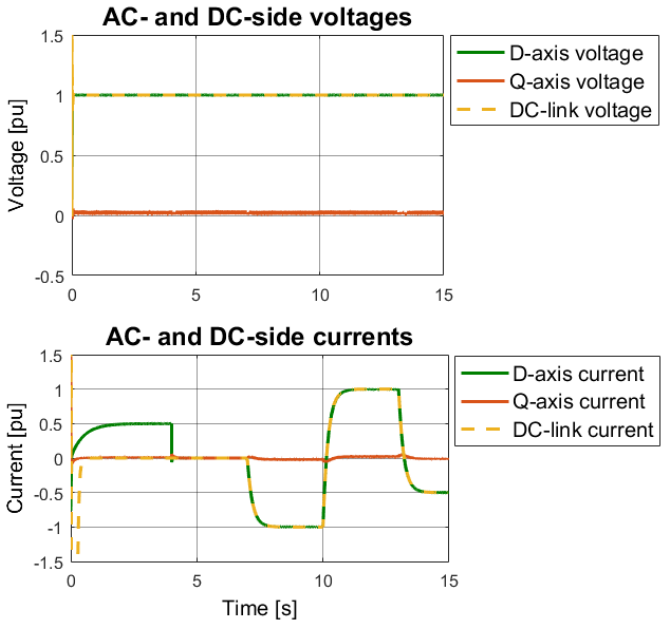

Figure 11.1: AC- and DC-side voltages and currents of the MMC.

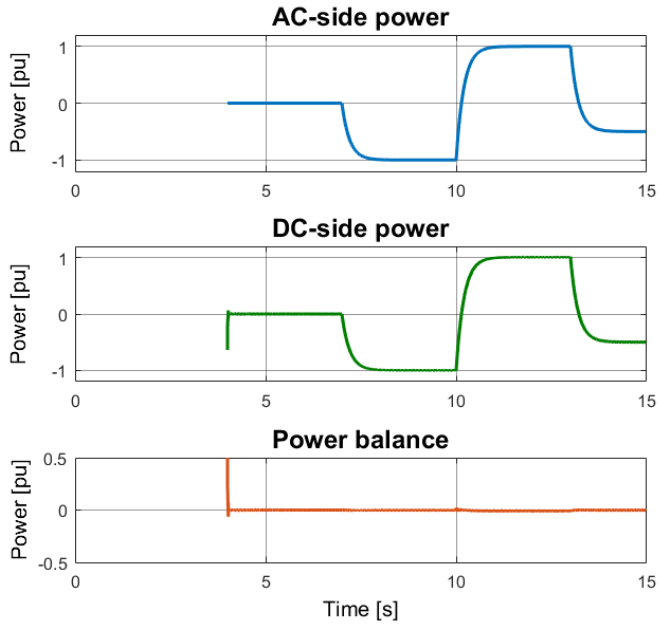

Figure 11.2: AC- and DC-side active power and power balance.

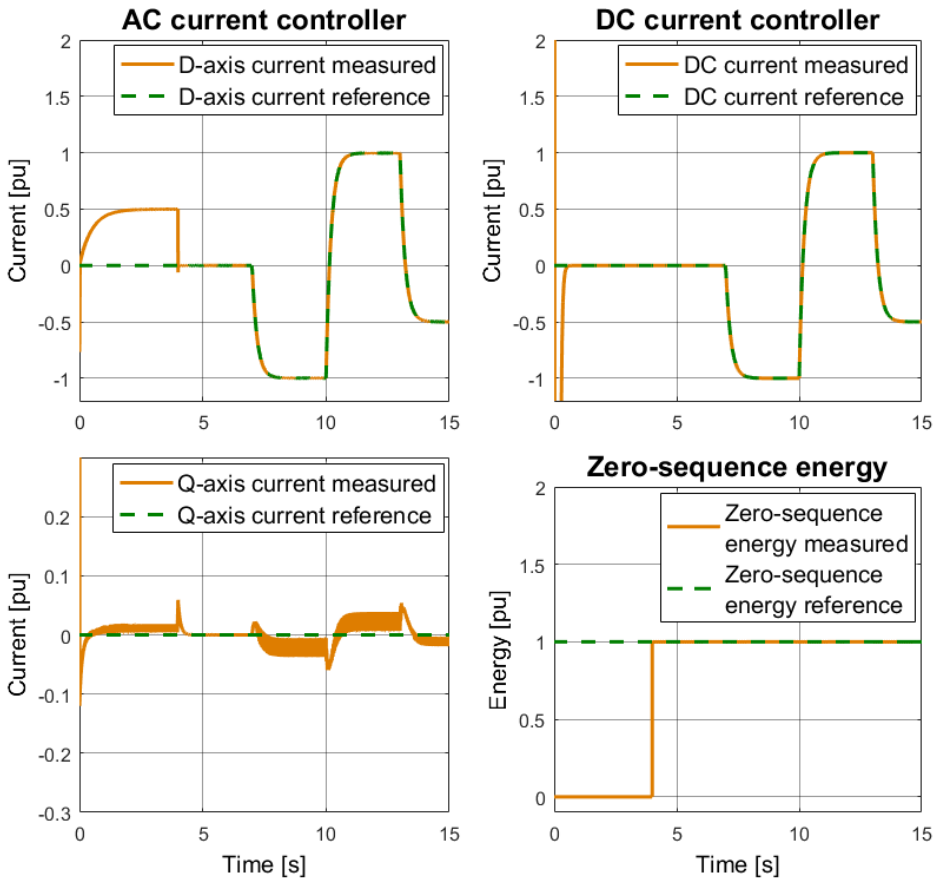

Figure 11.3: AC and DC current controller and zero-sequence energy.

Battery

The results of the centralized battery is shown in Figure 11.4, where the battery voltage, charge and discharge current, and charge and discharge power is shown in the three upper graphs. The latter graph shows the battery SoC. The SoC is measured after 4 seconds when the AC- and DC-side are coupled and active power can flow to and from the battery.

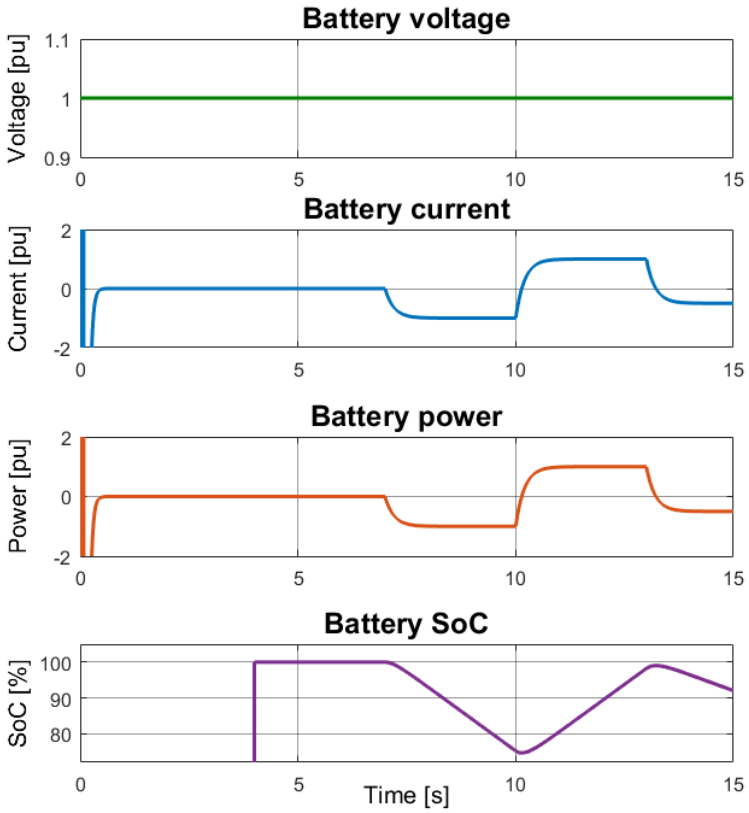

Figure 11.4: Battery voltage, current, power and SoC.

11.2 Test case 2: Grid support

Test case 2 investigates the MMC-BESS ability to provide grid support the AC grid for fluctuating wind power from the offshore wind farm. The MMC-BESS is set to absorb power from the wind farm when the wind power delivered is above its nominal rating. When the wind power delivered is below its nominal rating, the MMC-BESS is set to inject power to the AC grid. The nominal wind power is 1000 MW or 1.0 pu.

The fluctuations in wind power must be carried out by the slave converter of the HVDC transmission system, since the offshore wind farm is only represented as an ideal AC voltage source. The slave can generate a varying wind power profile by changing the reference signal of its d-axis current. The MMC has to apply corresponding steps in order to absorb or inject active power to maintain a constant power flow to the AC grid. This is also done by step functions applied to the DC reference current of the MMC.

Since the MMC-BESS and the HVDC transmission system are based on two different per unit-systems, a gain-block is added to the DC reference current of the MMC to account for the conversion from the MMC-BESS per unit-system to the per unit-system of the HVDC transmission system and the AC grid. This is done by multiplying the ratio between the DC base current of the HVDC transmission system and the DC base current of the MMC-BESS. The turn-ratio is also multiplied with the DC reference signal to account for the line-frequency transformer in the interface between the MMC-BESS and PCC.

Furthermore, the MMC-BESS scheme requires two three-phase breakers, labeled B1 and B2, to ensure sufficient time for energizing the MMC-BESS as well as properly connecting the MMC-BESS to the PCC. Initially, breaker B1 is closed in the time interval between 0 and 5 seconds, allowing the MMC-BESS to be energized and avoid stability issues due to the presence of the HVDC transmission system. During this time interval, the MMC-BESS is connected to an AC voltage source via the line-frequency transformer, cf. Figure 11.18. The nominal line voltage of AC voltage source is 400 kV, same as the AC grid line voltage.

During the same time interval, breaker B2 is initially open. After 5 seconds, B1 and B2 changes states simultaneously by the means of step-functions - B1 opens, whereas B2 closes. This allows the connection of the MMC-BESS to the rest of the system via the PCC. At this instant it is crucial to ensure that both the HVDC transmission system and the MMC-BESS have reached steady state, otherwise stability problems will occur. The initial start-up of the system occurring in the time interval between 0 and 5 seconds is not shown in the results. It is assumed that the full system is in steady state, and the start-up dynamics are a part of the initialization of the simulation and not a part of the investigated case.

11.2.1 Results

MMC

The results of the MMC are presented in Figures 11.5 to Figure 11.7, where all pu values are referred to the per unit system of the HVDC transmission system.

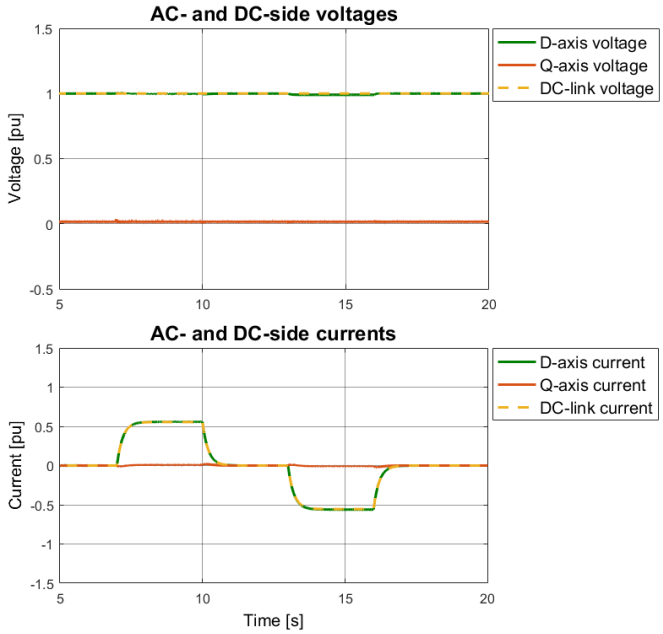

Figure 11.5: The AC- and DC-side voltages and currents of the MMC.

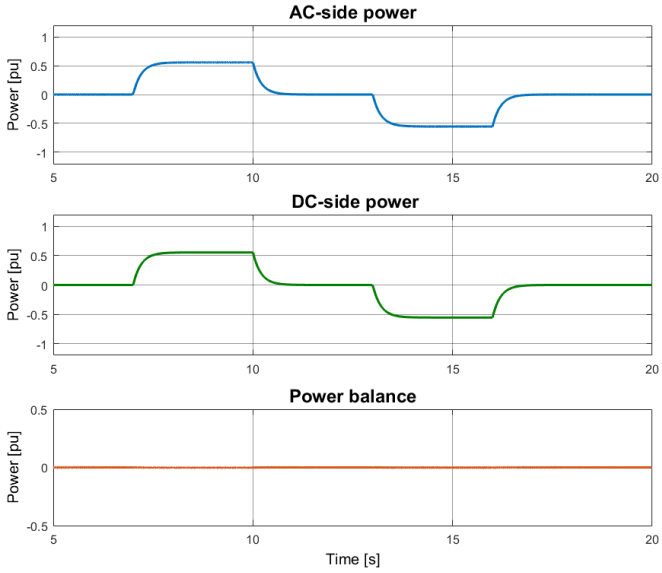

Figure 11.6: The AC- and DC-side active power and power balance.

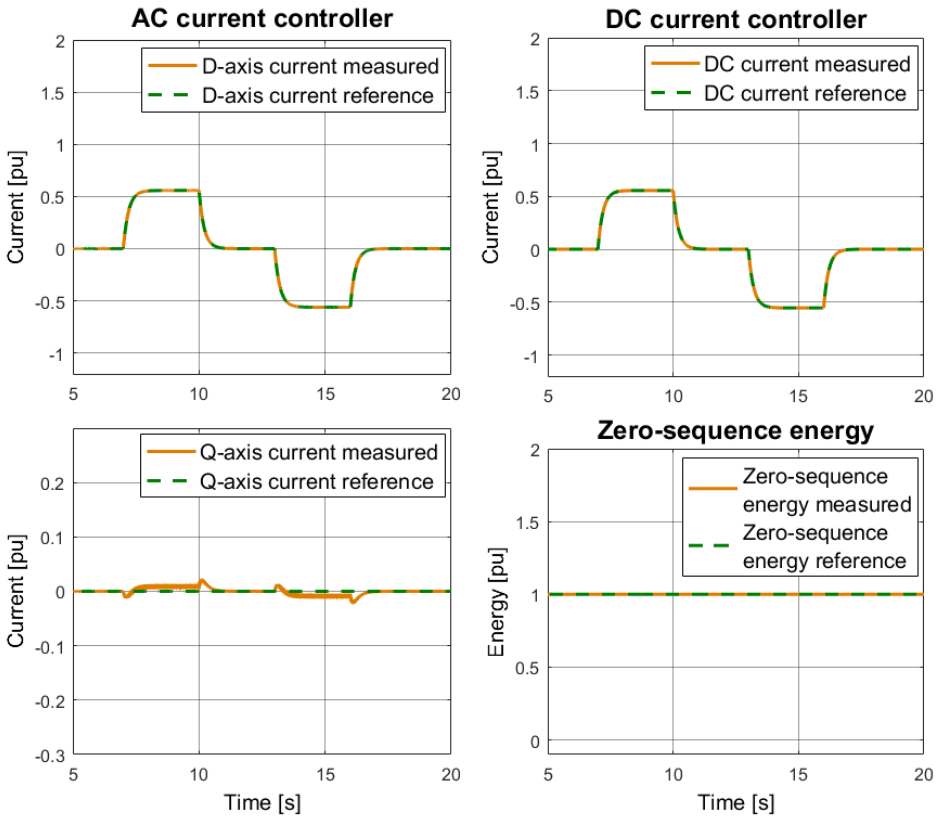

Figure 11.7: The AC and DC current controller and zero-sequence energy.

Battery

Figure 11.8 shows the centralized battery graphs for the battery voltage, charge and discharge current, as well as charge and discharge power.

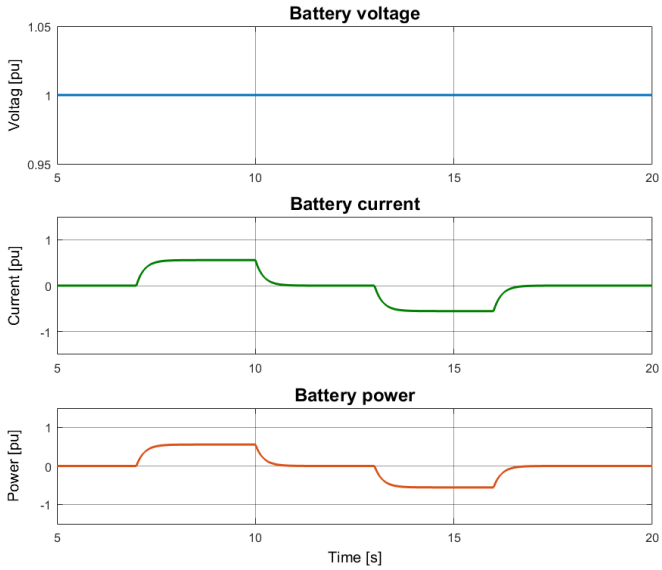

Figure 11.8: The AC and DC current controller and zero-sequence energy.

Line-frequency transformer

The primary and secondary side voltages and currents are shown in Figure 11.9 and 11.10, for abc-reference frame and $dq0$-reference frame, respectively. Figure 11.9 shows the balanced three-phase voltages and currents for an interval of 50 milliseconds. Figure 11.10 shows the d- and q-axis quantities for the full duration of the simulation. The primary side of the transformer is connected to the PCC via B2, and the secondary side is connected to the AC terminals of the MMC, cf. Figure 11.18.

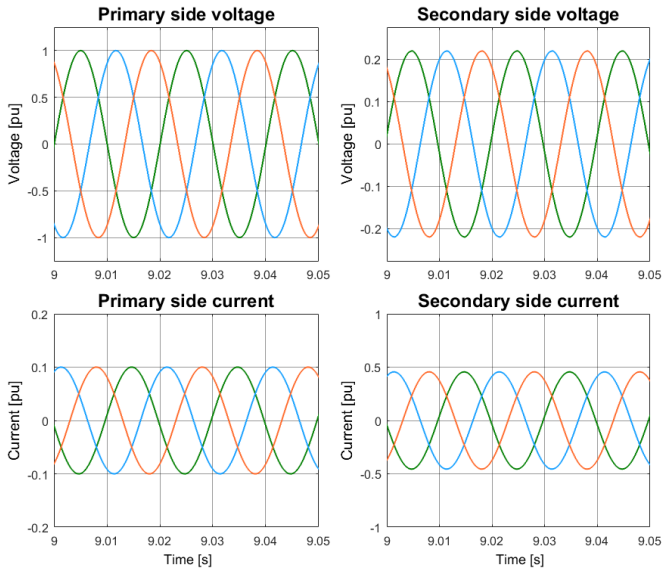

Figure 11.9: Transformer quantities in abc-reference frame.

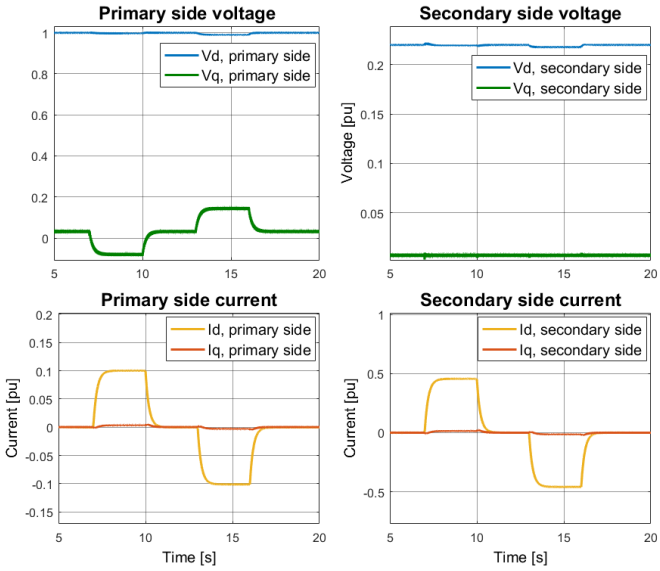

Figure 11.10: Transformer quantities in $dq0$-reference frame.

HVDC transmission system and AC grid

Figure 11.11 shows the master-slave interaction of the HVDC transmission system in terms of active power, DC current and DC voltage. Figure 11.12 shows the active power transfer without grid support, whereas Figure 11.13 shows the active power transfer with grid support being enabled. In Figure the active power delivered from the wind farm corresponds to the base values of the HVDC transmission system, whereas the MMC-BESS base values are used for the MMC-BESS active power. Hence, they cannot be directly summed without converting from one of the pu-systems to comply with the other.

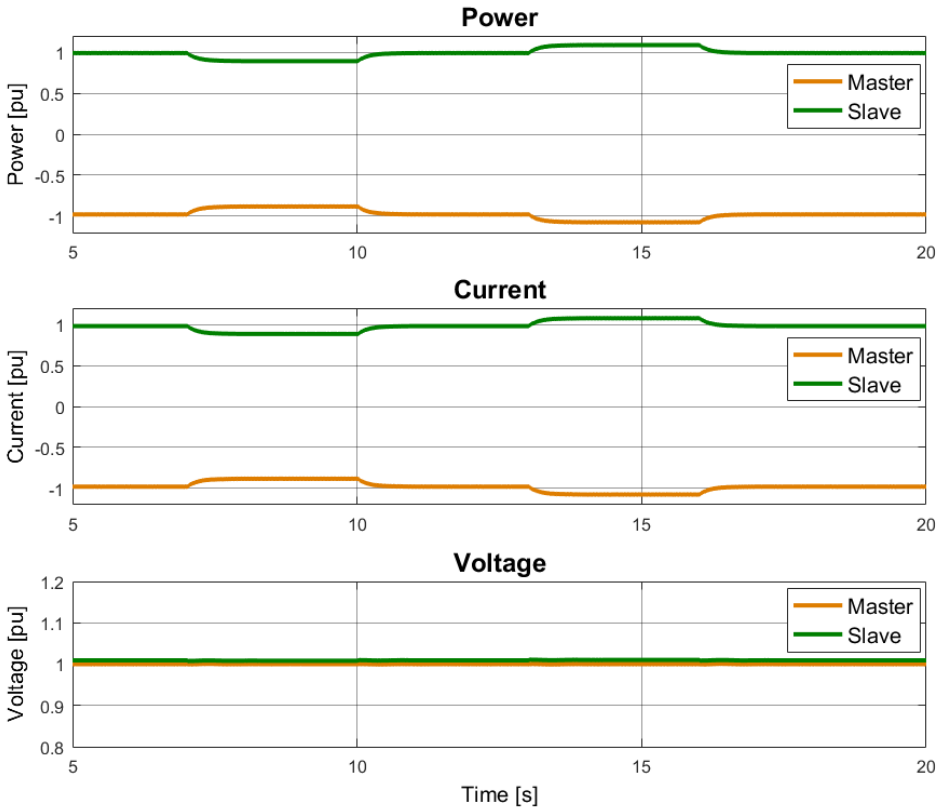

Figure 11.11: Master-slave interaction of the HVDC transmission system.

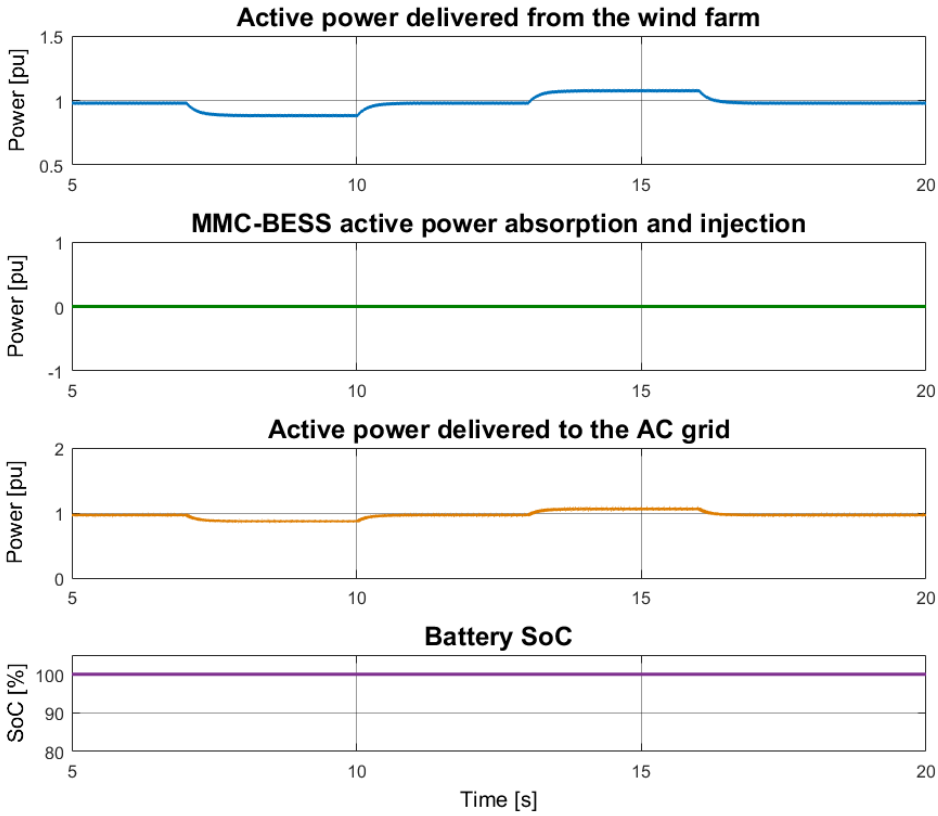

Figure 11.12: Active power transfer of the full system without grid support.

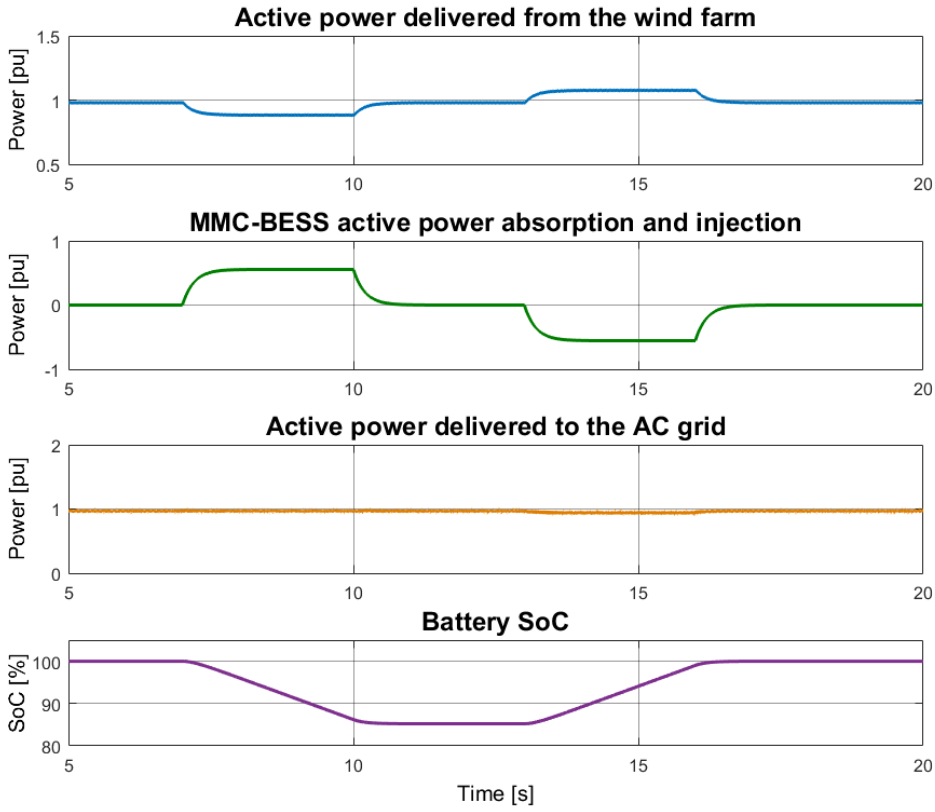

Figure 11.13: Active power transfer of the full system with grid support.

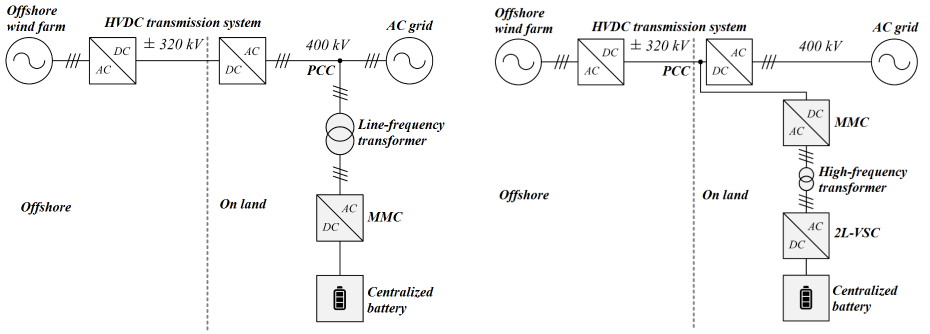

(a) BESS connected to the AC grid.

(b) BESS connected to HVDC system.

Figure 11.14: Single-line diagrams of two BESS schemes.

11.3 Test case 3: Comparison

The last test case shows a comparison between the MMC-BESS presented in this thesis and a BESS scheme connected to the HVDC-link of the HVDC transmission system, where grid support is investigated. A single-line diagram of the two systems to be compared are shown in Figure 11.14a and Figure 11.14b. The latter system has been investigated in [38], and will therefore not be explained in details in terms of modeling and simulation approach in this thesis. Only the results will be presented, followed by a short discussion in Chapter 12.

The system investigated in [38] comprises of an MMC, a high-frequency transformer, a 2L-VSC and a centralized battery. The BESS scheme is connected to the PCC at the HVDC-link of the transmission system, as shown in Figure 11.14b. The MMC for both cases are based on the same modeling principle as presented in [70] and [25].

The two BESS schemes will be tested for the same varying wind power profile, where the nominal wind power is set to 0.82 pu (820 MW). This implies that the BESS schemes must inject active power for wind power below 0.82 pu, and absorb active power for wind power above 0.82 pu. The SoC for the centralized batteries is also included in the results in order to observe the charging and discharging processes.

Both BESS schemes are initially fully charged (100% SoC), and have the same system time response, i.e. the transfer-function blocks used are equal. Furthermore, it is assumed that for positive pu-values the BESS schemes inject active power and for negative pu-values the BESS schemes absorb active power. Prior to 4 seconds of simulation, the two systems are energizing in order to avoid stability issues and are therefore not shown in the graphs for the same reason given in Section 11.2 for test case 2.

11.3.1 Results

Grid support

Figure 11.15 shows the results from the MMC-BESS investigated in this thesis, whereas the results from the BESS scheme investigated in [38] is shown in Figure 11.16.

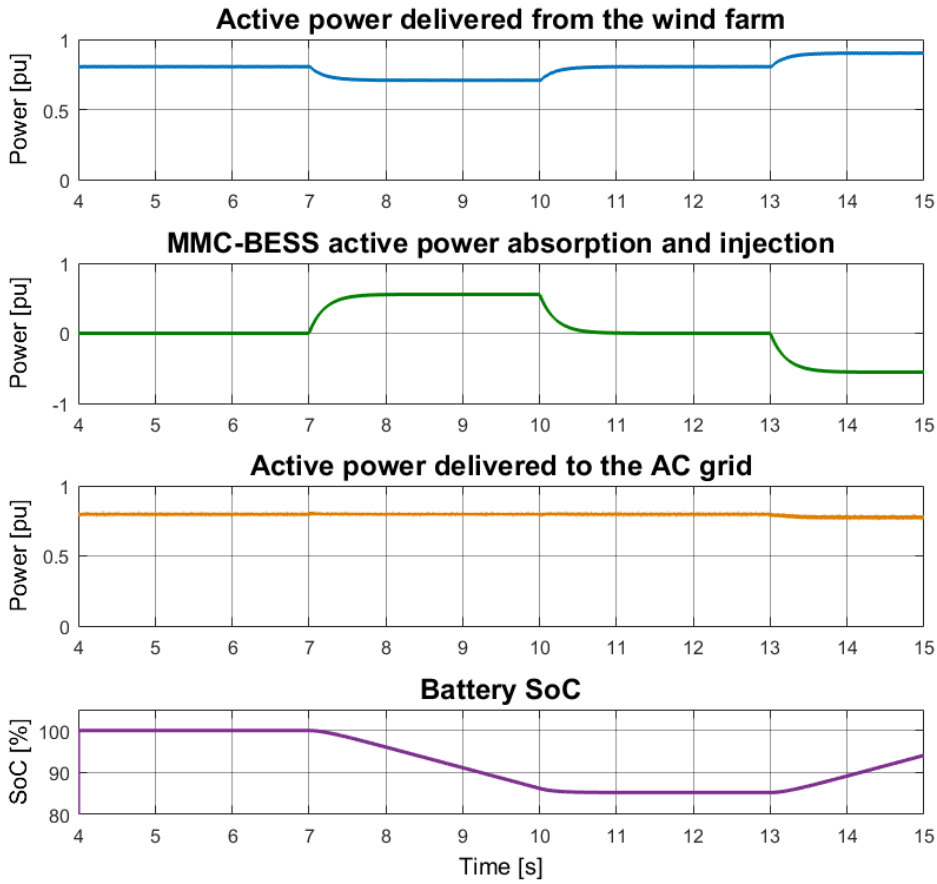

Figure 11.15: Active power transfer for the MMC-BESS investigated in this thesis, cf. Figure 11.14a.

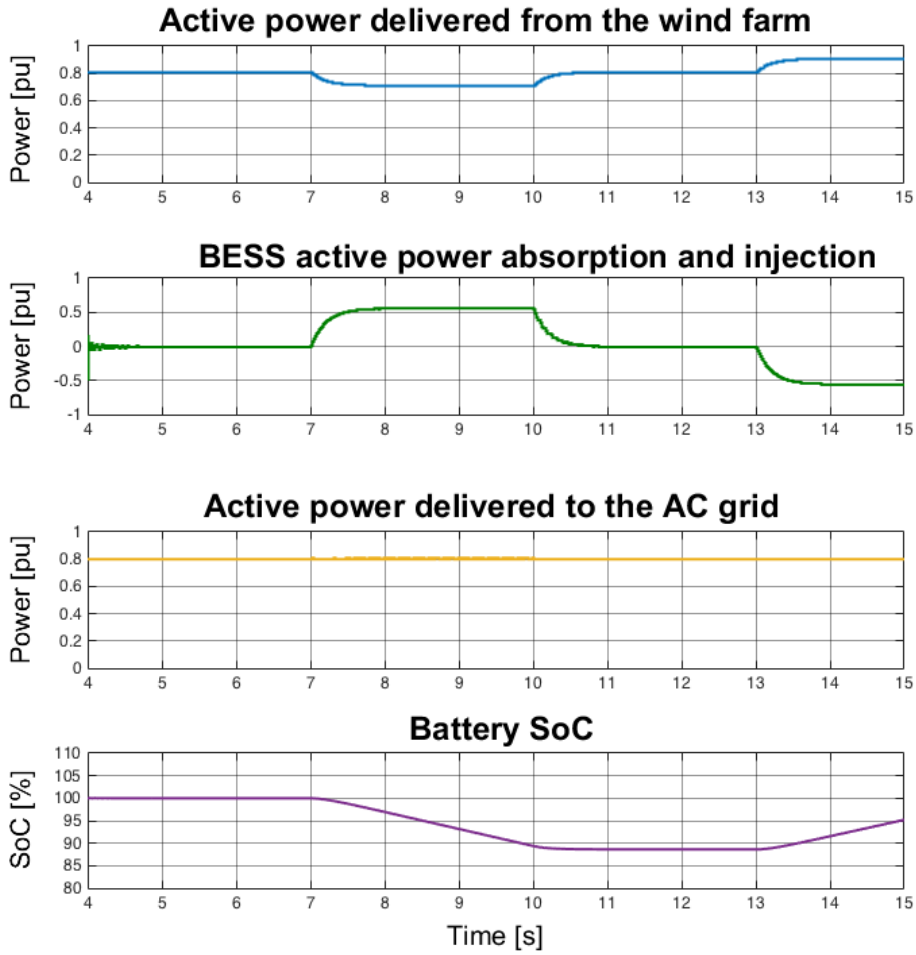

Figure 11.16: Active power transfer for the BESS scheme investigated in [38], cf. Figure 11.14b.

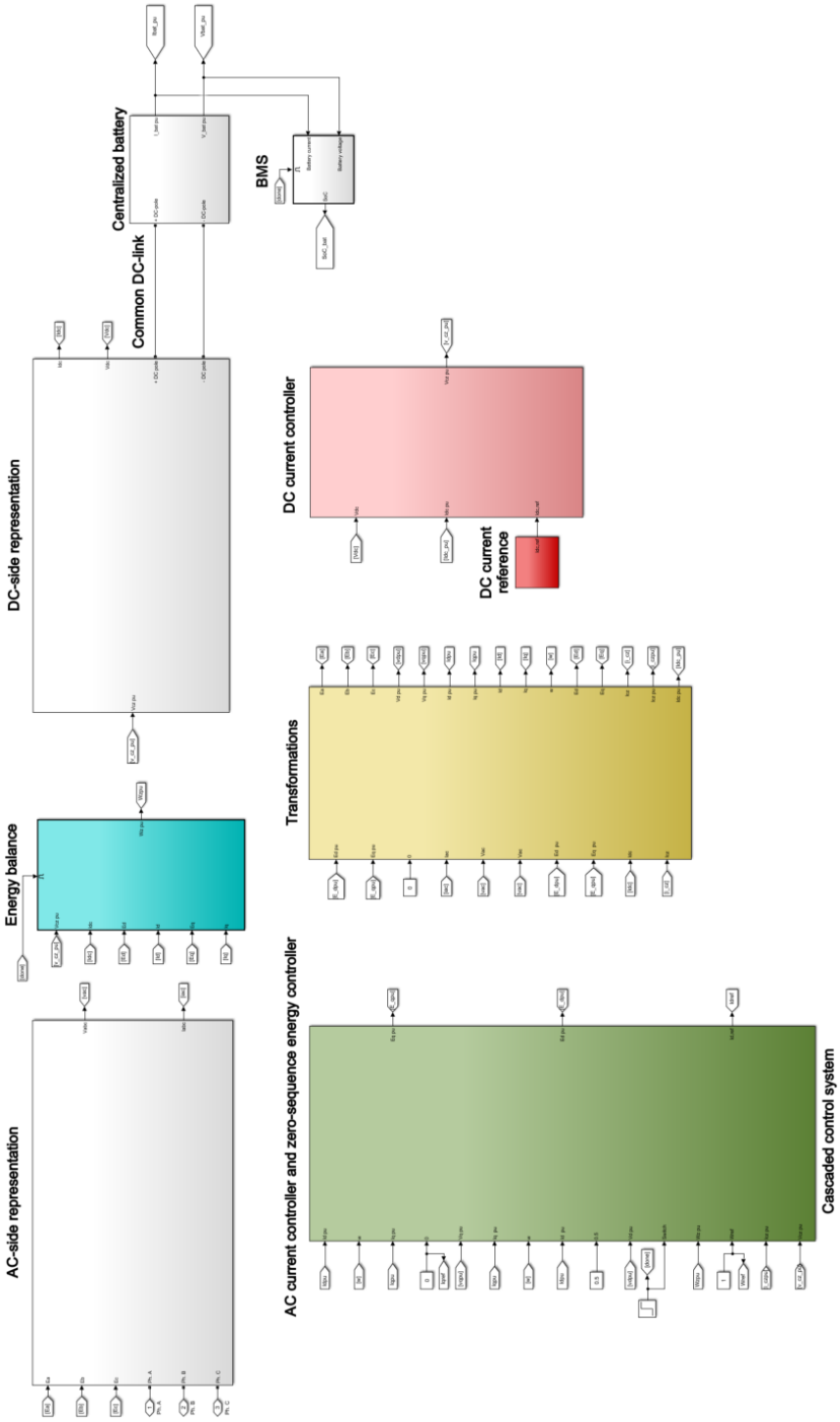

Figure 11.17: Overview of the MMC-BESS model with its associated controllers; MMC with a battery connected to the DC-side.

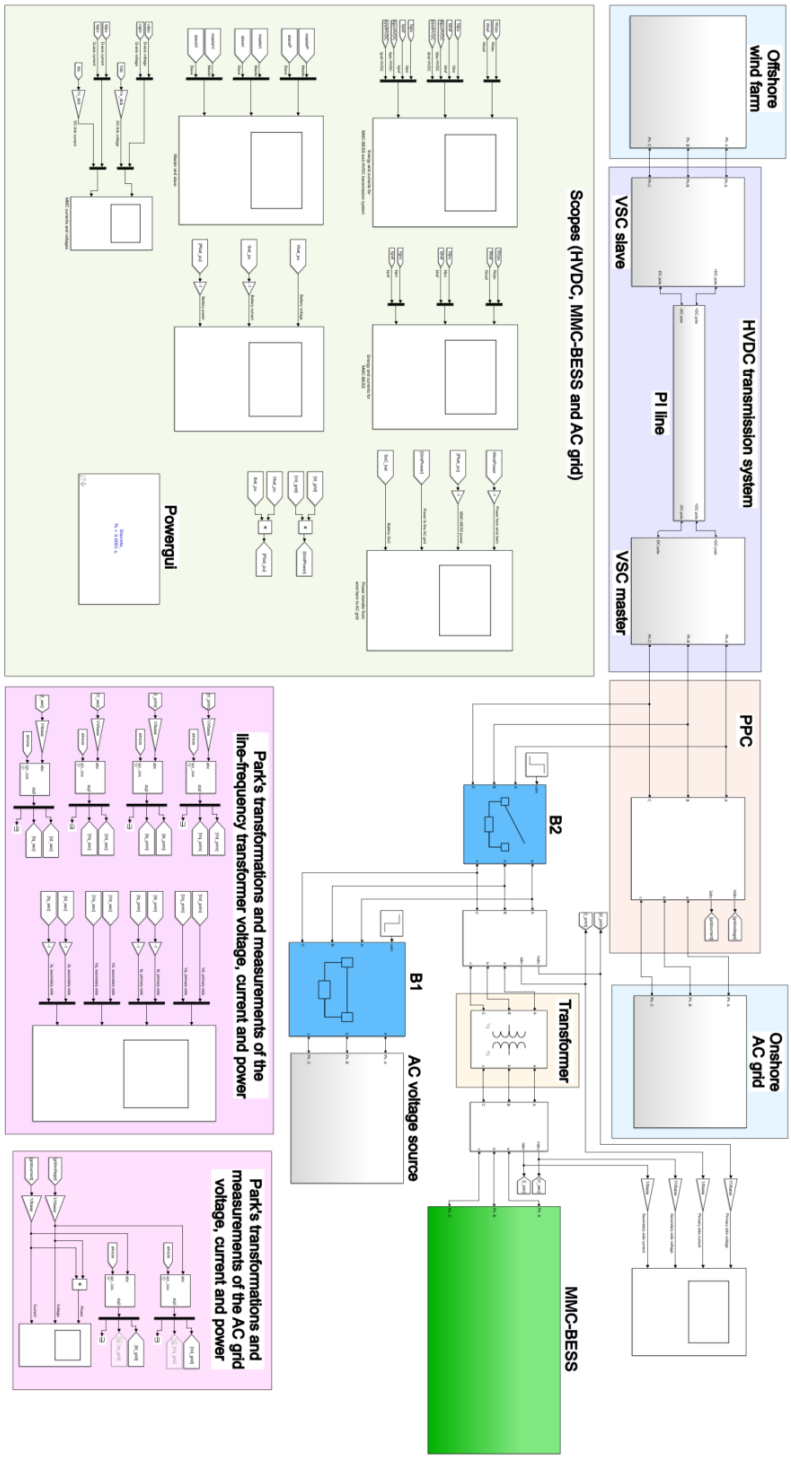

Figure 11.18: Overview of the modeled system.

Part V

Discussion, Conclusion and Further Work

CHAPTER 12

Discussion and Conclusion

The discussions based on the design, and modeling and simulation of the MMC-BESS is presented in this chapter. Parts of the discussions is also provided in Part III and IV, and to get the full aspect and overview of the assumptions and analyses it is therefore highly recommended to read those parts before reading this chapter. Furthermore, this chapter presents the challenges regarding the modeling and simulation of the MMC-BESS. Lastly, a common conclusion is given for the design and the modeling and simulation of the MMC-BESS.

12.1 Design of MMC-BESS

One of the major challenges on designing an MMC-BESS was the high power requirement. The requirement of 10-20% of the wind farm's rated active power of 1000 MW and with a power factor of 0.95, implied that the MMC-BESS needed to be rated close to 200 MVA. As of today, BESS' with such high power ratings do not exist [81], [54], [72]. Both for the design and the simulation of the MMC-BESS, the rated power of 180 MW was chosen.

The three different MMC-BESS schemes (I, II and III), where proposed based on the battery voltage and current ratings of the centralized battery. MMC-BESS I is based on three paralleled battery strings, each string containing 60 1 MW-rated EssPro^{TM} Grid-containers. This requires a total of 180 containers to achieve 180 MW. MMC-BESS II have four paralleled strings, each string with 90 0.5 MW-rated EssPro^{TM} Grid-containers, whereas MMC-BESS III requires 6 paralleled strings of 60 containers of the same power rating. The two latter BESS configurations have a total of 360 containers, implying that the schemes would require considerable more area. Moreover, the cost would also be high for the MMC-BESS configurations II and III, compared to I.

In terms of reliability and to meet the criteria of power coverage of 10-20%, MMC-BESS II offers the highest percent of coverage, $p_{coverage}$, for the maximal allowable num-

ber of disconnected battery strings, N_{max}[1]: it can offer a power coverage of 13.5%, however only one battery string can be disconnected. MMC-BESS III can allow up to two strings to be disconnected, and still be able to cover 12% of the wind farm's rated power. MMC-BESS I can also provide 12% of power coverage, but allows only for one string to be disconnected as for II. Hence, the reliability is apparently higher for MMC-BESS III. However, problems with unequal voltages across the strings increases with the number of strings. It is industry practice is to not install more than three battery strings in parallel [47], implying that MMC-BESS I presents a more optimal choice compared to MMC-BESS III.

Regarding the half-bridge MMC configuration chosen for the MMC-BESS scheme, two different topologies can be realized in terms of number of submodules required and the StakPak rating of the submodule switches. These parameters can strongly indicate the total cost of the MMC, since a major part of the converter cost is closely linked to power semiconductor requirements. MMC-BESS I and III consist of a total of 144 submodules (24 submodules per arm), whereas MMC-BESS II consists of 216 in total (36 submodules per arm). This implies that the MMC configuration for MMC-BESS II is 50% more expensive in terms of power semiconductors than the MMC in I and III. Additionally, the power losses of the MMC would increase with higher number of submodules, which in turn lowers the efficiency. Since the overall efficiency of the BESS (round trip efficiency) is defined as the square of the converter efficiency, the MMC efficiency should be as high as possible implying that both MMC-BESS I and III would serve as optimal choices from a converter standpoint.

The selected power modules for the submodules of the MMC was the ABB IGBT StakPak press-pack module, with available ratings of 4.5 kV and 1.3-2.0 kA. In order to select proper the press-pack module, the converter arm current and the required blocking voltage for each submodule was calculated. For MMC-BESS I and III, the arm currents were 1640 A, whereas for MMC-BESS II the arm current was 1093 A. The required blocking voltage for all three configurations were 3.0 kV. This further indicate that StakPak module rated for 4.5 kV and 2.0 kA must be used for MMC-BESS I and III. Due to lower arm currents, the MMC-BESS II can be implemented by using the StakPak module of 4.5 kV and 1.3 kA. The cost of power modules are generally linked to the current rating of the module: high current rating implies larger cross-section area of the conductor as well as higher insulation requirement, which in turn indicate that the module cost will be higher.

From a cost and power loss perspective, the MMC-BESS I appear to be the optimal choice as MMC-BESS design. The configuration utilizes lower numbers of batteries (1.0 MW-rated EssPro^{TM} Grid-containers), comply with industry practice of only three paralleled strings, as well as being able to cover 12% with one disconnected string. Furthermore, the MMC requires only 144 submodules in total.

As Chapter 7 suggested, a battery configuration based on distributed batteries would utilize the modular characteristic of the MMC, in addition to offering better performance, higher redundancy and lower cost. The line frequency transformer at the AC terminals of the MMC could be replaced with DC-DC converters connected across each submodule. The presented DC-DC converters in Chapter 7 were the buck-boost converter and the DAB converter, where the DAB converter is preferred due to the galvanic isolation provided by

[1] See Chapter 5, Table 5.3 for N_{max} and $p_{coverage}$.

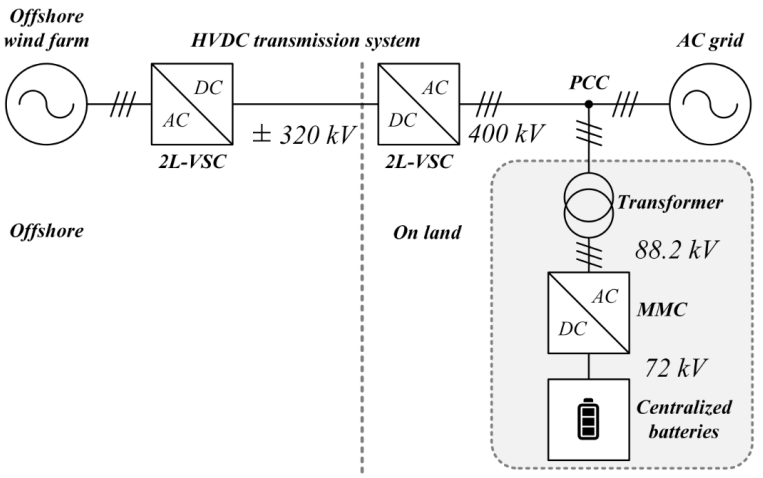

Figure 12.1: MMC with centralized batteries connected on the common DC-link.

the high-frequency transformer within the converter. This approach offers a higher degree of safety since each submodule is electrically isolated from the battery module, rather than a big, bulky and lossy transformer connected to the MMC AC terminals. The high-frequency transformer offers several advantages, first of which being the size. Operating at high frequencies, commonly in the range of 20 kHz to 1 MHz, the transformer size will be small, regardless the power rating. Moreover, due to the small size of the high-frequency transformer, fewer turns are required. This reduces the losses, making the transformer more efficient [5].

A further suggestion regarding the MMC-BESS configuration, was the proposed three-port MMC with integrated batteries, each connected to a DC-DC converter as energy storage submodules. The overall system comprised of an HVDC transmission system connecting the offshore wind farm to the onshore AC grid, where the HVDC system converter stations are based on 2L-VSCs. By further improving both the MMC-BESS by reducing cost and area requirements, as well as improving the HVDC transmission system performance, the 2L-VSC can be replaced with MMC in the converter stations. Moreover, one (or both) of the HVDC converter stations can be implemented as an MMC-BESS with energy storage submodules, where the DAB converter is preferred.

A summary on the technical requirements of the proposed MMC-BESS scheme in this section, based on the analysis, calculations and various considerations carried out in Chapter 5, 6 and 7, is presented in Table 12.1. Figure 12.1 shows the initial structure of the MMC-BESS scheme with a line-frequency transformer connecting the MMC-BESS to PCC, whereas Figure 12.2 presents the improved structure of the MMC-BESS where the transformer is replaced with DC-DC converters connected to the submodules, and lastly, Figure 12.3 depicts the three-port solution, where the MMC-BESS replaces one of the converter stations of the HVDC transmission system.

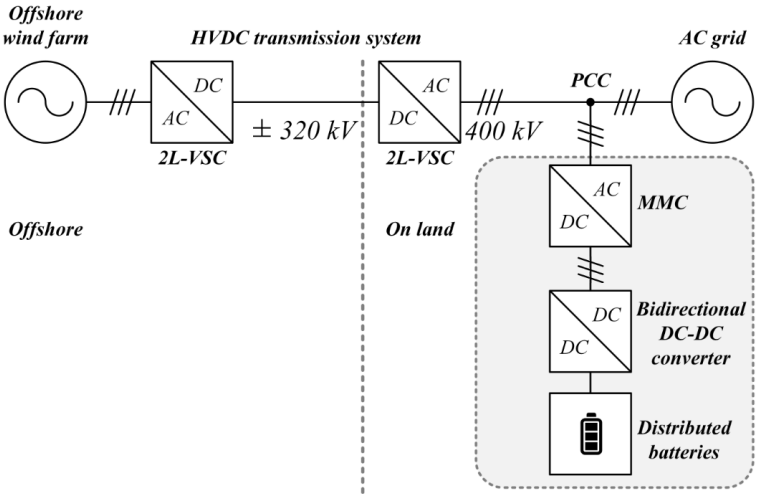

Figure 12.2: MMC with distributed batteries and DC-DC converters connected across each submodule.

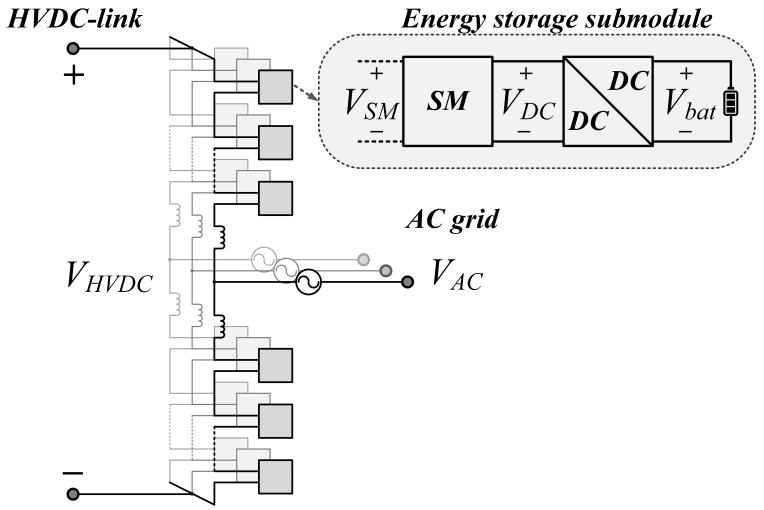

Figure 12.3: Three-port MMC with distributed batteries with the common DC-link of the MMC connected to the HVDC-link, realized as a converter station for the HVDC transmission system.

Table 12.1: Technical specifications of the 180 MW, 45 MWh MMC-BESS scheme.

BESS scheme	
BESS system active power rating	180 MW
Power coverage of the system	18%
No. of battery modules in total	180
No. of battery modules per string	60
No. of paralleled strings	3
Battery voltage	72 kV
Battery current	2.5 kA
Active power per string	60 MW
Allowable no. disconnected strings	1
Coverage with disconnected strings	12%
Battery	
Battery module type	EssPro^{TM} Grid
Battery module ratings	1.0 MW, 1.2 kV
Manufacturer	ABB
Battery technology	Lithium-ion
Power conversion system	
Converter technology	MMC
Converter active power rating	180 MW
Submodule configuration	Half-bridge
Converter arm current	1.64 kA
Submodule blocking voltage	3.0 kV
No. of submodules in total	144
No. of submodules per arm	24
No. of converter arms	6
Power semiconductor	
Power module technology	IGBT press-pack
Power module	StakPak
Manufacturer	ABB
Part number	5SNA 200K450300
IGBT-to-diode ratio	1.1
Maximum voltage	4.5 kV
Nominal current	2.0 kA

12.2 Modeling and simulation of MMC-BESS

12.2.1 Test case 1

The initial step in the simulations was to validate the ability of the MMC to function as a PCS. Thus, the main function of the modeled MMC is to enable a bidirectional power flow to and from the centralized battery, through rectification (AC-DC) and inversion (DC-AC). More specifically, the MMC enables the charging and discharging of the battery. The second main function of the MMC as a PCS is to control the power to ensure a stable flow to avoid unnecessary wearing and stress of the battery.

The MMC AC- and DC-side voltages in Figure 11.1 show a steady and balanced operation of the MMC. The AC-side phase voltages are converted from abc- to $dq0$-reference frame, and are therefore presented by their d- and q-axis components. The d-axis component of the AC phase voltage is aligned with the common DC-link voltage where both are 1.0 pu, however they are divided by their respective base values which implies that their real numeral values will differ. The relationship between the AC-side phase voltage and the DC-side voltage is given in Equation (8.17).

The AC- and DC-side currents shown in the latter graph of Figure 11.1, show the d-axis current energizing the system the first 4 seconds of simulation. At the instant where the AC- and DC-side are coupled, the d-axis current coincide with the DC current. With a steady d-axis and DC-link voltage of 1.0 pu, together with the varying d-axis and DC current result in active power flowing in both sides of the MMC. The d-axis components and the DC voltage and current are responsible for the active power flow in the MMC. The q-axis components are responsible for the reactive power, and by forcing both the q-axis voltage and current to be zero no reactive power should flow in the MMC.

Figure 11.2 presents the active power balance between the MMC AC- and DC-side. Prior to 4 seconds, no active power is measured in the converter due to the decoupling of the AC- and DC-side. After 4 seconds the AC-side active power equals the DC-side active power, thus the power balance is maintained.

The current controller operations are shown in Figure 11.3, where the d-axis current controller and DC current controller are able to regulate their respective currents to follow their references. The graphs show well-tuned PI controllers for both currents. The q-axis current show transient spikes where the d-axis current changes direction and magnitude. Spikes appear due to cross-coupling terms, as well as for rapid changes in the current. These appear as disturbances to the controller output, and are therefore subtracted by a decoupling term to improve the controller performance. This can be seen in Figure 8.5, where $-v_q + \omega L i_d$ is subtracted from the q-axis current controller output of $G_c(s)$. Nonetheless, the transient spikes present in the q-axis current are larger when the MMC is performing at its outer limits of operation, i.e. between 1.0 and -1.0 pu, where the spikes are less than 5% or 0.5 pu in magnitude. The q-axis current controller is able to perform adequate control of the current.

The zero-sequence energy is following its reference after 4 seconds of simulation, implying that the zero-sequence energy controller is able to control the zero-sequence energy to follow a 1.0 pu-reference well.

The measurements of the centralized battery is presented in Figure 11.4. The battery voltage equals common DC-link voltage, and is maintained constant and equal to 1.0 pu

throughout the simulation. The battery current is zero until 7 seconds, implying that no active power is flowing to or from the battery. This is further validated with the two latter graphs, where the batter power is zero and the SoC is constant and equal to 100%. After 7 seconds, the MMC discharges the battery by increasing the d-axis current to -1.0 pu in Figure 11.3, which corresponds to the change in DC current and thus the battery current and power in Figure 11.4. The SoC decreases from initially 100% to 73%. At 10 seconds, the MMC charges the battery by reversing the d-axis current direction, increasing it toward 1.0 pu. The SoC increases towards 100%, before decreasing after 13 seconds when the MMC discharges the battery with a d-axis current of -0.5 pu.

12.2.2 Test case 2

Test case 1 was to ensure proper operation of the MMC-BESS, which is a prerequisite for test case 2 where grid support is investigated. The MMC is operating well as for test case 1, maintaining its power balance and with well-tuned controllers, cf. Figure 11.5 to 11.7. Thus, the MMC is performing its tasks as a PCS for the BESS. The q-axis current spikes present in Figure 11.7 are less apparent (less than 3%) than in test case 1, due to less rapid changes in the current. Figure 11.8 shows the centralized battery measurement, where the battery current charges and discharges the battery as in test case 1.

Before the MMC-BESS is connected to the AC grid at PCC, the MMC AC line voltage must be stepped up to the line voltage level of the AC grid. This is done by the line-frequency transformer, where the primary side is connected to the AC grid and the secondary side is connected to the AC terminals of the MMC. The transformer is modeled as a simplified transformer, with an equivalent impedance of $Z_T = 0.005 + j0.15$ pu referred to the transformer's primary side. The excitation branch of the transformer is ignored by selecting very high values for the core-loss resistance and the magnetizing inductance. Hence, a very small load current flows in the branch and omitting the branch can be done without compromising the transformers behavior under loaded conditions. This is shown in Figure 11.9, with balanced three-phase voltages and currents.

Furthermore, to ensure the voltage is stepped up to the AC grid line voltage, the voltage ratio of the primary and secondary sides can be compared with the turn-ratio of the transformer. The voltage ratio should equal the turn-ratio specified in the model, based on the calculations in Part III for the MMC-BESS design. This comparison can be done by analyzing the results in Figure 11.10, where the primary and secondary side voltages and currents are represented in the $dq0$-reference frame. The d-axis voltage of the primary side is approximately 1.0 pu throughout the simulation, whereas the d-axis voltage of the secondary side is close to 0.22 pu. Thus, the voltage-ratio becomes:

$$\frac{V_{prim}}{V_{sec}} = \frac{V_{d,prim}}{V_{d,sec}} = \frac{1.0}{0.22} = 4.55 \tag{12.1}$$

The turn-ratio calculated in Part III was 4.54:1, and with a deviation of only 0.22% from the voltage ratio, the line-frequency transformer is operating as specified.

Figure 11.11 shows the master-slave interaction of the HVDC transmission system. The operation of the HVDC system is elaborated in Chapter 10, and as shown in the simulation results the active power is flowing from the slave to the master, i.e. from the

offshore wind farm to the onshore AC grid. The DC voltage is equal and constant to 1.0 pu, where as the DC current is varying according to the varying wind power profile. As a result, the active power in the HVDC system is varying.

Since the HVDC transmission system was provided for the test case, the controllers of the VSC stations are assumed to operate adequately. The analysis does not cover the internal controller dynamics, and are therefore not included in the results.

Figure 11.12 shows the active power fluctuations from the wind farm propagating through the HVDC transmission system in the upper graph. The MMC is set to not interact with the power variations, resulting in varying active power being delivered to the AC grid as shown in the two middle graphs. The SoC of the centralized battery is 100% throughout the simulation, implying no power is discharged to the grid.

Figure 11.13 presents the active power from delivered from the wind farm, the MMC-BESS interaction and the resulting power delivered to the AC grid. The SoC of the centralized battery is included, to validate the charging and discharging processes. The wind power is fluctuating around a set point of 1.0 pu, being the nominal active power of the wind farm. The variations are balanced by the MMC-BESS, where the MMC charges the battery for positive pu-values and discharges for negative pu-values. This counteraction results in a smooth, steady active power flow to the AC grid.

The SoC further validates the battery charging processes, where the battery is initially fully charged with SoC of 100%. At 7 seconds, the active power delivered from the wind farm falls below 1.0 pu to 0.9 pu, at which the MMC discharges the battery with a steady discharge rate. At 10 seconds, the wind farm is able to deliver power at its nominal rating, and the MMC is set to neither charge or discharge the battery maintaining an SoC of 85%. At 13 seconds the power delivered from the wind farm increases to 1.1 pu. The MMC charges the battery accordingly, increasing the SoC to 100%.

12.2.3 Test case 3

The last test case compares the two BESS schemes presented in Figure 11.14 in terms of grid support. Figure 11.15 shows the power transfer of the MMC-BESS investigated in the theses, whereas Figure 11.16 shows the power transfer of the BESS scheme investigated in [38].

The test results for the two schemes are essentially the same. Figure 11.16 show the presence of some minor disturbances of the BESS active power in the upper middle graph after 4 seconds of simulation. These are most likely due to the coupling of the AC- and DC-side of the MMC, where the common DC-link is connected directly to the HVDC-link of the HVDC transmission system. More specific, the disturbance is not a part of the investigated case since it present due to the modeling approach of the MMC where energizing must be done in advance. Nonetheless, the disturbance is sufficiently damped and is not affecting the investigated case further.

Additionally, slight disturbances are present in the BESS active power between the transitions. These disturbances could be the result of the BESS scheme comprising of additional components compared to the MMC-BESS presented in this thesis, cf. Figure 11.14. The results of the MMC-BESS in Figure 11.15 shows smoother graphs for the MMC-BESS active power between transitions. The difference between the two BESS

schemes is essentially the high-frequency transformer and the 2L-VSC, and the disturbances in the BESS scheme results in [38] could occur due to these components.

The SoC for the centralized battery in the two schemes shows the charging and discharging processes. Both batteries are initially fully charged, decreasing their SoC to for wind power below 0.82 pu. The SoC in Figure 11.15 decreases to 85%, whereas the SoC in Figure 11.16 decreases to approximately 88%. The deviation could be due to different slight changes in the battery ratings, i.e. the rated energy capacity and the discharge rate of the battery.

12.2.4 Modeling and simulation challenges

The challenges of modeling the MMC-BESS were the implementation of the controllers and calculating suitable gains, which turned out to take considerably amount of time of troubleshooting and remodeling. Instability issues arose on different stages of the modeling, and were dealt with accordingly. One unexpected outcome was the base value of the capacitance, Cb, had to be in units of seconds, rather than Farads (Appendix D, line 106-107). For Cb in Farads, the system would quickly become unstable for negative pu-values.

Regarding the test case investigating the MMC-BESS' ability to provide grid support, a model employing logical if-else blocks was made in an attempt to make a simplified controller sensing the variations in the wind power. However, this quasi controller did not work properly and due to limited time, the MMC was modeled with step-function blocks providing presumed reference signals according to the wind power variations.

12.3 Conclusion

The MMC-BESS has been presented as a promising technology enabling RES integration and realization of smart grids for future power systems. It offers a variety of attractive properties such as modularity and scalability, low THD, excellent efficiency and reliability. The main parts investigated in this thesis revolves around the design of an MMC-BESS, and the modeling and simulation of an MMC-BESS for grid support.

The design of the MMC-BESS was initially based on an conventional MMC with half-bridge submodules, where a centralized battery-approach was chosen for simplicity. The design utilizes commercially available technologies to make a more realistic solution. Furthermore, by replacing the centralized batteries with energy storage submodules the MMC-BESS design would better employ the modular structure of the MMC, and thus an increased reliability of the scheme can be achieved.

The last step in the design-part investigated the possible solution of replacing one or more of the 2L-VSCs in the HVDC transmission system's converter station with the MMC-BESS. This three-port solution, where the MMC-BESS with energy storage submodules is connected to the HVDC-link on the DC-side and the AC-grid on the AC-side, indicates both a reduction of area and cost as well as improving the HVDC transmission system's performance. However, more attempt should be made to verify the advantages of the proposed solution.

The modeling and simulation of the MMC-BESS investigates the MMC-BESS scheme initially proposed in the design-part. The results from the simulations confirmed the

MMC-BESS ability to support the AC grid during variable wind power. The MMC performed satisfactory charging and discharging of the batteries, with well-tuned energy and current controllers. Moreover, the SoC measurement was included to further verified the centralized battery's charging and discharging processes, making the results more reliable.

CHAPTER 13

Future Work

This chapter briefly presents some proposed topics for future work, reflecting the MMC-BESS design and modeling and simulation parts investigated in this thesis.

Synthetic Inertia

The inertia of the power system is proportional to the sum of stored energy in the rotating masses of the generators and motors directly connected to the grid [37]. RES typically have little or no inertia, and increased levels of RES is being integrated into the grid combined with less and less grid-connected rotating masses have raised concerns regarding the system inertia as well as the amount of fast frequency control reserves [94], [29]. By investigating how inertial response in grid-scale BESS' can be emulated, the proposed MMC-BESS scheme could be further improved to prevent the frequency and rate-of-change of frequency (RoCoF) from exceeding their limits. As for the model of the MMC-BESS this can be realized by the means of an inertial controller. The inertial controller proposed in [37] is able to reduce the initial system frequency drop, without affecting the steady-state frequency.

Asymmetric grid conditions

The MMC-BESS is very likely to operated under asymmetric grid conditions. The MMC-BESS model presented in this thesis is not assembled for faults and asymmetric conditions. Well-established line-current control techniques for the MMC exists: balanced positive-sequence current (BPSC) injection, active power oscillation elimination (APOE), and the reactive power oscillation elimination (RPOE) [86].

Fault handling capability

The MMC-BESS model assembled and presented in this thesis is not equipped to handle large disturbances such as faults. This could be achieved by implementing circuit breakers and disconnectors into the model. Other safety measurements should be investigated.

Modeling and simulation of a three-port MMC-BESS for HVDC transmission system

The assumptions regarding the three-port MMC-BESS integrated in the converter station of the HVDC transmission system should be validated through modeling and simulation to verify the feasibility of the solution. The challenge lies in the modeling approach being able to reflect the system's dynamics adequately without posing great computational burden.

References

[1] ABB Ltd., 2015. EssPro^{TM} Grid Battery Energy Storage Systems – The Power to Control Energy. ABB Ltd.

[2] ABB Ltd., March 2016. Power Semiconductor – Product Broschure 2016.

[3] ABB Ltd., May 2017. Semiconductors.
URL `http://new.abb.com/semiconductors`

[4] Adapa, R., Nov 2012. High-Wire Act: HVdc Technology: The State of the Art. IEEE Power and Energy Magazine 10 (6), 18–29.

[5] Agile Magnetics, June 2017. An Essential Part of Supplying Power to Modern Electronics.

[6] Allebrod, S., Hamerski, R., Marquardt, R., 2008. New Transformerless, Scalable Modular Multilevel Converters for HVDC-Transmission. In: Power Electronics Specialists Conference, 2008. PESC 2008. IEEE. IEEE, pp. 174–179.

[7] Alvarez, R., Wahle, M., Gambach, H., Dorn, J., Sept 2016. Optimum Semiconductor Voltage Level for MMC Submodules in HVDC Applications. In: 2016 18th European Conference on Power Electronics and Applications (EPE'16 ECCE Europe). pp. 1–9.

[8] Arrillaga, J., Liu, Y. H., Watson, N. R., Murray, N. J., 2010. Self-Commutating Converters for High Power Applications. John Wiley & Sons.

[9] Badran, A., 2017. Water, Energy & Food Sustainability in the Middle East: The Sustainability Triangle. Springer.

[10] Bahrman, M. P., Johnson, B. K., March 2007. The ABCs of HVDC transmission technologies. IEEE Power and Energy Magazine 5 (2), 32–44.

[11] Bajracharya, C., Molinas, M., Suul, J. A., Undeland, T. M., et al., 2008. Understanding of tuning techniques of converter controllers for VSC-HVDC. In: Nordic Workshop on Power and Industrial Electronics (NORPIE/2008), June 9-11, 2008, Espoo, Finland. Helsinki University of Technology.

[12] Balchen, J. G., Andresen, T., Foss, B. A., 2003. Reguleringsteknikk - Department of Engineering Cybernetics. Norwegian University of Science and Technology, Trondheim, Norway.

[13] Baliga, B. J., 2015. The IGBT Device: Physics, Design and Applications of the Insulated Gate Bipolar Transistor. Elsevier Science.

[14] Beardsall, J. C., Gould, C. A., Al-Tai, M., Sept 2015. Energy Storage Systems: A Review of the Technology and its Application in Power Systems. In: 2015 50th International Universities Power Engineering Conference (UPEC). pp. 1–6.

[15] Beddard, A., Barnes, M., 2015. Modelling of MMC-HVDC Systems – An Overview. Energy Procedia 80, 201–212.

[16] Beerten, J., Diaz, G. B., D'Arco, S., Suul, J. A., April 2016. Comparison of Small-Signal Dynamics in MMC and Two-Level VSC HVDC Transmission Schemes. In: 2016 IEEE International Energy Conference (ENERGYCON). pp. 1–6.

[17] Bresesti, P., Kling, W. L., Hendriks, R. L., Vailati, R., 2007. HVDC Connection of Offshore Wind Farms to the Transmission System. IEEE Transactions on Energy Conversion 22 (1), 37–43.

[18] Buschendorf, M., Weber, J., Bernet, S., March 2012. Comparison of IGCT and IGBT for the use in the Modular Multilevel Converter for HVDC Applications. In: International Multi-Conference on Systems, Sygnals Devices. pp. 1–6.

[19] Chae, S. H., Lee, S., Kim, H.-C., Kim, E.-H., 2016. Analyzing Modulation Techniques for the Modular Multilevel Converter. International Journal of Computer and Electrical Engineering 8 (4), 259.

[20] Chan, H. L., 2000. A New Battery Model for use with Battery Energy Storage Systems and Electric Vehicles Power Systems. In: 2000 IEEE Power Engineering Society Winter Meeting. Conference Proceedings (Cat. No.00CH37077). Vol. 1. pp. 470–475 vol.1.

[21] Chen, Q., Li, R., et al., 2016. Analysis and Fault Control of Hybrid Modular Multilevel Converter with Integrated Battery Energy Storage System (HMMC-BESS). IEEE Journal of Emerging and Selected Topics in Power Electronics.

[22] Daniel, J. P., Liu, S., Ibanez, E., Pennock, K., Reed, G., Hanes, S., 2014. National Offshore Wind Energy Grid Interconnection Study Executive Summary. Tech. rep., ABB, Inc., Cary, NC (United States).

[23] De Doncker, R. W., 2016. Power Electronics - Control, Synthesis, Application, lecture notes.

[24] De-Leon, S., 2010. High-Power Rechargeable Lithium Battery Market.

[25] Diaz, G. B., Suul, J. A., D'Arco, S., Sept 2015. Small-Signal State-Space Modeling of Modular Multilevel Converters for System Stability Analysis. In: 2015 IEEE Energy Conversion Congress and Exposition (ECCE). pp. 5822–5829.

[26] Divya, K., stergaard, J. O., 2009. Battery Energy Storage Technology for Power Systems – An Overview. Electric Power Systems Research 79 (4), 511 – 520.

[27] Dubey, G., 1986. Thyristorised Power Controllers. Wiley Eastern.

[28] Electronics Hub, jun 2015. Three-Phase Transformer.

[29] Endegnanew, A. G., Uhlen, K., 2016. Global Analysis of Frequency Stability and Inertia in AC Systems Interconnected through an HVDC. In: Energy Conference (ENERGYCON), 2016 IEEE International. IEEE, pp. 1–6.

[30] Eriksson, K., 2002. HVDC Light and Development of Voltage Source Converters. ABB review.

[31] et al., J. D. W., 2014. Guide for the Development of Models for HVDC Converters in a HVDC Grid. CIGRÉ technical brochure 604.

[32] Filsecker, F., Alvarez, R., Bernet, S., Feb 2013. Comparison of 4.5-kV Press-Pack IGBTs and IGCTs for Medium-Voltage Converters. IEEE Transactions on Industrial Electronics 60 (2), 440–449.

[33] Friedemann, A., June 2017. Peak Energy & Resources, Climate Change, and the Preservation of Knowledge.

[34] Fuji Electric Co., May 2017. Power semiconductors.
URL `http://www.fujielectric.com/products/semiconductor/model/igbt/`

[35] Gao, S., Barnes, M., March 2012. Phase-Locked Loop for AC Systems: Analyses and Comparisons. In: 6th IET International Conference on Power Electronics, Machines and Drives (PEMD 2012). pp. 1–6.

[36] Glover, J., Sarma, M., Overbye, T., 2012. Power System Analysis & Design, SI Version. Cengage Learning.

[37] Gonzalez-Longatt, F. M., Alhejaj, S. M., 2016. Enabling Inertial Response in Utility-Scale Battery Energy Storage System. In: Innovative Smart Grid Technologies-Asia (ISGT-Asia), 2016 IEEE. IEEE, pp. 605–610.

[38] Hellesnes, M. N., June 2017. Use of Battery Energy Storage for Power Balancing in a Large-Scale HVDC Connected Wind Power Plant. Master's thesis, Norwegian University of Science and Technology.

[39] Hertem, D. v., Gomis-Bellmunt, O., Liang, J., 2016. HVDC Grids For Offshore and Supergrid of the Future. IEEE Press series on power engineering.

[40] Hitachi Power Semiconductor Device, Ltd., May 2017. IGBT.
URL http://www.hitachi-power-semiconductor-device.co.jp/en/product/igbt/

[41] Infineon Technologies AG, May 2017. IGBT modules.
URL http://www.infineon.com/cms/en/product/power/igbt/igbt-module/channel.html?channel=ff80808112ab681d0112ab69e66f0362

[42] IXYS UK Westcode Ltd., May 2017. Press-pack IGBT capsules.
URL http://www.westcode.com/igbt1.html

[43] Jansen, A. N., Kahaian, A. J., Kepler, K. D., Nelson, P. A., Amine, K., Dees, D. W., Vissers, D. R., Thackeray, M. M., 1999. Development of a high-power lithium-ion battery. Journal of Power Sources 8182, 902 – 905.

[44] Jones, P. S., Davidson, C. C., Sept 2013. Calculation of Power Losses for MMC-based VSC HVDC Stations. In: 2013 15th European Conference on Power Electronics and Applications (EPE). pp. 1–10.

[45] Joseph, A., Shahidehpour, M., 2006. Battery Storage Systems in Electric Power Systems. In: Power Engineering Society General Meeting, 2006. IEEE. IEEE, pp. 8–pp.

[46] Kawabata, J., Kusunoki, Y., Onozawa, Y., Nishimura, Y., Kobayashi, Y., Ikawa, O., June 2015. The Advanced 7th Generation IGBT Module for High Power Density Technology. In: 2015 9th International Conference on Power Electronics and ECCE Asia (ICPE-ECCE Asia). pp. 554–559.

[47] Keyhani, A., 2016. Design of Smart Power Grid Renewable Energy Systems. John Wiley & Sons.

[48] Konstantinou, G., Zhang, J., Ceballos, S., Pou, J., Agelidis, V. G., June 2015. Comparison and Evaluation of Sub-Module Configurations in Modular Multilevel Converters. In: 2015 IEEE 11th International Conference on Power Electronics and Drive Systems. pp. 958–963.

[49] Küchler, A., 2017. High Voltage Engineering: Fundamentals – Technology – Applications. Springer.

[50] Kumar, V., Pandey, A. S., Sinha, S. K., 2016. Grid Integration and Power Quality Issues of Wind and Solar Energy System: A Review. In: Emerging Trends in Electrical Electronics & Sustainable Energy Systems (ICETEESES), International Conference on. IEEE, pp. 71–80.

[51] Ladoux, P., Serbia, N., Carroll, E. I., Sept 2015. On the Potential of IGCTs in HVDC. IEEE Journal of Emerging and Selected Topics in Power Electronics 3 (3), 780–793.

[52] Lesnicar, A., Marquardt, R., 2003. An Innovative Modular Multilevel Converter Topology suitable for a Wide Power Range. In: Power Tech Conference Proceedings, 2003 IEEE Bologna. Vol. 3. IEEE, pp. 6–pp.

[53] Li, T., Gole, A. M., Zhao, C., Aug 2016. Harmonic Instability in MMC-HVDC Converters resulting from Internal Dynamics. IEEE Transactions on Power Delivery 31 (4), 1738–1747.

[54] Li, X., Hui, D., Lai, X., April 2013. Battery Energy Storage Station (BESS)-Based Smoothing Control of Photovoltaic (PV) and Wind Power Generation Fluctuations. IEEE Transactions on Sustainable Energy 4 (2), 464–473.

[55] Long, H. Y., Sweet, M. R., Narayanan, E. M. S., Li, G., March 2017. Reliability Study and Modelling of IGBT Press-Pack Power Modules. In: 2017 IEEE Applied Power Electronics Conference and Exposition (APEC). pp. 2711–2717.

[56] Machowski, J., Bialek, J., Bumby, J., 2011. Power System Dynamics: Stability and Control. Wiley.

[57] Madsen, K., Krogsgaard, P., 2010. Offshore Wind Power 2010. BTM Consult 22.

[58] May, T. W., Yeap, Y. M., Ukil, A., Nov 2016. Comparative Evaluation of Power Loss in HVAC and HVDC Transmission Systems. In: 2016 IEEE Region 10 Conference (TENCON). pp. 637–641.

[59] Mehr, T. H., Masoum, M. A. S., Jabalameli, N., Sept 2013. Grid-Connected Lithium-Ion Battery Energy Storage System for Load Leveling and Peak Shaving. In: 2013 Australasian Universities Power Engineering Conference (AUPEC). pp. 1–6.

[60] Mitsubishi Electric Co., May 2017. Semiconductors & devices.
URL http://www.mitsubishielectric.com/semiconductors/products/powermod/igbtmod/

[61] Moranchel, M., Huerta, F., Sanz, I., Bueno, E., Rodríguez, F. J., 2016. A Comparison of Modulation Techniques for Modular Multilevel Converters. Energies 9 (12), 1091.

[62] Murnane, M., Ghazel, A., 2017. A Closer Look at State of Charge (SOC) and State of Health (SOH) Estimation Techniques for Batteries.

[63] Nahar, A., 2008. Control System Design for Power Converters. Microchip Webseminars.

[64] Nikoletatos, J., Tselepis, S., 2015. Renewable Energy Integration in Power Grids – Technology Brief. IEA-ETSAP and IRENA technology Brief.

[65] Norrga, S., Ängquist, L., Sharifabadi, K., Li, X., 2015. Power Electronics for HVDC Grids–an Overview. In: CIGRE colloquium.

[66] Phuangpornpitak, N., Tia, S., 2013. Opportunities and Challenges of Integrating Renewable Energy in Smart Grid System. Energy Procedia 34, 282 – 290.

[67] Rashid, M. H., 2010. Power Electronics Handbook: Devices, Circuits and applications. Academic press.

[68] Reite, I. P., December 2016. Battery Energy Storage System Connected to a 50 Hz-grid, specialization project.

[69] Saad, H., Peralta, J., Dennetiére, S., Mahseredjian, J., Jatskevich, J., Martinez, J. A., Davoudi, A., Saeedifard, M., Sood, V., Wang, X., Cano, J., Mehrizi-Sani, A., July 2013. Dynamic Averaged and Simplified Models for MMC-Based HVDC Transmission Systems. IEEE Transactions on Power Delivery 28 (3), 1723–1730.

[70] Sanchez, S., Bergna, G., Tedeschi, E., April 2017. Tuning of Control Loops for Grid-Connected Modular Multilevel Converters under a Simplified Port Presentation for Large System Studies. ResearchGate.

[71] Schettler, F., Huang, H., Christl, N., 2000. HVDC Transmission Systems using Voltage Sourced Converters – Design and Applications. In: Power Engineering Society Summer Meeting, 2000. IEEE. Vol. 2. IEEE, pp. 715–720.

[72] SDG&E, ???? SDG&E Unvails World's Largest Lithium Ion Battery Storage Facility.

[73] Sharifabadi, K., Harnefors, L., Nee, H.-P., Teodorescu, R., Norrga, S., 2016. Design, Control and Application of Modular Multilevel Converters for HVDC Transmission Systems. John Wiley & Sons.

[74] Smith, S. C., Sen, P. K., Kroposki, B., Malmedal, K., May 2010. Renewable Energy and Energy Storage Systems in Rural Electrical Power Systems: Issues, Challenges and Application Guidelines. In: 2010 IEEE Rural Electric Power Conference (REPC). pp. B4–B4–7.

[75] Soong, T., 2015. Modular Multilevel Converters with Integrated Energy Storage. Ph.D. thesis, University of Toronto.

[76] Soong, T., Lehn, P. W., Oct 2014. Evaluation of Emerging Modular Multilevel Converters for BESS Applications. IEEE Transactions on Power Delivery 29 (5), 2086–2094.

[77] Spahic, E., Schettler, F., Varma, D., Dorn, J., 2015. Impact of the DC Technology on Transmission Grids.

[78] Steimer, P. K., June 2010. Enabled by High Power Electronics – Energy Efficiency, Renewables and Smart Grids. In: The 2010 International Power Electronics Conference - ECCE ASIA -. pp. 11–15.

[79] Suul, J. A., Molinas, M., Norum, L., Undeland, T. M., Dec 2008. Tuning of Control Loops for Grid Connected Voltage Source Converters. In: 2008 IEEE 2nd International Power and Energy Conference. pp. 797–802.

[80] Team, M. E. V., 2008. A Guide to Understanding Battery Specifications.

[81] Technofi, 7 2016. Technical Analysis of Past and On-going Projects - Support to R&D Strategy in the Area of SET Plan Activities in Smart Grids and Energy Storage, 167–168Quality check: ENTSO-E, EDSO, EASE, RSE, VITO.

[82] Tedeschi, E., 2016. Lecture notes in ELK-23: Power Electronics for Future Power Systems.

[83] The Modern Grid Strategy team, 2009. Energy Storage – A Key Enabler of the Smart Grid.

[84] Thien, I., Axelsen, H., Merten, M., Zurhühlen, S., Münderlein, J., Leuthold, M., Sauer, D. U., 2015. Planning of Grid-Scale Battery Energy Storage Systems: Lessons Learned from a 5 MW Hybrid Battery Storage Groject in Germany. In: Proc. BATTCON Int. Battery Conf. pp. 18–1.

[85] Torres-Olguin, R. E., rdal, A. R. A., ylen, H. S., Endegnanew, A. G., kelsøy, K. L., Tande, J. O., 2014. Experimental Verification of a Voltage Droop Control for Grid Integration of Offshore Wind Farms using Multi-Terminal HVDC. Energy Procedia 53, 104 – 113.

[86] Vasiladiotis, M., Cherix, N., Rufer, A., 2015. Impact of Grid Asymmetries on the Operation and Capacitive Energy Storage Design of Modular Multilevel Converters. IEEE Transactions on Industrial Electronics 62 (11), 6697–6707.

[87] Wahlstroem, J., Dujic, D., Luescher, M. A., Reist, S., May 2014. High Power IGCT based Multilevel Inverter. In: PCIM Europe 2014; International Exhibition and Conference for Power Electronics, Intelligent Motion, Renewable Energy and Energy Management. pp. 1–6.

[88] Wang, G., Konstantinou, G., Townsend, C. D., Pou, J., Vazquez, S., Demetriades, G. D., Agelidis, V. G., Oct 2016. A Review of Power Electronics for Grid Connection of Utility-Scale Battery Energy Storage Systems. IEEE Transactions on Sustainable Energy 7 (4), 1778–1790.

[89] Westerweller, T., Friedrich, K., Armonies, U., Orini, A., Parquet, D., Wehn, S., 2010. Trans Bay cable - World's First HVDC System using Multilevel Voltage-Sourced Converter. Proc. 2010 CIGRE, Paris.

[90] Wu, B., Pontt, J., Rodríguez, J., Bernet, S., Kouro, S., 2008. Current-source converter and cycloconverter topologies for industrial medium-voltage drives. IEEE Transactions on Industrial Electronics 55 (7), 2786–2797.

[91] Yang, X., Li, J., Wang, X., Fan, W., Zheng, T. Q., 2011. Circulating Current Model of Modular Multilevel Converter. In: Power and Energy Engineering Conference (APPEEC), 2011 Asia-Pacific. IEEE, pp. 1–6.

[92] Yao, L., Yang, B., Cui, H., Zhuang, J., Ye, J., Xue, J., 10 2016. Challenges and Progresses of Energy Storage Technology and its Application in Power Systems. Journal of Modern Power Systems and Clean Energy 4 (4), 519–528, copyright - The Author(s) 2016; Last updated - 2016-10-28.

[93] Zeng, R., Xu, L., Yao, L., July 2014. An Improved Modular Multilevel Converter with DC Fault Blocking Capability. In: 2014 IEEE PES General Meeting — Conference Exposition. pp. 1–5.

[94] Zhu, J., Booth, C. D., Adam, G. P., Roscoe, A. J., Bright, C. G., 2013. Inertia Emulation Control Strategy for VSC-HVDC Transmission Systems. IEEE Transactions on Power Systems 28 (2), 1277–1287.

Appendix

APPENDIX A

MMC-BESS system design: Matlab script

The various parameters for the MMC-BESS design is calculated by the Matlab script below. The user is asked to specify a battery voltage, from which the calculations are based on. Other predetermined parameters are given in Table A.1. After the user has specified a battery voltage a list of calculated parameters is printed in the *Command Window* of Matlab®, this is omitted from the code below.

Table A.1: Predetermined parameters for the Matlab script.

Parameter	Symbol	Value
Grid line voltage	V_line	400 kV
Battery power	P_bat	180 MW
Power factor	pf	0.95
No. of converter arms	N_arm	6
Max. output DC voltage of one EssPro™ Grid-container	V_EssPro	1.2 kV
Max. output active power of one EssPro™ Grid-container	P_EssPro	1 MW

MMC_BESS_design.m

```
%% MMC-BESS system design

clc;

prompt = 'Battery voltage in kV? ';
V_bat = input(prompt)*1e3; % Battery voltage in kV

%% Battery data
% The battery power should be 10-20% of the active power from the offshore
% wind farm:

%P_bat = 200e6; % 200 MW
P_bat = 180e6; % 180 MW
%P_bat = 100e6; % 100 MW
pf = 0.95;
S_bat = P_bat/pf;

t_bat = 0.25; % 15 min = 0.25 hours
capacity_bat = P_bat*t_bat; % [Wh]

V_line = 400e3;
V_ac_line = sqrt(3/2)*V_bat; % using V_ac,LL (RMS) = sqrt(3/2)*V_dc
V_ph = V_ac_line/sqrt(3); % RMS ph. voltage (decided by the battery
    voltage)

%% Semiconductor data
% IGBTs are made as modules with an anti-parallel diode, however IGCTs
% are only found as a single power switch and a anti-parallel diode must
% be additionally considered. Other manufacturers can be considered as
    well
% (Semikron, Westcode, Mitsubishi, Fuji, Hitachi, etc):

% Various IGBT modules:
% ABB's StakPak (PressPak) IGBT module, with IGBT-to-diode ratio = 1.1
% 5SNA 1300K450300
V_IGBT = 4.5e3; % V_CE [kV]
I_IGBT = 1.3e3; % I_C [kA]
% 5SNA 2000K450300
% V_IGBT = 4.5e3; % V_CE [kV]
% I_IGBT = 2e3; % I_C [kA]
%
% % ABB's HiPak IGBT module, with single IGBT
% % 5SNA 1200G450300 (or Infineon's FZ1200R45HL3 - same ratings)
% V_IGBT = 4.5e3; % V_CE [kV]
% I_IGBT = 1.2e3; % I_C [kA]
% % 5SNA 0750G650300
% V_IGBT = 6.5e3; % V_CE [kV]
% I_IGBT = 0.75e3; % I_C [kA]
%
% Infineon's IGBT module
% FZ1500R33HE3
% V_IGBT = 3.3e3; % V_CE [kV]
% I_IGBT = 1.5e3; % I_C [kA]

% % ABB's IGCT (no module with anti-parallel diodes are manufactured):
```

```
%% V_IGCT = 4.5e3; % V_DRM [kV]
%% I_IGCT = 4e3; % I_T(AV)M [kA]

% Choosing IGBT module or IGCT:
V_SW = V_IGBT;
I_SW = I_IGBT;
% V_SW = V_IGCT;
% I_SW = I_IGCT;

%% MMC-BESS design
% Assuming one parallel connection per phase leg (no parallel connections
% of semiconductors within the submodules). The current that the IGBTs/
% IGCTs must be able to handle. Basing the calculation on the upper arm
% current:

I_bat = P_bat/V_bat; % Battery current
I_dc = I_bat;
I_ph = S_bat/(3*V_ph); % RMS phase current
I_margin = 0.15*I_ph; % A margin which accounts for the circ. current
I_arm = (I_dc/3) + (I_ph/2) + I_margin; % The full arm current
I_submodule = I_arm; % The current in the arm is the current the
    submodules
                     % must handle if no parallel connections of
                     % semiconductors are made within the submodules

N_sm = ceil(V_bat/((2/3)*V_IGBT)); % No. of submodules per arm
N_arm = 6; % No. of arms (2 arms per phase leg, 3 phase legs in total)
N_tot = N_sm*N_arm; % Total no. of submodules in the MMC

V_submodule = V_bat/N_sm; % The voltage each submodule must handle

%% Transformer's turn-ratio 'n'
% Calculating the turn-ratio of the T/F based on the line voltage ratio
% between the AC grid and the AC side of the MMC (should be a low turn-
% ratio to get a more realistic result - less than 5):

if V_line > V_ac_line
    n = V_line/V_ac_line;
else
    n = V_ac_line/V_line;
end

%% No. of EssProTM Grid BESS' required
% Assuming both series and parallel connection of EssProTM Grid-containers
% to increase the voltage on the battery side, while keeping the current
% low through the batteries; assuming this is an feasible approach for
% this thesis. Further, one container is assumed to have a max. DC voltage
% of 1.2 kV, and a max. power of 30 MW. The max. DC voltage used in this
% script is 1.2 kV and the max. power of one container is set to 1 MW. The
% real battery power is calculated by no. of series and parallel
% connections, as well as the power output of the EssProTM Grid-container:

V_EssPro = 1.2e3; % 1.2 kV
P_EssPro = 0.5e6; % 0.5 MW
%P_EssPro = 1e6; % 1 MW

Nseries = ceil(V_bat/V_EssPro); % No. of containers in series
```

```
110
111 Pstring = P_EssPro*Nseries;
112 Istring = Pstring/V_bat;
113 Nparallel = ceil(I_dc/Istring); % No. of parallel-connections
114
115 Ntotbat=Nseries*Nparallel; % The real total no. of containers
116
117 P_bat_real = P_EssPro*Ntotbat; % The real total battery power
```

APPENDIX B

MMC-BESS model: Simulink model

A overview of the MMC-BESS subsystems is given below. These include:

- Figure B.1: AC-side representation modeled in SI system
- Figure B.2: DC-side representation modeled in SI system
- Figure B.3: Centralized battery modeled in SI system
- Figure B.4: Battery management system (SoC measurement) modeled in per unit system
- Figure B.5: Energy balance modeled in SI system
- Figure B.6: Zero-sequence energy controller and AC current controller modeled in per unit system
- Figure B.7: DC current controller modeled in per unit system
- Figure B.8: Phase-locked loop, Park's transformations and transformations between SI and per unit system

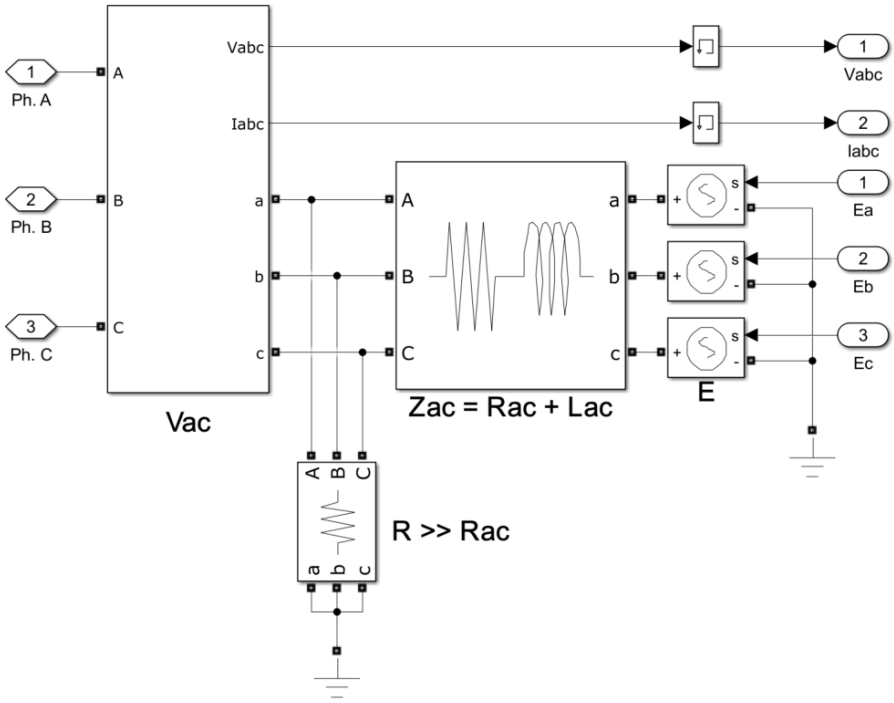

Figure B.1: MMC-BESS: AC-side representation.

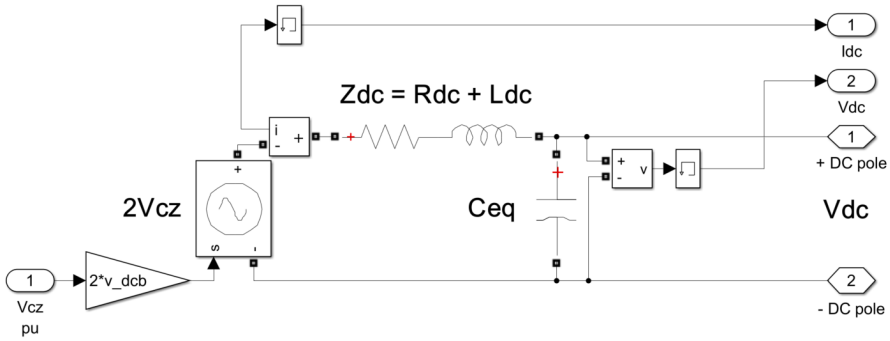

Figure B.2: MMC-BESS: DC-side representation.

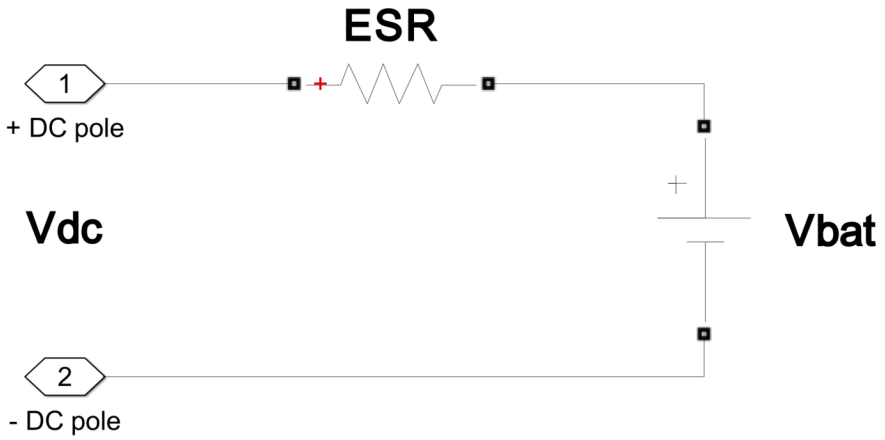

Figure B.3: MMC-BESS: Centralized battery.

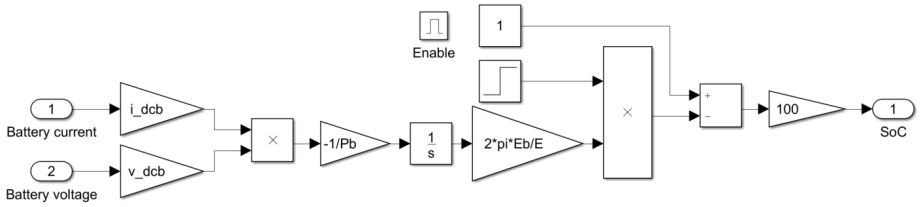

Figure B.4: MMC-BESS: Battery state-of-charge measurement.

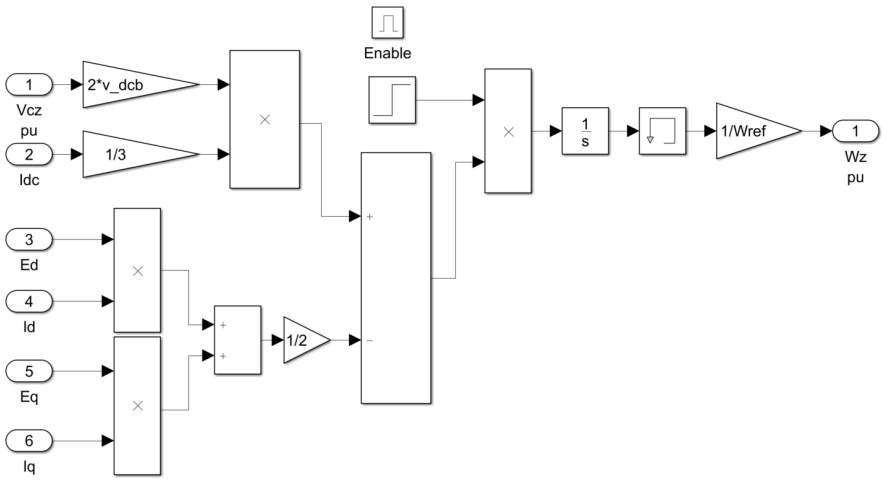

Figure B.5: MMC-BESS: Energy balance.

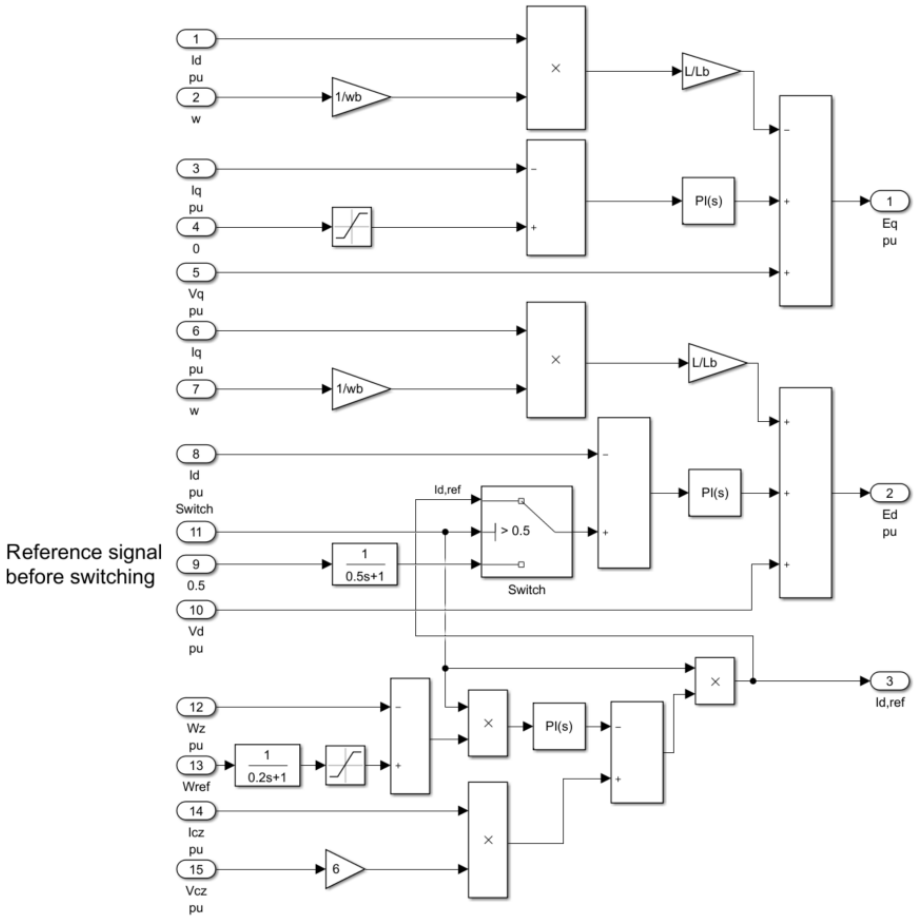

Figure B.6: MMC-BESS: Zero-sequence energy controller and AC current controller.

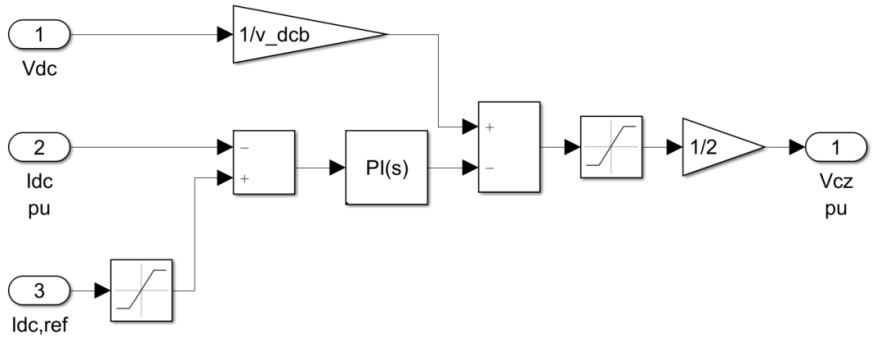

Figure B.7: MMC-BESS: DC current controller.

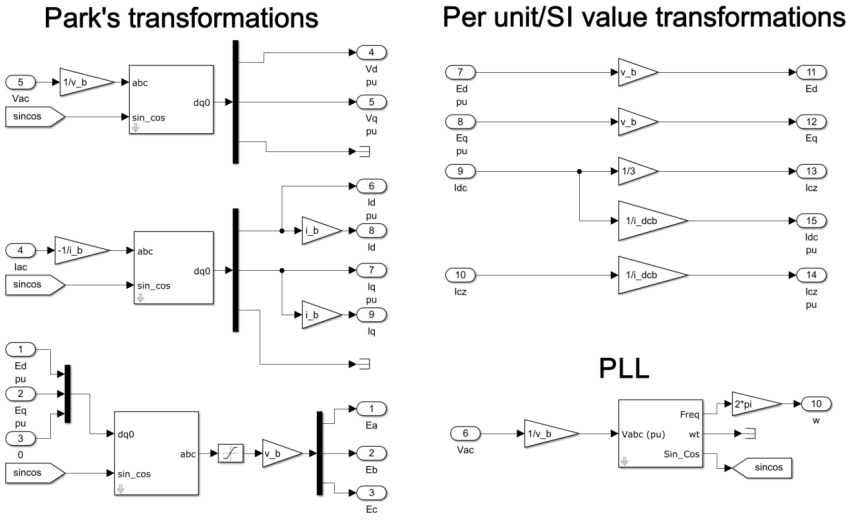

Figure B.8: MMC-BESS: PLL and transformations.

APPENDIX C

MMC-BESS model: Per unit system

The base values of the HVDC transmission system and the MMC-BESS are presented below. In both systems the base voltage and base apparent power are given, whereas the remaining base values can be calculated from the given voltage and power base values. Furthermore, the parameters of both systems are presented in tables.

C.1 HVDC transmission system

The parameter values in Table C.2 are found in CIGRÉ Technical Brochure TB 604 *Guide for the Development of Models for HVDC Converters in a HVDC Grid* [31].

Table C.1: HVDC transmission system base values.

Base	Symbol	Value
Active power	P_b	1000 MW
Power factor	pf	0.95
Apparent power	S_b	1052.6 MW
Line voltage	V_b	400 kV

Table C.2: HVDC transmission system parameters in per unit and SI values.

VSC parameter	Symbol	Per unit value	SI value
Converter resistance	R_{vsc}	0.0047	0.7600 Ohm
Converter inductance	L_{vsc}	0.1469	0.0617 H
Converter capacitance	C_{vsc}	0.6000	$2.9605 \cdot 10^{-4}$ ms
Line parameter	Symbol	Per unit value	SI value
Distance	dist	–	200 km
Line resistance	R_{line}	–	1.900 Ohm
Line inductance	L_{line}	–	0.4224 H
Line capacitance	C_{line}	–	$1.9060 \cdot 10^{-5}$ F
Line conductance	G_{line}	–	$4.8000 \cdot 10^{-6}$ S

C.2 Line-frequency transformer

The transformer is modeled as a simplified three-phase transformer, with an equivalent impedance at its primary side. Hence, the secondary side impedance is zero. The primary side of the transformer is connected to PCC and the secondary side is connected to the AC terminals of the MMC. The excitation branch is neglected by using very high pu values for the core-loss resistance and the magnetizing inductance. The excitation branch is commonly regarded as an open circuit and therefore ignored for power system analysis purposes.

Table C.3: Line-frequency transformer base values.

Transformer parameter	Symbol	Value
Active power	P_b	180 MW
Power factor	pf	0.95
Apparent power	S_b	189.5 MW
Line voltage	V_b	400 kV
Turn-ratio	n	4.54

Table C.4: Line-frequency transformer parameters in per unit and SI values.

Transformer parameter	Symbol	Per unit value	SI value
Primary side resistance	R_{prim}	0.005	380 mOhm
Primary side leakage inductance	L_{prim}	0.15	36.3 mH
Secondary side resistance	R_{sec}	0	0
Secondary side leakage inductance	L_{sec}	0	0
Core-loss resistance	R_c	500	–
Magnetizing inductance	L_m	500	–

C.3 MMC

The MMC parameters are based on [70], where the DC-side equivalent capacitance is calculated based on the number of submodules per converter arm being 200.

Table C.5: MMC base values.

Base	Symbol	Value
Active power	P_b	180 MW
Power factor	pf	0.95
Apparent power	S_b	189.5 MW
AC-side line voltage	V_b	40 kV

Table C.6: MMC parameters in per unit and SI values.

Converter parameter	Symbol	Per unit value	SI value
Filter resistance	R_f	0.0032	0.0655 Ohm
Filter inductance	L_f	0.1229	0.0080 H
Arm resistance	R_a	0.0030	0.0616 Ohm
Arm inductance	L_a	0.0480	0.0031 H
AC-side equivalent resistance	R_{AC}	0.0047	0.0963 Ohm
AC-side equivalent inductance	L_{AC}	0.1469	0.0096 H
DC-side equivalent resistance	R_{DC}	$7.5212 \cdot 10^{-4}$	0.0411 Ohm
DC-side equivalent inductance	L_{DC}	0.0120	0.0021 H
Submodules per arm	N_{valve}	200	200
DC-side equivalent capacitance	C_{eq}	0.0042	0.2050 ms

APPENDIX D

MMC-BESS model: Matlab script

The Matlab script below was made for the Simulink model presented in Chapter 11, cf. Figure 11.18.

D.1 MMC-BESS and HVDC transmission system Matlab script

MasterThesis_MMC_HVDC_script.m

```
%% MMC-BESS and HVDC transmission system
% A Matlab script calculating base values, system parameters and
% controller parameters for both MMC-BESS and HVDC transmission system:

close all
clear all
warning off

%% HVDC transmission system

Pbase = 1000e6; %Base active power
pf = 0.95; %Power factor
Sbase = Pbase/pf; %Base apparent power
Vbase = 400e3/sqrt(3); %Base phase voltage (peak value)
Ibase = 2*Sbase/(3*Vbase); %Base current (peak value)
Vdcbase = 2*Vbase; % DC base phase voltage definition
Idcbase = Sbase/Vdcbase;% Base DC current (or Idcbase = (3/2)*Ibase)
fbase = 50; % Base system frequency
wbase = 2*pi*fbase; % Base rotational frequency
Zbase = Vbase/Ibase; % Base impedance
Zdcbase = Vdcbase/Idcbase; % Base DC impedance
Xlbase = Zbase; % Base reactance
Lbase = Xlbase/wbase; % Base AC inductance
Ldcbase = Zdcbase/wbase; % Base DC inductance
Cdcbase = 1/(Zdcbase*wbase); % Base DC capacitance
```

```
fsw = 2.5e3; % Switching frequency
Ts = 100e-6; % Sampling time

%% Design of the VSC parameters (Rvsc, Lvsc, Cvsc):
% Calling function VSCpu for calculating various parameters of the HVDC
% transmission system:

[Cvsc,Lvsc,Rvsc,kpvsc,kivsc,kpIout,kiIout,wbase,poles,Ta]= VSCpu(Vbase,
    Ibase,fsw);

% Cvsc: DC-link capacitor (VSC)
% Lvsc: Inductor AC (VSC)
% Rvsc: Resistor AC (VSC)
% kpvsc: PI current controller - proportional gain, PI type: Kp+Ki/s
% kivsc: PI current controller - integral gain
% kpIout: PI voltage controller - proportional gain, PI type: Kp+Ki/s
% kiIout: PI voltage controller - integral gain
% wbase: Base rotational speed
% Poles: Provides information about the controllers, as well as the
% current and voltage systems
% Ta: Time constant of the sensor and PWM

%% Frequency domain analysis controllers and RL system
% Nyquist and Bode diagrams of controller and RL system:

figure
nyquist(tf(1,[Lvsc,Rvsc]),poles(1).Gci,poles(1).Gcv)
grid on
legend(['RL ';'Gci';'Gcv'])

figure
bode(tf(1,[Lvsc,Rvsc]),poles(1).Gci,poles(1).Gcv)
grid on
legend(['RL ';'Gci';'Gcv'])

%% Line design
% The HVDC line between the two converter stations in the point-to-point
% HVDC transmisssion system

dist = 200; % in km
Cline_mtdc = dist*(0.1906e-6)/2; % in uF/km
Gline_mtdc = dist*(0.048e-6)/2;  % in uS/km
Lline_mtdc = dist*2.1120e-3; % in mH/km
Rline_mtdc = dist*0.0095;    % in ohm/km

%% Transformer parameters
% Transformer turn ratio is set, which in turn sets the AC-side base
% voltage of the MMC-BESS:

VbaseTF1 = Vbase; % Base phase voltage (peak voltage) on prim. winding
PbaseTF = 180e6; % Base active power
SbaseTF = PbaseTF/pf; % Base apparent power
fTF = 50; % Operating freqency for the transformer (same as system freq.)
n = 4.54; % Turn ratio for MMC-BESS I and III (MMC_BESS_design.m-script)
%n = 3.02; % Turn ratio for MMC-BESS II (MMC_BESS_design.m-script)
VbaseTF2 = VbaseTF1/n; % Base phase voltage (peak voltage) on sec. winding
RTF1 = 0.005; % prim. wind. resistance [pu]
```

```
LTF1 = 0.15; % prim. wind. inductance [pu]
RTF2 = 0; % sec. wind. resistance
LTF2 = 0; % sec. wind. inductance

%% MMC-BESS
% MMC is modeled based on paper "Tuning of Control Loops for Grid-
% Connected Modular Multilevel Converters under a simplified Port
% Representation for Large System Studies" (Sanchez, Bergna, Tedeschi,
% 2017) [1]:

Pb = PbaseTF; % Base active power
Sb = Pb/pf; % Base apparent power (same pf for HVDC transmission system)
t = 0.25; % Discharge time of the battery
v_b = VbaseTF2; % Base phase voltage (peak value)
i_b = 2*Sb/(3*v_b); % Base current (peak value)
v_dcb = 2*v_b; % DC base voltage definition
i_dcb = Sb/v_dcb; %Base DC current (or Idcbase = (3/2)*Ibase)
fb = 50; % Base system frequency
wb = 2*pi*fb; % Base rotational frequency
Eb = Sb/wb; % Energy capacity base
E = Pb*t; % Battery energy capacity
Zb = v_b/i_b; % Base impedance
Zdcb = v_dcb/i_dcb; % Base DC impedance
Lb = Zb/wb; % Base inductance
%Cb = 1/(Zb*wb); % Base capacitance to get Cpu in Farads
Cb = 1/Zb; % Base capacitance to get Cpu in milliseconds
Ldcb = Zdcb/wb; % Base DC-side inductance
Cdcb = 1/(Zdcb*wb); % Base DC-side capacitance
fco = 2e3; % Cut-off requency, defines the bandwith of the controllers
        % fo = 2000 Hz is used in the paper [1]
Tfi = 1/(2*pi*fco); % Filter time constant
ESR = 0.001; % Equivalent internal series resistance of the battery

%% Parameters converted from per unit values to SI values:
% The per unit values from the paper [1] (with base values
% Vb = 400/sqrt(3) kV and Sb = 1200 MVA) are converted to
% per unit values for the master's thesis:

% Per unit values of converter parameters
Ceqpu = 0.0042; % Equivalent DC-side capacitance
Rpu = 0.0047; % AC-side equivalent resistance
Lpu = 0.1469; % AC-side equivalent inductance
Rdcpu = 7.5212e-4; % DC-side equivalent resistance
Ldcpu = 0.0120; % DC-side equivalent inductance

% SI values of the converter parameters
Rdc = Rdcpu*Zdcb; % DC-side equivalent resistance
Ra = (3/2)*Rdc; % Arm resistance
Ldc = Ldcpu*Ldcb; % DC-side equivalent inductance
La = (3/2)*Ldc; % Arm inductance
R = Rpu*Zb; % AC-side equivalent resistance
L = Lpu*Lb; % AC-side equivalent inductance
Rf = R-(Ra/2); % Filter resistance
Lf = L-(La/2); % Filter inductance
Ceq = Ceqpu*Cb; % DC-side equivalent capacitance in seconds

Narms = 2; % Number of converter arms per phase-leg in the MMC
```

```
Wref = 4*Narms*Ceq*(v_b)^2; % Energy reference

%% AC current controller (PI) gains
% Modulus optimum tuning technique:

k = 1/Rpu;
T = Lpu/(wb*Rpu);
Tf = Tfi;
Kpac = T/(2*Tf*k);
Ti = T;
Kiac = Kpac/Ti;

%% DC current controller (PI) gains
% Modulus optimum tuning technique:

k = 1/Rdcpu;
Tdc = Ldcpu/(wb*Rdcpu);
Tf = Tfi;
Kpdc = Tdc/(2*Tf*k);
Ti = Tdc;
Kidc = Kpdc/Ti;

%% Zero-sequence energy controller (PI) gains
% Symmetrical optimum tuning technique:

Ta = Tfi;
Teq = 2*Ta;
b = wb/(8*Ceqpu);
p = 1/Teq;
alpha = 6;
phiw=asin((alpha-1)/(alpha+1));
z = p/alpha;
wm = sqrt(z*p);
kpw = wm/b;
kiw = kpw*z;

%% Real internal AC loop

tau = Lpu/(Rpu*wb);
Hpi = tf(1/Rpu,[tau,1])*tf(1,[Tfi,1]); % System
Hci = tf([Kpac,Kiac],[1,0]); % Controller
Holac = Hpi*Hci; % Open-loop transfer function
Hclac = feedback(Holac,1); % Closed-loop transfer function

%% Real internal DC loop

taudc = Ldcpu/(Rdcpu*wb);
Hpidc = tf(1/Rdcpu,[taudc,1])*tf(1,[Tfi,1]);
Hcidc = tf([Kpdc,Kidc],[1,0]);
Holdc = Hpidc*Hcidc;
Hcldc = feedback(Holdc,1);

%% Transfer functions of the energy balance-part
% Bode diagram of the close-loop transfer functions:

Hin = tf(1,[Teq,1]); % Equivalent inner system
Hout = tf(b,[1,0]); % Energy transfer function
```

```
Hc = tf([kpw,kiw],[1,0]); % Controller transfer function
Hol = Hin*Hout*Hc; % Open-loop transfer function
Hcl = feedback(Hol,1); % Closed-loop transfer function

% Hclac = Gc AC in thesis
% Hcldc = Gc DC in thesis
% Hcl = Gc Wz in thesis

figure
bode(Hclac,Hcldc,Hcl)
grid on
```

D.2 HVDC transmission parameter Matlab function

VSCpu.m

The function **VSCpu** is called inside the Matlab script in Appendix D.1.

```
%% VSC parameter design

function [Cvsc,Lvsc,Rvsc,kpvsc,kivsc,kpIout,kiIout,wbase,poles,Ta,taupu,
    Tivsc]= VSCpu(Vbase,Ibase,fsw)
Vllbase=Vbase*sqrt(3/2); % Line voltage in RMS
Vdcbase=2*Vbase; % DC base voltage
Zbase=Vbase/Ibase; % AC base impedance
Sbase=3*Ibase*Vbase/2; % AC base apparent power
wbase=2*pi*50; % AC base rotational speed
Idcbase=Sbase/Vdcbase; % DC base current
Deltai=0.15*Ibase; % Maximum current ripple

Lbase=Zbase/wbase; % AC base inductor
rpu=0.01; % Filter resistance from Cigre B4 HVDC
R2=rpu*Zbase;  % Resistor in SI
Lpu=0.255; % AC inductor in per unit from Cigre B4 HVDC
L2=Lpu*Lbase; % Inductor in SI
Cbase=1/(Zbase*wbase);  % AC base capacitor

%% DC capacitor design

Zdcbase=Vdcbase/Idcbase; % DC base inductor
Cdcbase=1/(wbase*Zdcbase); % DC base capacitor
a=1;
Cpu=60e-3; % DC capacitor in per unit from Cigre B4 HVDC (based on ms)
C2=Cpu/Zdcbase; % DC capacitor in SI
Cpudc=Cpu;  % DC capacitor in per unit

%% AC current controller design
% Inner loop controller, modulus optimum:

taupu=Lpu/rpu; % Tau without wbase
Ta=1.5/(fsw);  % PWM and analog sensor approximation
kpvsc=(1/2)*(taupu*rpu/(wbase*Ta)); % Proportional gain
Tivsc=taupu/wbase; % Integrator time
kivsc=kpvsc/Tivsc; % Integral gain

%% Closed-loop inner system

```

```
wo=1/(sqrt(2)*Ta); % Control frequency
ro=Ta*wo; % Optimal approximation = 0.707

%% DC voltage controller design
% Outer loop controller, symmetrical optimum:

Teq=2*Ta; % Equivalent time constant, inner loop
p=1/Teq; % Pole of the inner loop
alpha=6; % Gain to obtain the z < p
phi=asin((alpha-1)/(alpha+1)); % Phase margin defined by alpha
z=p/alpha; % Zero for the controller design
wcut=sqrt(z*p); % Frequency for max. peak phase margin
Kvv=(Cpudc/wbase)*wcut;
kpIout=Kvv; % Proportional gain
kiIout=Kvv*z; % Integral gain

%% Parameters to be returned
Lvsc=L2; Rvsc=R2; Cvsc=C2;

% Controllers analysis (inner and outer loop controllers)
% Poles analysis:

kk=wbase/Lpu;
kc=wbase/Cpudc;

poles(1).RL=-Rvsc/Lvsc;
poles(1).I=roots([1,kk*kpvsc,kk*kivsc]);
poles(1).V=roots([1,kc*kpIout,kc*kiIout]);
wo2=sqrt(kc*kiIout);
wo=sqrt(kk*kivsc);
poles(1).w=[wo,wo2];
poles(1).RLtf=tf(1,[Lvsc,Rvsc]);
poles(1).Gci=tf([kk*kpvsc,kk*kivsc],[1,kk*kpvsc,kk*kivsc]);
poles(1).Gcv=tf([kc*kpIout,kc*kiIout],[1,kc*kpIout,kc*kiIout]);

return
```